Smouldering and self-sustaining reactions in solids: an experimental approach

Rory M. Hadden

A thesis submitted for the degree of Doctor of Philosophy
The University of Edinburgh
2011

Abstract

Smouldering combustion governs the burning of many materials in the built and natural environments. Smouldering is flameless, heterogeneous combustion which occurs when oxygen reacts with the surface of a solid fuel. Understanding the conditions which will result in the ignition and smouldering of a porous fuel is important and the phenomena involved are complex and coupled, involving heat and mass transfer, and chemical kinetics. This thesis reports experimental studies of the ignition, spread, suppression and emissions from reactions in porous media. Similar experimental techniques are shown in this thesis to be applicable when studying a wide range of solids which undergo self-sustaining reactions.

This thesis is presented in a manuscript style. Each chapter takes the form of an independent paper which has been prepared for journal publication and as such, each chapter can stand on its own as a piece of research. A final chapter summarizes the findings and conclusions and suggests further areas of research.

Chapter 1 presents a study of self-sustaining decomposition of ammonium nitrate containing inorganic fertilizer. This is of importance to the shipping industry which transports these materials in large quantities. Upon exposure to a heat source, ammonium nitrate may undergo exothermic decomposition which can propagate through the material, posing safety and economic threats. This reaction does not involve oxygen-based chemistry, but has many similarities to the propagation of a smoulder front in a porous material. Small-scale experiments to investigate the self-sustaining decomposition (SSD) behaviour of NPK (nitrogen, potassium, phosphorous) 16.16.16 fertilizer were undertaken. Experiments showed that this material will undergo self-sustaining decomposition and are used to formulate a reaction framework. Findings were applied to the events that occurred aboard the *Ostedijk* in 2007.

Chapter 2 is a study of smoulder in polyurethane foam to study the relationship between sample size, critical heat flux and spread rate. Smouldering fires are the leading cause of residential fire deaths in developed countries and polyurethane foam is ubiquitous in the modern world. The critical heat flux for ignition was found to decrease with increasing sample size and the spread rate was found to be a function of the sample size, smoulder propagation depth and the applied heat flux. This is the first time that results on the effect of sample size on smouldering have been reported in the literature and these can be used to aid the extrapolation of small-scale flammability testing results to large scale scenarios.

Chapter 3 presents an experimental investigation into the ignition of porous fuels by hot particles. This is related to the problem of spotting ember ignition in wildland fires which is a major, but poorly understood, spread mechanism. The process of spotting occurs in wildland fires when fire-lofted embers or hot particles land downwind, leading to ignition of new, discrete fires. The work studies the ignition of a fuel as a function of ember size and temperature. Metal particles are used as a proxy for burning embers and powdered cellulose to represent the forest fuel. Relationships between the size and temperature of the particle required for flaming and smouldering ignitions are found. These results are used to assess the ability of hot-spot ignition theory to determine the particle size–temperature relationship required for ignition of a cellulose fuel bed.

Chapter 4 is an investigation into the suppression of smouldering coal. Subsurface coal fires are a significant global problem with fires in China alone estimated to consume up to 200 million tons of coal per year. As global demand for coal increases, accidental fires are a waste of a useful energy resource as well as a source of pollution and greenhouse gases. The results are the first attempt reported in the literature to study the suppression of these fires under controlled laboratory conditions. The ignition, spread and suppression of subsurface coal fires were studied using small-scale laboratory experiments. Time to ignition was seen to depend on particle size with small and large particles resulting in long times to ignition, while medium sized particles resulted in the shortest time to ignition. The maximum temperature, spread rate and mass lost were found to be independent of particle size above a critical particle size. The effectiveness

of three systems for delivery of a suppression agent were assessed – direct injection, shower and spray. The effect of particle size on the water required for extinguishing using a spray was found to be weak.

Chapter 5 presents an experimental investigation of the smouldering behaviour of peat. This is of particular interest in understanding the impact of smouldering fires on the earth system. The longer burn durations and different combustion dynamics of smouldering compared to flaming means that they have been shown to consume large amounts of biomass in, and contribute significantly to the emissions from, natural fires occurring in peatlands. The dynamics of smouldering peat in shallow, strong fronts was studied in the Fire Propagation Apparatus and a smoulder reaction framework with two burning regimes is presented. The first regime is peat smouldering and was found to be controlled by the applied heat flux and the second regime corresponded to char smouldering and was more sensitive to the flow of oxidizer.

Chapter 6 complements Chapter 5 with an analysis of the CO and CO_2 emissions for smouldering and flaming peat. This data can be used with large-scale measurement techniques to improve emission estimates. The emissions are found to be dependent of the burning regime and the type of combustion with flaming resulting in higher fluxes of CO_2 and lower fluxes of CO compared to peat smouldering. Char smouldering resulted in the highest yields of CO and CO_2. The large majority of emissions (85% of CO_2 and 97% of CO) are released during the smoulder phase of the reaction. This highlights the differences in the chemical processes occurring under these two modes of combustion.

Chapter 7 summarizes the research undertaken in this thesis and presents possible further work.

Contents

List of Figures

List of Tables

Declaration

This thesis and the work described within has been conducted solely by Rory Hadden under the supervision of Dr Guillermo Rein and Prof. José L. Torero. Where others have contributed or other sources are quoted, references are given in full.

Rory Hadden

2011

Acknowledgements

First of all, thanks must go to my supervisor Dr Guillermo Rein without whom, had it not been for a chance email, I might never have been introduced to this fascinating field. Your optimism, encouragement, support and belief has got me here.

Thanks also to Prof. José Torero, a constant, seemingly inexhaustible source of knowledge on fire. Thanks also for investing so much in fostering a feeling of community in the group – this has been a great place to spend the last three years.

This research was funded by the Engineering and Physical Sciences Research Council. Additional funding was provided by International Fire Investigators and Consultants Ltd, so my thanks to the staff there, especially Dr Jim Lygate who has allowed me to experience life in the real world of fire investigation during my PhD, usually by asking the unanswerable. I have enjoyed every one of the challenges you have thrown at me.

A special thanks to all my colleagues at the Fire Lab for making the last three and a bit years so much fun, whether at home or abroad. A special mention to my lab forefathers: Thomas, Pedro, Paolo, Hubert and Ricky. Without your patience I would have been lost at sea, you taught me how to burn things well. To Master Wolfram, I know I have lots to learn but you are an excellent teacher. Nico has been a constant source of knowledge, particularly on crème brûlée. Jimbo, your trips to Edinburgh always provided a welcome distraction. Freddy, thanks for sharing the FPA with me. Thanks to Claire for showing me a new way to think about science. I should specially like to thank Angus, Joanne, Kate and Sue for always being around for a cup of tea, lunch or a cocktail.

The award of a J. M. Lessells Travel Scholarship from the Royal Society of Edinburgh allowed me to spend time at the University of California, Berkeley for four months

in 2009. I had a great time working in the lab with Prof. Carlos Fernandez-Pello (my academic grandfather). Thanks to Dave and Erin Rich (and Fred and Amelia) for welcoming me so warmly in to their home – it wouldn't have been the same without you. Thanks also to the best lab mates on the other side of the pond: Chris, Sonia, Sarah, Colin, Andres and MaryAnne.

My time in Edinburgh has been so much fun thanks to friends and family. Thanks to the Lee House crowd and the members of Edinburgh University Wind Band for making Wednesday (and so many other) nights so much fun. Thanks Catriona, Charlie, Laura, Lawrence, Liz and Lucy for continuing the Wednesday night tradition. Thanks to Ben (Roger knows why) for being such an excellent friend.

Thanks to Daniel for forging a path for me to follow and showing me all that was possible. Mum and Dad, thanks for being there and showing so much support. I am so lucky.

To all of you, thanks!

Preface

This thesis is presented in a manuscript format. Each chapter is written in the style of a research paper which has been prepared for journal publication. Using a musical analogy, this work differs from a traditional thesis as a series of études differs from a symphony.

The material is presented in the following order:

- Chapter 1 is an investigation into the decomposition behaviour of ammonium nitrate containing fertilizers. The findings of small-scale experiments are applied to the events that occurred aboard the cargo ship *Ostedijk* in 2007. The chapter is based on:

  R. M. Hadden and G. Rein. Small-scale experiments of self-sustaining decomposition of NPK fertilizer and application to events aboard the Ostedijk in 2007, *Journal of Hazardous Materials*, **186**, 731–737, 2011.

- Chapter 2 is an investigation into the effect of sample size on smouldering combustion of polyurethane foam. This is based on the following paper which has been accepted for publication:

  R. M. Hadden, A. Alkatib, G. Rein and J. L. Torero. Radiant ignition of polyurethane foam: the effect of sample size, *Fire Technology*, 2011.

- Chapter 3 is a manuscript on the ignition of combustible fuel beds by hot embers. This work was undertaken at the University of California, Berkeley under the supervision of Prof. Carlos Fernandez-Pello and is based on:

  R. M. Hadden, S. Scott, C. Lautenberger and A. C. Fernandez-Pello. Ignition of combustible fuel beds by hot particles: an experimental and theoretical study, *Fire Technology*, **47**, 341-355, 2011.

- Chapter 4 is an experimental study of the suppression of subsurface coal fires using small scale experiments and is based on:
  R. M. Hadden and G. Rein. Burning and suppression of smouldering coal fires, in Coal and Peat Fires: A Global Perspective, Volume 1, Chapter 18, Editors G. B. Stracher, E. V. Sokol, and A. Prakash, Elsevier, 2010.

- Chapter 5 is an experimental study of the dynamics of smouldering peat using small-scale experiments. This is intended for the fire engineering and wild fire communities as it provides a fundamental investigation of the controlling mechanisms of smouldering combustion. It will be submitted for publication in an appropriate journal.

- Chapter 6 is a study of the emissions from smouldering and flaming peat fires. This is of interest in the fields of climate modelling and geoscience and will be submitted for publication in an appropriate journal.

Selected publications

As a result of this work, other papers have been published as follows:

- C. M. Belcher, J. Yearsley, **R. M. Hadden**, J. McElwain and G. Rein. Baseline intrinsic flammability of Earth's ecosystems estimated from paleoatmospheric oxygen over the past 350 million years. *Proceedings of the National Academy of Sciences*, **107**, 22448-22453, 2010.

- **R. M. Hadden**, S. Scott, A. Yun, C. Lautenberger, and A. C. Fernadez-Pello. Ignition of cellulose fuel beds by hot metal particles. International Congress on Combustion and Fire Dynamics, Santander, October 2010.

- **R. M. Hadden**, G. Rein. Ignition, suppression and CO/CO_2 emissions of subsurface coal fires at laboratory scale. Second International Conference on Coal Fire Research, Berlin, May 2010.

- **R. M. Hadden**, A. Alkatib, G. Rein and J. L Torero. Radiant ignition of smouldering combustion in polyurethane foam: the effect of sample size. Proceedings of the 6th International Seminar on Fire and Explosion Hazards, Leeds, April 2010.

- **R. M. Hadden**, G. Rein. Ignition and suppression of smouldering coal fires in small-scale experiments. Fall meeting of the Western States Section of The Combustion Institute, Irvine, October 2009.

- **R. M. Hadden**, G. Rein. Small scale extinguishing experiments of coal subsurface fires. 6th Mediterranean Combustion Symposium, Ajaccio, June 2009.

- **R. M. Hadden**, F. X. Jervis and G. Rein. Investigation of the fertilizer fire aboard the *Ostedijk*. International Association of Fire Safety Science 9, Karlsruhe, September 2008, doi:10.3801/IAFSS.FSS.9-1091.

1

Small-scale experiments of self-sustaining decomposition of NPK fertilizer and application to the events aboard the *Ostedijk* in 2007

Summary

Small-scale experiments to investigate the self-sustaining decomposition (SSD) behaviour of NPK 16.16.16 fertilizer have been undertaken. These experiments show that this material will undergo self-sustaining decomposition and are used to give insight into the behaviour of the reaction. A three-step decomposition process is observed leading to a self-sustained reaction reaching temperatures of 200–350°C. The measured heat of reaction is 0.73–1.8 $MJ \cdot kg^{-1}$. Measurements are applied to the events that occurred aboard the ship *Ostedijk* in 2007 in which a SSD reaction occurred. The mass loss rate from the cargo was calculated to range from approximately 0.5 $kg \cdot s^{-1}$ on the first day to 12 $kg \cdot s^{-1}$ on the last day. From this measurement, the maximum fire size was estimated to be in the range 5.8–29 MW.

1.1 Introduction

Self-sustaining decomposition (SSD) is the phenomenon in which a locally initiated decomposition reaction spreads through the mass of a material. This phenomenon has been reported to occur in inorganic fertilizers and other materials with a high ammonium nitrate fraction. Other materials, such as peroxides, are also known to undergo exothermic decomposition [1].

Self-sustaining decomposition incidents can be initiated by self-heating or external heat sources. Self-heating is the phenomenon in which the temperature in a body of material rises due to heat being generated by some process taking place within the material. If this heat cannot be lost to the surroundings at a rate greater than that at which it is generated, then a thermal runaway may occur [2]. Self-heating of fertilizers is promoted when large quantities of material remain undisturbed for a long time e.g. in bulk storage or transportation, or if there is contamination with organic material with which ammonium nitrate will start to react directly at around 100°C [3]. Local external heat sources (e.g. hot work, hot surfaces and embers) can also initiate a SSD [4].

Large SSD events are rare with one occurring worldwide on average every three years [4]. The consequences can be severe with direct casualties, formation of toxic plumes and explosions [4, 5]. Incidents involving SSD of fertilizers include warehouses in Cartagena, Spain in 2002, on the Humber coast in north-east England in 1993 and in Nantes, France in 1987 [5, 6]. These incidents were initiated by relatively small heat sources (e.g. electric lamps or faults in electric equipment) but resulted in the formation of large, toxic plumes. Kiiski [4] gives a review of eleven SSD incidents dating back to 1962 and Marlair et al. [5] summarize seven incidents dating back to 1972.

1.2 The *Ostedijk* and the incident timeline

In February 2007, 6012 tonnes of NPK (nitrogen, phosphorous and potassium) fertilizer cargo aboard the *Ostedijk* underwent a self-sustaining decomposition which lasted for seven days destroying part of the cargo and compromising the ship. The incident took place off the north-west coast of Spain while the vessel was en route from Porsgrunn,

Norway to Valencia, Spain. A detailed timeline of events is available in [7]. The decomposition occurred in Cargo Hold Two which contained 2,627 tonnes of fertilizer.

The incident was closely followed by the Spanish media (see [7] for full details), which provided good photographic evidence of the evolution of the plume size. The plume was seen to grow from about 0.5 m diameter to greater than 50 m over five days. Although the composition of the plume is unknown, it is likely that it contained nitrogen, nitrous oxides, water vapour, and ammonium and chlorine compounds, which are products typical of NPK fertilizer decomposition [6, 8]. Thermal imaging deployed by emergency personnel measured surface temperatures of the cargo to be in excess of 175°C [7]. Heat losses from the surface mean that the inside of the cargo must have been at temperatures significantly higher than this.

Initial firefighting aboard the *Ostedijk* utilized an auxiliary ship to cool the outside of the hold with water jets. This started on the fourth day but proved ineffective in controlling the fire. On the fifth day, specialist salvors boarded the vessel and used localized application of water to cool the interior of the cargo. The plume prior to the commencement of extinguishing can be seen in Fig. 1.1. On the seventh day, the fire was declared extinguished and the vessel was allowed to reach port at Bilbao. The cargo after suppression can be seen in Fig. 1.2, which suggests that approximately two thirds of cargo in Hold Two was affected [9].

The International Maritime Organisation described the event as a fire which "broke out ... evidently due to cargo decomposition" [10]. Meanwhile, the official standing of the Spanish authorities was that the incident was a self-sustaining fermentation reaction, which presumably refers to the phenomenon of self-sustaining decomposition [7]. This hypothesis is confirmed by analysis of the photographic evidence, reports from maritime agencies and results from small-scale laboratory experiments reported in this paper.

1.3 The cargo on board the *Ostedijk*

The cargo was inorganic, mineral fertilizer NPK 15.15.15 manufactured in Norway [8]. The naming convention of fertilizers means that this material contains the equivalent

Figure 1.1. The *Ostedijk* on 21st February (the 5th day) after the hold was opened and before specialized firefighting activities had commenced. Derived from photograph courtesy of Agencia EFE [11].

of 15% nitrogen (as ammonium and nitrate salts), 15% phosphorous pentoxide (as phosphates) and 15% potassium oxide (as potassium chloride and potassium oxide) on a mass basis. The remaining portion of the fertilizer consists of micronutrients (magnesium, sulphur, calcium, etc) and anticaking agents. The material is of a granular nature with a bulk density in the range 900–1200 $\mathrm{kg \cdot m^{-3}}$ and particle diameter in the range 2–4 mm.

Ammonium nitrate is commonly found in fertilizers because it incorporates nitrogen in the forms readily taken up by crops (i.e. ammonium and nitrate ions). However, ammonium nitrate is capable of undergoing exothermic decomposition reactions upon exposure to a heat source [3]. Exothermic decomposition of pure ammonium nitrate begins around 200–230°C [12] and it has been suggested that it follows the general reaction described in Eq. 1.1. A further exothermic decomposition reaction which takes place at temperatures above 230°C is presented in Eq. 1.2 [12].

$$\mathrm{NH_4NO_3} \rightarrow \mathrm{N_2O} + 2\mathrm{H_2O} \quad \Delta\mathrm{H} = -37\ \mathrm{kJ \cdot mol^{-1}} \tag{1.1}$$

$$4\mathrm{NH_4NO_3} \rightarrow 3\mathrm{N_2} + 2\mathrm{NO_2} + 8\mathrm{H_2O} \quad \Delta\mathrm{H} = -102\ \mathrm{kJ \cdot mol^{-1}} \tag{1.2}$$

1.3.1 Assessing the hazard of SSD

Ammonium nitrate containing fertilizers are classified according to their propensity to undergo self-sustaining decomposition [13]. This is determined by the Trough Test as set out in the UN Recommendations on the Transport of Dangerous Goods [14]. In

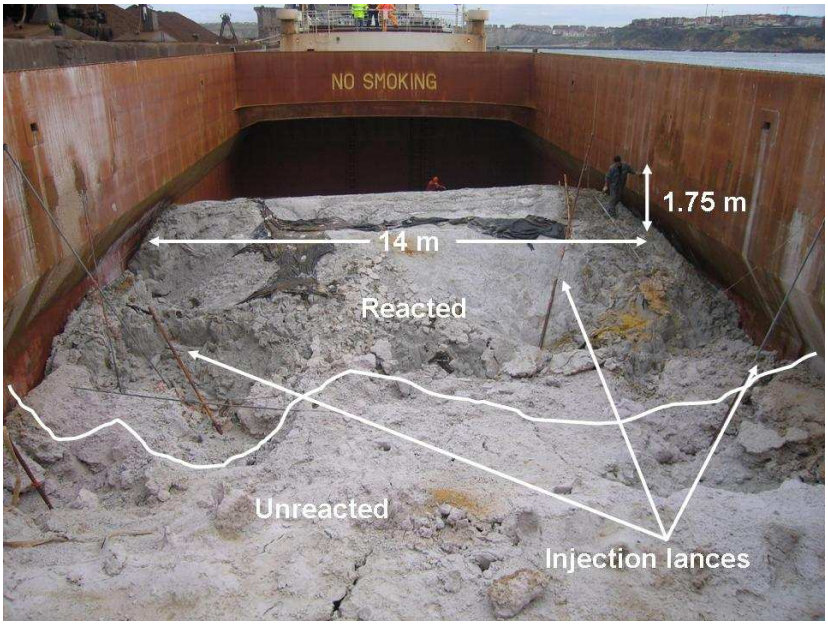

Figure 1.2. Photograph of inside the cargo hold prior to unloading. The demarcation between reacted and unreacted regions as well as the water lances used for firefighting can be seen. Picture courtesy of Ministerio de Fomento, Spain.

this test, a mesh trough of dimensions $150 \times 150 \times 500$ mm^3 is filled with the fertilizer to be tested and heated at one end. The heating is either by a 250 W electric heater or gas burners capable of heating a 1–3 mm thick steel plate to between 400 and 600°C. Heat is applied until decomposition is established and propagation of the front over 30–50 mm is observed (in some cases it may be necessary to continue heating for over two hours). The position of the decomposition front 20 min after heating has been stopped is noted. The position of the front can be determined either by thermocouple readings or differences in colour.

The classifications state that if propagation of the decomposition continues throughout the substance after heating has been stopped, the fertilizer is considered capable of self-sustaining decomposition, and that if propagation does not continue throughout the substance, the fertilizer is considered to be free of the hazard of self-sustaining decomposition. The NPK 15.15.15 aboard the *Ostedijk* was deemed to be free from the hazard of SSD.

Though not the objective of this paper, it is important to highlight some of the limitations of the test. The limitation of the trough test is that it is conducted on the centimetre scale whereas in reality, SSD accidents occur on the metre scale. This

change in scale means that it is not possible to apply the Trough Test results to real-scale applications. Additionally, the ignition protocol in the test is poorly defined and the test only gives a 'yes/no' response to the occurrence of SSD under specific circumstances. This means that the test does not quantify the ability of a material to undergo SSD. Here we use the small scale propagation experiments to investigate the mechanisms of the reactions which are assumed not to be influenced by the sample size.

1.3.2 Decomposition mechanisms of ammonium nitrate-based fertilizers

The decomposition chemistry of ammonium nitrate containing fertilizers differs from that of pure ammonium nitrate (Eqs 1.1 and 1.2), due to the presence of other compounds (especially chlorides) in the aggregate which act to alter the reaction pathway and thermal properties of the material. Public literature relating to these reactions is scarce and few details are published, however reaction mechanisms are presented by Kiiski [4] along with the following observations:

1. NH_4^+ and NO_3^- ions and a catalyst (commonly Cl^-) must be present within a small volume
2. A solid matrix must be present or formed during decomposition such that heat can be trapped and transferred to the reaction zone
3. Sufficient heat must be liberated to overcome heat losses and allow the reaction to propagate

Non-catalysed decomposition

The global non-catalysed reaction mechanism is a chain reaction which goes to completion and proceeds only if there is sufficient heat to maintain the decomposition [12]. The initial step involves the melting and dissociation of ammonium nitrate (NH_4NO_3) to form ammonia and nitric acid (NH_3 and HNO_3) which further decompose to N_2, N_2O, NO_x and NO_xCl [12].

Catalysed decomposition

SSD of fertilizers is generally by the chloride catalysed mechanism. In this case, the decomposition is mainly that of nitric acid (HNO_3) which is formed during the endothermic dissociation of ammonium nitrate NH_4NO_3 [4]. The reaction is initiated by the formation of nitric and hydrochloric acids which undergo a chain reaction with chloride ions acting as a catalyst producing N_2, N_2O, NO_2 and H_2O. The temperature must be in excess of 300°C to allow completion [4].

These mechanisms are complex, result in the formation of many intermediate products and are too complicated for simple analysis. In this work, a simplified framework based on laboratory observations will be proposed for use in post-event analysis (see Section 1.5).

1.4 Laboratory experiments

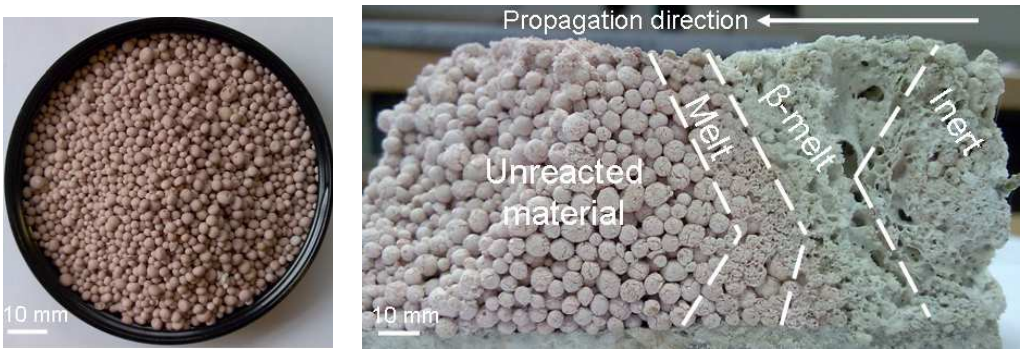

(a) (b)

Figure 1.3. (a) Unreacted fertilizer granules and (b) cross section showing partially reacted sample with 4 phases visible (see section 1.4.1)

Small-scale experiments were carried out to investigate the decomposition behaviour of NPK fertilizer and develop a reaction framework. Experiments were carried out using NPK 16.16.16, a blend which is deemed to be similar in nature (i.e. thermal properties and composition) to that aboard the *Ostedijk* (density in the range 1000–1100 $kg \cdot m^{-3}$ and particle size 2–4 mm). This was due to NPK 15.15.15 being available only in industrial quantities not suitable for laboratory experiments in the UK. Since this paper aims to give an outline of the decomposition framework and not a detailed kinetic study, these materials are sufficiently close in properties and composition to

draw useful conclusions [15, 16]. Three experimental methods were used: bench-scale experiments where the sample is heated with an electrical coil [17], thermogravimetric analysis [18] and experiments in the Fire Propagation Apparatus (FPA) [19]. The experimental findings are applied to the case of the *Ostedijk* in Section 1.5. Figure 1.3a shows the granular nature of the unreacted material.

1.4.1 Propagation experiments

Experiments were performed in a configuration similar to the Trough Test using a box constructed from insulation board. The box had dimensions of $100 \times 100 \times 50$ mm^3 and was covered with aluminium foil. Thermocouples were placed on the igniter and in two rows in the sample at distances of 30 and 60 mm from the igniter to monitor ignition and propagation. Coiled Nichrome wire was used as the heat source for ignition. 150 W of power was applied during the whole experiment. This set-up was used to provide an insight into the ignition of SSD and the conditions necessary for propagation of the decomposition front. Figure 1.3b shows the decomposition occurring in three steps. The unreacted material melts, undergoes reaction to form an intermediate product (β-melt), before undergoing further reaction to form an inert product.

Figure 1.4 shows the temperature evolution of the three thermocouple locations. Below 200°C, melting occurs and there is little offgassing. The exothermic reaction steps occur between approximately 200 and 350°C with initial offgassing of an orange hue which turns white as the reaction progresses. The upper temperature limit observed in Fig. 1.4 is affected by heat transfer from the igniter, which increases the local temperature above that of the reaction.

The reacted samples showed significant mass loss in the reaction zone. There is also a colour gradient from the pink granules of the virgin material, a pink molten phase with some particle agglomeration and a gray phase (β-melt) which is characterized by pores 2–6 mm in diameter. The final, inert phase has an off-white appearance and a density of around 340 kg·m^{-3}. This phase forms a matrix in which small pores approximately 1–3 mm in diameter and larger pores up to several cm in diameter (see Fig. 1.3b).

Mass loss of 49% is measured when reaction spreads throughout the reaction zone.

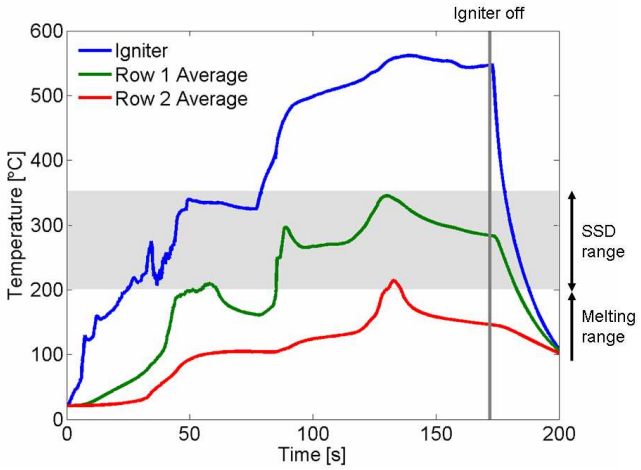

Figure 1.4. Temperature traces for the propagation experiments. The igniter is turned on at t = 0 and is switched off at after 172 s leading to rapid cooling. The temperatures are averages of 2 thermocouples in each row; row 1 is located 50 mm and row 2 90 mm from the igniter at a depth of 25 mm.

The spread rate (calculated using the time when the temperature at a thermocouple exceeds 200°C) was found to be of the order of 10 mm·min^{-1}. This may be a function of the sample size, however further investigation is beyond the scope of this paper.

The propagation experiments do not allow all the details of the decomposition to be observed. In order to gain a better understanding of the reaction paths and exothermicity, further experiments on SSD reactivity were carried out.

1.4.2 Thermogravimetric analysis (TGA)

Thermogravimetric tests [18] allow measurement of the mass loss of a sample as a function of the sample temperature. The resulting mass loss curve allows the reactions occurring during the decomposition of the material to be characterized.

Figure 1.5 shows the relationship between mass and temperature for 10 mg samples of fertilizer, subject to different heating rates and atmospheres. Heating rates of 10°C·min^{-1} and 20°C·min^{-1} were used in an air atmosphere and 10°C·min^{-1} was used in a nitrogen atmosphere up to 500°C. In each case, the following trend is seen: up to 200°C there is very little mass loss. During this time, the sample is melting, which is an endothermic process. Between 220 and 260°C there is a strong reaction resulting in 42–48% mass loss, which is followed by a period of slow mass loss up to 500°C. The total mass loss is approximately 45–52%. There is good agreement between the

temperatures at which the mass loss occurs in these experiments and the reaction temperatures observed in the propagation experiments (Section 1.4.1). There is also good agreement in the mass losses with a value of approximately 50% in both sets of experiments.

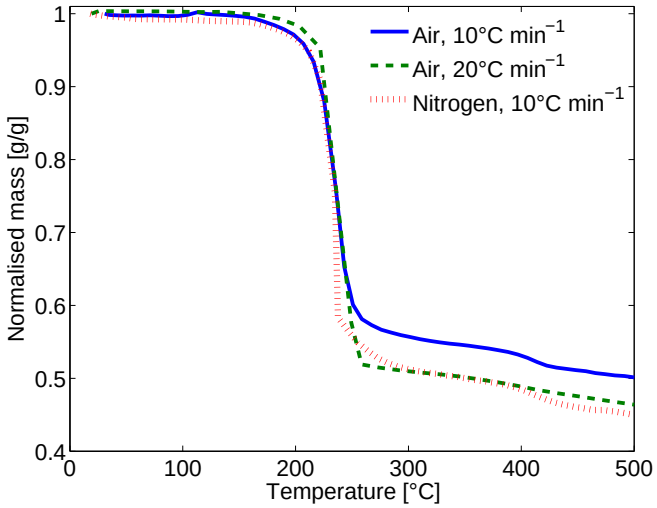

Figure 1.5. Mass versus temperature at heating rates of 10 and 20°C·min^{-1} in air and 10°C·min^{-1} in nitrogen for the TGA experiments. Mass loss is not affected by heating rate or environment, with the majority occurring at 220–260°C in agreement with Fig. 1.4.

Figure 1.6 shows the result of differential thermal analysis (DTA) of the samples. The temperature difference between the sample and an inert reference in the TGA apparatus is measured to give a representation of the heat release of any reactions occurring. Positive temperature differences are a result of exothermic reactions with net heat release, while negative temperature differences arise due to endothermic reactions.

The peak in heat release coincides with the peak in mass loss at temperatures between 220 and 260°C. As the difference is positive, the reaction is exothermic. The difference before and after the peak can be attributed to endothermic reactions such as melting and drying of the fertilizer or further degradation of the product species. The similarity of the curves for air and nitrogen experiments in Figs 1.5 and 1.6 under the air and inert environments means that the reaction does not consume oxygen. Small differences in mass loss and heat release can be attributed to experimental uncertainties, such as sample preparation and variations in heating rate. Units in Fig. 1.6 are in μV, representing the temperature difference between the sample and an inert reference

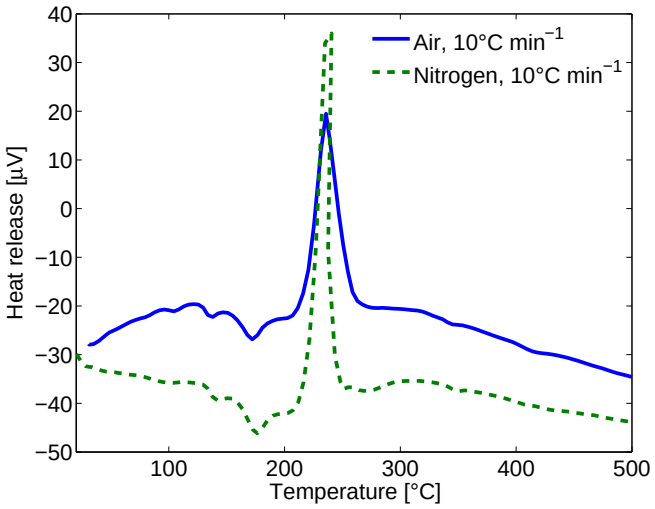

Figure 1.6. DTA measurements for fertilizer in air and nitrogen environments. Maxima represent exothermic reactions and minima endothermic reactions. Note the large exothermic reaction at 220–260°C which is in agreement with temperatures observed in Fig. 1.4. The results can not be interpreted quantitatively due to differences in apparatus and sample preparation, and only provide qualitative estimation of the reactions occurring.

material and therefore the heat release.

1.4.3 Reactivity experiments

The Fire Propagation Apparatus (FPA) [20] was used to investigate the decomposition behaviour and determine the mass loss, gas emissions and heat released rate (HRR) during the SSD process. The FPA is a calorimeter which allows the heat released when a material decomposes to be measured. The decomposition is initiated by a uniform radiative heat flux on the surface of a sample. Product gas composition, flow and temperature can then be measured in the exhaust duct. In this work, the heat release of the fertilizer is measured using the temperature and flow rate of gas in the exhaust duct.

Samples of 130 g of fertilizer were placed in a sample holder of diameter 100 mm, forming a layer 25 mm deep. The samples were exposed to an external radiant heat flux of 20 kW·m^{-2} for various lengths of time. All samples underwent decomposition and, for exposure times greater than 750 s, reached self-sustaining decomposition as seen in Fig. 1.7. If the exposure time was shorter than this then the mass loss was observed to increase with increasing exposure time up to mass loss of around 15%. After this time,

significantly higher mass losses of up to 53% are observed with a lower dependence on exposure time.

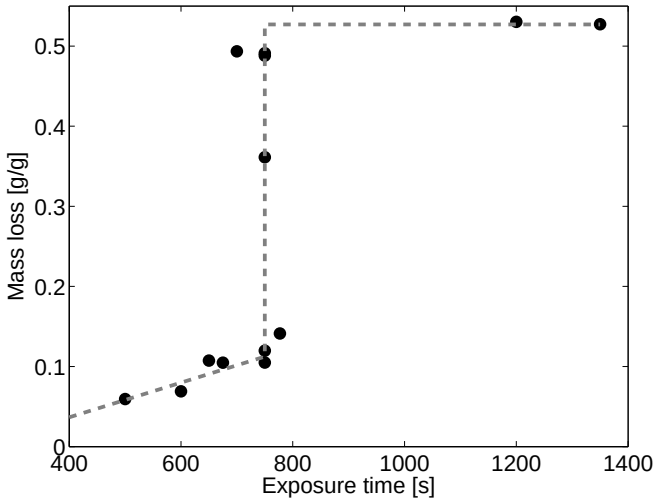

Figure 1.7. Mass loss of samples as a function of the exposure time to the ignition source. The sharp transition at 750 s indicates the onset of SSD.

Figure 1.8a shows the mass loss as a function of time for three samples exposed to the heat flux for 650 s, 750 s and until the reaction is completed after approximately 1250 s. The non-self-sustaining reaction for heat flux exposure of 650 s can be seen as well as the self-sustaining behaviour for exposure times greater than 750 s. The small mass loss early in the experiment is due to the reaction in a thin layer of material on the surface of the sample. For samples where the exposure time was less than 750 s, the mass loss rate is observed to rapidly decrease to zero after the external heat flux is switched off.

Three distinct regimes of mass loss are apparent in Fig. 1.8b which shows six repeats of the same experiment (i.e. incident heat flux of 20 $kW \cdot m^{-2}$ for 750 s): 1) low mass loss rate during the heating phase (0–300 s); 2) moderate mass loss rate (300–700 s); and 3) high mass loss rate (700–1500 s). The reactive fraction of the sample was completely consumed after approximately 1500 s. The mass loss rates in the second and third regime are 0.035–0.045 and 0.06–0.11 $g \cdot s^{-1}$ respectively. Only the third regime is self-sustaining and truly represents the SSD phenomenon. The data after the heat flux is switched off shows more variability suggesting that this stage is more sensitive to small uncontrolled external factors.

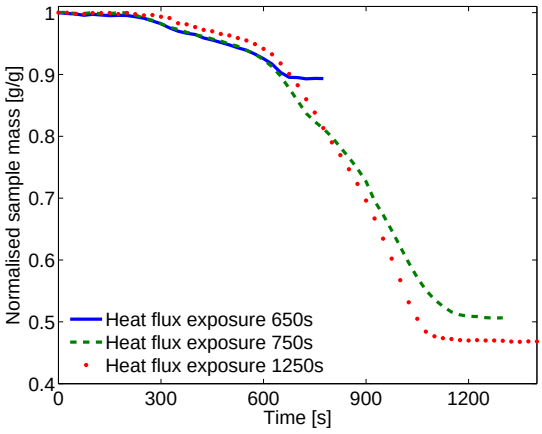

(a)

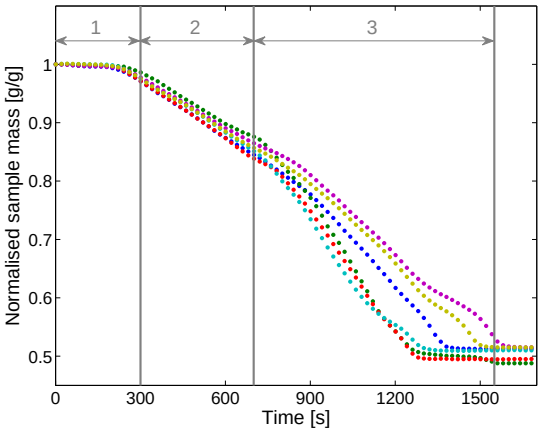

(b)

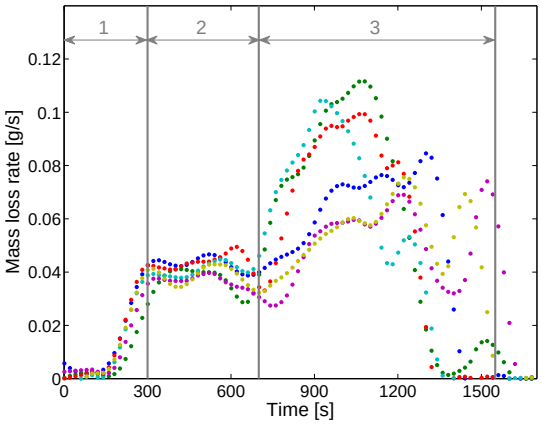

(c)

Figure 1.8. (a) Normalized mass loss for tests with heat flux exposure of 650 s, 750 s and full exposure until reaction completion, 1250 s. The increased mass loss rate and final mass loss for the 1250 s exposure are due to the additional heat insult received by the sample. (b) Normalized mass loss regimes observed in six repeat experiments each subject to a 750 s, 20 kW·m^{-2} exposure. Note the differences in mass loss rate after the external heat flux is switched off. (c) Mass loss rates for the experiments shown in (b).

Total mass loss measurements indicate that a fraction of the fertilizer is not involved in the reaction and remains in the holder as a condensed phase. This remaining material accounts for approximately 52±3% of the initial mass and, once cooled, has a porous structure white in colour and is inert, suggesting that it is of mineral origin as described in Section 1.4.1. This inert fraction is in agreement with previous measurements of 49% in the propagation experiments and 45–52% in the TGA.

Additionally, the FPA allows measurement of O_2, CO and CO_2 concentrations in the product gases and the convective heat release rate. Analysis of the product gases shows that these remain at ambient levels during the experiment, indicating that the SSD reaction does not produce or consume O_2, CO or CO_2 and thus does not contain any carbonaceous material. Figure 1.9 shows the heat released by the reaction against an empty, reference holder. The heat release is calculated by measuring the temperature and flow of gases in the exhaust duct.

Figure 1.9 shows data after the external heat flux is switched off, i.e. after 750 s of exposure corresponding to the third mass loss regime. The SSD is weakly exothermic with the heat released ranging from 0.08 to 0.11 kW above the background. To find the heat of reaction, the heat released is divided by the mass loss rate. From above, this is in the range 0.06–0.11 $g \cdot s^{-1}$. Therefore, the heat of reaction is 0.73–1.8 $MJ \cdot kg^{-1}$ – approximately 15 times lower than that of wood [21].

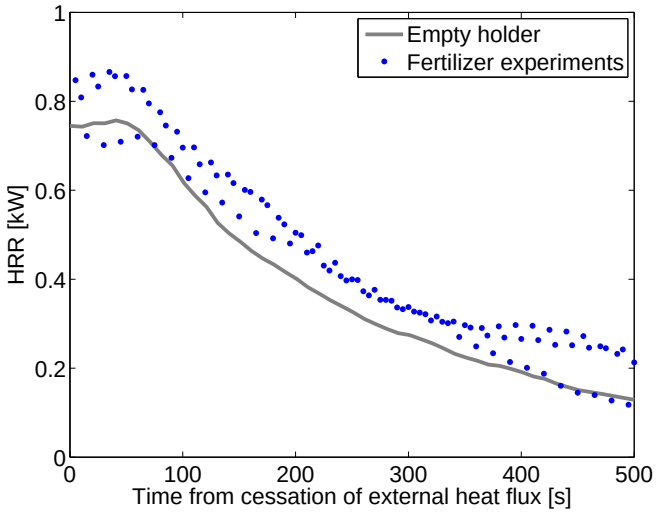

Figure 1.9. The increased heat released for experiments with fertilizer (blue) and the background (black). Time starts after the cessation of the heat flux at 750 s.

1.4.4 Proposed decomposition framework

From the experimental measurements and observations, a three-step decomposition framework with four species is proposed. Analysis of the samples after reaction in the two experimental series shows four species: virgin material, molten material, molten material which has partially undergone reaction (β-melt) and inert matrix (see Fig. 1.3b).

The minimum exposure time seen in Fig. 1.7 shows that there is a minimum amount of material which must be heated in order to initiate self-sustaining decomposition. The first step of the proposed framework is the melting of the fertilizer, which is endothermic. This is correlated to mass loss regime 1 in Section 1.4.3. This molten material undergoes reaction to form an intermediate product (β-melt) which then undergoes further reaction to form the inert product. This corresponds to mass loss regime 2 in Section 1.4.3. After enough heat has been supplied, the reaction front is large enough that the heat released is sufficient to promote melting and heating of the virgin fertilizer up to the reaction temperature, and the reaction can propagate unaided (this is what happens in mass loss regime 3).

The proposed reaction framework is as follows:

$$\text{Virgin fertilizer} \rightarrow \text{Melt} \quad \text{up to } 200^{\circ}\text{C (endothermic/melting)}, \tag{1.3}$$

$$\text{Melt} \rightarrow \beta\text{-melt} \quad 200\text{–}350^{\circ}\text{C (exothermic)}, \tag{1.4}$$

$$\beta\text{-melt} \rightarrow \text{Inert} \quad 200\text{–}350^{\circ}\text{C (exothermic)}. \tag{1.5}$$

1.5 Application to the *Ostedijk* event

These results can be applied to the events aboard the *Ostedijk* in 2007 to give further insight into this incident. However, it is not within the scope of this paper to comment on the possible cause and origin of the ignition source.

Photographic evidence in the Spanish media of the 2007 event aboard the *Ostedijk* clearly shows the development of the plume from the cargo hold [7]. Estimating the

mass of cargo lost in the plume from photographs gives an indication of the size and growth rate of the SSD and, using data from the laboratory tests, the heat released can be estimated.

The plume flow rate was calculated using two methods. For the second, third and fourth days (no data were available for day 1), wind speed from historical records [22] and angle of plume deflection were used to resolve for the velocity vector normal to the ship deck, as in Eq. 1.6 where θ is the angle between the plume centreline and the line normal to the deck surface.

$$\text{plume velocity} = \frac{\text{wind speed}}{\tan\theta} \tag{1.6}$$

Estimating the vent diameter in the cargo cover, through which the gas flowed, the flow rate could then be obtained. The angle of plume deflection varies from 10° from the horizontal on the first day to 40° on the fourth day. The volumetric flow rate could be converted to a mass flow by multiplying by the plume density at the gas temperature (taken to be 200°C, as this is below the decomposition temperatures found in Section 1.4.2) estimated to be 0.74 kg·m^{-3} (assuming the plume has the same molecular weight as air). On the fifth day, the flow rate was estimated using Gaussian plume theory [23], as described by

$$\text{Release rate (kg·s}^{-1}) = \frac{2\pi\sigma_y\sigma_z C u}{exp(-\frac{1}{2}(\frac{z}{\sigma_y})^2)(exp(-\frac{1}{2}(\frac{z-H_e}{\sigma_y})^2) + exp(-\frac{1}{2}(\frac{z+H_e}{\sigma_z})^2))}, \tag{1.7}$$

as opening the holds had led to a much larger, well defined plume suitable for such analysis. In Eq. 1.7, C is the gas concentration along the edge of the plume (as this is well defined in the photographs, a trace concentration of 1×10^{-6} was chosen), u is the wind speed (6 m·s^{-1} from historical data [22]), $\sigma_y = 0.08x(1+0.0001y)^{-0.5}$ and $\sigma_z = 0.06x(1+0.0001x)^{-0.5}$ are the lateral and vertical dispersion coefficients respectively, H_e is the elevation of the plume centreline above ground and z is the height above ground of the region of interest.

Applying the results from the experimental investigations to the events aboard

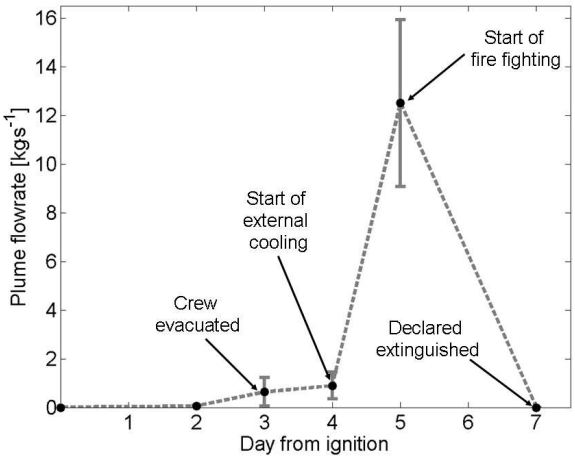

Figure 1.10. Estimated plume flow rates during the event. The error in day 2, 3 and 4 arises from using different images to calculate flow rate, meanwhile the error in day 5 arises due to the sensitivity of Eq. 1.7 the input parameters. The fire was declared extinguished on day 7. Other events are indicated.

the *Ostedijk* allows us to draw some additional conclusions regarding the accident. The observed orange plume on the third day corresponds well to those observed in the early stages of our experiments and would indicate that the fire was propagating through the cargo. The white plume observed during most of the event would indicate sustained propagation with temperatures between 200 and 350°C in the bulk of the material and is in agreement with the temperature of 175°C on the surface of the cargo as reported in [7].

Combining the plume analysis with the measured heat of reaction allows estimation of the heat release rate from Cargo Hold Two of the *Ostedijk*. The flow of gases estimated in Fig. 1.10 equals the mass loss from the cargo hold due to the SSD. Thus, multiplication of the flow rate by the heat of reaction gives the energy released. By this calculation, it is estimated that the amount of energy released by the SSD was of the order of 0.4–0.9 MW the first day and grew to between 5.8 and 29 MW on the fifth day. These calculations are based on the heat of reaction as calculated in Section 1.4.3.

1.6 Conclusions

The small-scale experiments performed have given insight into the SSD behaviour of inorganic fertilizers. From the experiments, a minimum temperature of 200°C is required

to initiate SSD and the steady-state reaction temperature in the bulk of the material ranges between 200 and 350°C. The propagation process has been characterized and a phenomenological decomposition framework is proposed based on the experimental observations.

The analysis of the event has further indicated that the bulk cargo of NPK fertilizer aboard the *Ostedijk* underwent a self-sustaining decomposition reaction. The plume analysis shows rapid growth of the fire and allows estimation of the mass loss, heat release rate and the front size. Although NPK 15.15.15 is classified as a class C fertilizer (i.e. one which will not sustain decomposition in the Trough Test), the fertilizer cargo ignited and an SSD fire grew rapidly for seven days. Our analysis of NPK 16.16.16 (also Class C) indicates that it can also undergo SSD under the correct conditions. This highlights the limitations of the Trough Test and the lack of attention given to fertilizer fires by the research community.

Acknowledgements

The authors are grateful for the financial support of the Engineering and Physical Sciences Research Council and International Fire Investigators and Consultants Ltd. Thanks to Freddy Jervis for assisting in the use of the FPA (donated by FM Global), Anna Stec at the University of Central Lancashire for providing the TGA data and Robert Redpath at the Scottish Agriculture College for supplying the fertilizer.

References

[1] D. Drysdale. *An Introduction to Fire Dynamics*. John Wiley and Sons Ltd, Chichester, UK, 2nd edition, 1998.

[2] P. C. Bowes. *Self-heating: Evaluating and Controlling the Hazards*. Her Majesty's Stationery Office, 1984.

[3] V. Babrauskas. *Ignition Handbook*. Fire Science Publishers, 2003.

[4] H. Kiiski. Self sustaining decomposition of ammonium nitrate containing fertilisers. *Presented at 70th International Fertiliser Association Conference, Paris*, 2002.

[5] G. Marlair and M.-A. Kordek. Safety and security issues relating to low capacity storage of AN-based fertilisers. *Journal of Hazardous Materials*, 123:13–28, 2005. doi: 10.1016/j.jhazmat.2005.03.028.

[6] A. M. Palomo. Report on the accident at Escombreras – Cartagena ("Informe sobre el accidente en Escombreras - Cartagen"). *Revista de Protección Civil 11, Madrid, Spain*, March 2002. URL www.proteccioncivil.org/eu/DGPCE/Informacion_y_documentacion/catalogo/carpeta06/revispc11/rpc11_16.htm.

[7] R. M. Hadden, F. X. Jervis, and G. Rein. Investigation of the Fertilizer Fire aboard the *Ostedijk*. *Fire Safety Science*, 9:1091–1101, 2008. doi: 10.3801/IAFSS.FSS.9-1091.

[8] Yara International. Decomposition of NPK 15-15-15 on m/v 'Ostedijk' in February 2007 – Internal Investigation Report. 2007.

[9] Direccion General de la Marina Mercante. Personal Communication, Subdireccin General De Seguridad Martima y Contaminación, Ministerio De Fomento, Spanish Government, Madrid, Spain, 2007.

[10] Technical Group on the MEPC ON OPRC-HNS. Summary of the Incidents Involving HNS and Lessons Learnt. Technical report, International Maritime Organisation, 2008. URL www.imo.org. Accessed September 2008.

[11] Agencia EFE, with permission. 2007.

[12] J. I. Kroschwitz, editor. *Kirk-Othmer Encyclopedia of Chemical Technology*. John Wiley and Sons, 1994.

[13] *Handbook for the Safe Storage of Ammonium Nitrate Containing Fertilizers*. International Fertilizer Industry Association and the European Fertilizer Manufacturers Association, 1992.

[14] United Nations. *UN Recommendations on the Transport of Dangerous Goods - Manual of Tests and Criteria*. United Nations, New York and Geneva, 2002.

[15] Yara International. Yara Milla 16-16-16 Technical Data. Technical report, Accessed

October 2009. URL mediabase.edbasa.com/kunder/yaraimages/agribro/agribro/agribro/j2007/m07/t16/0003350_2.pdf.

[16] Yara International. Yara Milla 15-15-15 Technical Data. Technical report, Accessed October 2009. URL mediabase.edbasa.com/kunder/yaraimages/agribro/agribro/agribro/j2007/m09/t19/0003597_2.pdf.

[17] G. Rein, N. Cleaver, C. Ashton, P. Pironi, and J. L. Torero. The severity of smouldering peat fires and damage to the forest soil. *Catena*, 74(3):304–309, 2008. ISSN 0341-8162. doi: 10.1016/j.catena.2008.05.008.

[18] M. M. Hirschler and A. B. Morgan. *SFPE Handbook of Fire Protection Engineering*, chapter 1-7: "Thermal Decomposition of Polymers", pages 1–112–1–143. National Fire Protection Association, Quincy, MA 02269, 4th edition, 2008.

[19] A. Tewarson. *SFPE Handbook of Fire Protection Engineering*, chapter 3-4: Generation of Heat and Chemical Compounds in Fires, pages 3–82–3–161. National Fire Protection Association, 2002.

[20] M. Janssens. *SFPE Handbook of Fire Protection Engineering*, chapter 3–2: "Calorimetry", pages 3–60–3–89. National Fire Protection Association, Quincy, MA 02269, 4th edition, 2008.

[21] P. DiNenno, editor. *SFPE Fire Protection Handbook*, chapter Appendix C. National Fire Protection Association, 2002.

[22] National Severe Storms Laboratory Historical Weather Data Archives. Historical Weather Data Archive, Accessed October 2009. URL data.nssl.noaa.gov.

[23] S. R. Hanna and D. Strimaitis. *Workbook of Test Cases forVapour Cloud Source Dispersion Models*. Center for Chemical Process Safety, American Institute of Chemical Engineers, 1st edition, 1989.

2

Radiant ignition of polyurethane foam: the effect of sample size

Summary

Although smouldering ignition of upholstery items remains a leading cause of residential fire deaths, relatively little research is conducted on the topic. An experimental investigation of the effect of sample size on the ignition and spread of smouldering and flaming in polyurethane foam under natural flow conditions is reported here. Polyurethane foam samples are used because this is a common material in modern, residential environments and one for which there exists previous test data. Samples of different square cross-section size and a fixed height of 150 mm are insulated on all sides expect the top which is exposed to a radiant heat flux and is open to the air. Samples with side lengths of 50, 100, and 140 mm are studied. Ignition and spread dynamics are diagnosed using thirteen thermocouples located along the vertical centre line. The onset of smouldering ignition (13, 8 and 7 $kW \cdot m^{-2}$ for 50, 100 and 140 mm sample sizes respectively) is observed at significantly lower heat fluxes that flaming (45, 32 and 30 $kW \cdot m^{-2}$ respectively). Critical heat fluxes for smouldering and flaming ignition increase with decreasing sample size, with smouldering ignition being significantly more sensitive to sample size than flaming ignition under the size range studied. Smouldering spread rates are measured in the range from 3 to 25 $mm \cdot min^{-1}$ and found to be a strong function of the heat flux, depth and sample size. The effect of sample size on smouldering ignition has been theoretically proposed before but this is the first

time that this effect has been demonstrated experimentally. The fact that large samples result in the lowest critical heat flux could have implications for testing procedures and translation of results from small-scale testing to real-scale in the built environment.

2.1 Introduction

Previous work on smouldering ignition of polyurethane (PU) foam has focused on the effects of flow through the porous fuel [1–3], enhanced or reduced oxygen concentration [4] and the heat flux and exposure time [5]. In this work we present the effect of sample size on the ignition and spread of smouldering under atmospheric oxygen concentrations and natural flow conditions.

Smouldering is a slow, low-temperature, heterogeneous form of combustion in which oxygen directly attacks the surface of a solid fuel [6–8]. Ignition is governed by the balance between heat flux applied to the surface, heat losses and fuel kinetics [6, 8], while the self-sustained propagation is governed primarily by the oxygen supply to, and heat losses from the reaction front [8–10]. The heat losses are a function of surface area and the heat liberated from the reaction depends on the volume of the reaction front; therefore, smouldering combustion is sensitive to the size of the sample [1, 2, 8]. This work aims to experimentally identify the effect of size on the ignition and subsequent propagation of smouldering in PU foam over a wide range of heat fluxes, resulting in smouldering and flaming ignition, and using three sample sizes.

The effect of sample size on the smouldering ignition of dusts has been studied by Krause and Schmidt [11, 12] and Schmidt et al. [13]. These investigations use hot particles [11] or elevated ambient temperatures [12, 13] to initiate the smouldering reaction. Ignition of larger sample sizes is found to require lower critical ambient temperatures than for smaller sizes due to the reduced heat losses from the reaction front. However, larger sample sizes result in lower temperatures and slower propagation of the smouldering front during the reaction. This is attributed to lower rates of oxygen diffusion through the sample to the reaction zone. Schartel et al. [14, 15] studied the effect of sample thickness on flaming ignition of polymers and show that the ignition delay time is reduced and peak heat release rate is increased for thermally thin samples

compared to thick samples. These studies did not address smouldering ignition nor the effect of sample surface area. Ritchie et al. [16] studied the effect of sample size on the heat release from flaming wood. They found that, other than the initial peak, the heat release rate is nearly independent of the sample area. They did not study the effect of size on the critical heat flux for ignition nor smouldering combustion.

The theoretical critical minimum size for sustained smoulder propagation in which the heat losses are balanced by heat generation under conditions of forced flow and no gravity is given by Eq. 2.1 [8],

$$L_c = \frac{4\delta}{Q_{\text{sml}}} \frac{U_{\text{loss}} \left(T_{\text{sml}} - T_0\right)}{\dot{m}''}, \tag{2.1}$$

where L_c is the critical length of the sample (sample side length for a square cross section or diameter of a circular cross section), δ is the thickness of the smouldering front, Q_{sml} is the heat released by the smouldering reaction, U_{loss} is the global heat loss coefficient, T_{sml} is the smouldering temperature, T_0 is the ambient temperature and $\dot{m}''$ is the mass flux of oxidizer to the reaction zone.

Using typical experimental data for smouldering PU foam with forced oxidizer flow (δ = 0.04 m, Q_{sml}= 5880 kJ/kg-O_2, U_{loss} = 14 W·m^{-1}·K^{-1}, T_{sml} = 450°C and T_0 = 20°C) [1, 2], a minimum sample size on the order of 160 mm is found to be required to sustain smouldering propagation [8]. Equation 2.1 is only valid for forced flow through the PU foam; however, the scenarios of most importance in fire safety occur under natural flow conditions. In these situations, Eq. 2.1 cannot be applied and it is necessary to study the critical size problem without forced flow.

Polyurethane foam can undergo smouldering and flaming combustion. At low heat fluxes, a smouldering reaction will be initiated and will propagate through the sample; at higher heat fluxes, flaming ignition will occur. There are two possible mechanisms which may lead to flaming: either transition from a smouldering reaction or auto-ignition in the gas phase. Transition is a complex phenomena which, though significant in fire safety, has received relatively little study. Putzeys et al. [17] found that the smoulder velocity and peak temperature are strongly correlated to the occurrence of transition from smouldering to flaming. The transition has also been observed to occur

when pores are formed in the region behind the smouldering front [18]. This implies that the smouldering front acts as the source of combustible vapours and heat for the flaming ignition. As a result, the onset of flaming ignition may also be affected by the sample size. Flaming ignition may also occur due to spontaneous ignition of the fuel vapours. This requires that the mixture of vapours and air is heated to a temperature sufficient to initiate a gas-phase reaction [7].

2.2 Experimental set-up

The experimental set-up used for these experiments (shown in Fig. 2.1) was based on those of Anderson et al. [5] and Gratkowski et al. [19]. The set-up is deliberately based on the cone calorimeter, except that there is no gas analysis and the sample depth is increased to 150 mm. A calibrated cone heater provided a uniform heat flux up to 50 $kW \cdot m^{-2}$ over the free surface of the sample. The sample was held in a stainless steel sample holder which was inlaid with insulation board to minimize heat losses as well as prevent ingress of oxygen from any face other than the heated free surface. The bottom of the sample holder was not inlaid with insulation. As a result, oxygen could only diffuse downward from the free surface. In order to minimize the formation of recirculation eddies induced by the buoyant flows generated by the heater, a 100 mm wide flange was added to the top of the sample holder.

Samples of PU foam with square cross sections of length 50 mm, 100 mm and 140 mm were tested. The depth of all samples was 150 mm. The largest sample was 140 mm as this is maximum size that can fit under the cone heater and still be subject to a heat flux across the entire surface. The total error in the heat flux measurement was calculated to be ± 0.5 $kW \cdot m^{-2}$, due to the positioning of the heat flux meter and the sample position being accurate within ± 5 mm. This is in addition to a 3% uncertainty of the calibration.

Heat flux along the radius from the sample centre was measured and a maximum reduction of 30% of the centreline value was found at the edge of the 140 mm sample. However, because ignition occurs at the centre of the sample where the heat flux is greatest and heat losses are minimum, this variation in heat flux was not expected to

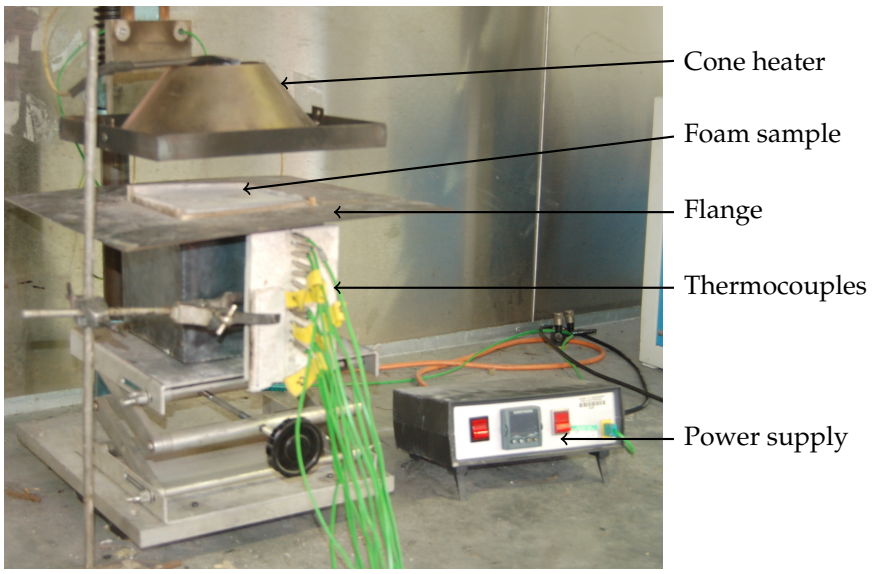

Figure 2.1. The experimental apparatus.

have a significant impact on the results. The sepration between the heater and the sample was fixed at 25 mm.

The samples were instrumented with thirteen sheathed K-type thermocouples of 1.5 mm diameter. These entered the sample perpendicular to the applied heat flux and were located on the central axis 5 mm below the exposed surface, and subsequently at 10 mm intervals to a depth of 125 mm. Thermocouples were held in place using a stand with holes at locations corresponding to the measurement points on the sample. Temperature data were recorded every second using an Agilent 34980A Multifunction Switch interfacing with a computer running Matlab 2008b. Visual observations and temperature measurements allowed the differentiation between no ignition, smouldering ignition and flaming ignition.

A commercially available PU foam sourced from the UK was used. The density was in the range 20–22 $kg \cdot m^{-3}$. The foam is the same as that used by Bustamante et al. [20] who found the elemental composition to be 61.9% carbon, 22.5% oxygen, 8.5% hydrogen and 5.9% nitrogen with trace quantities of sulphur and chlorine. Based on this composition, the chemical formula is $CH_{1.53}O_{0.27}N_{0.08}$.

Prepared samples were placed under the heater and shielded from the heat flux using fibreboard insulation. When the heater had reached the temperature corresponding to the desired heat flux at the sample surface, the fibreboard was rapidly removed

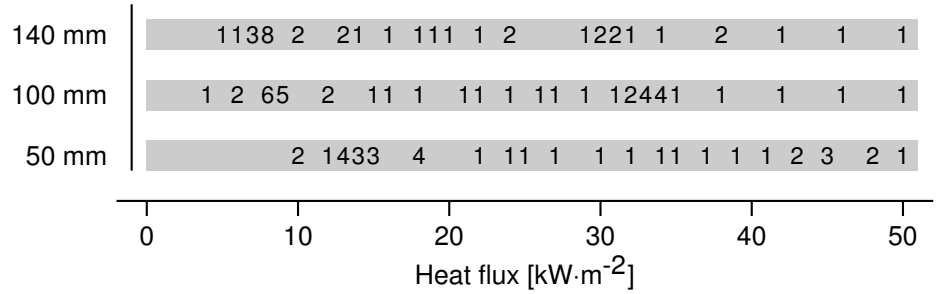

Figure 2.2. Test matrix showing the heat fluxes at which each sample size was tested. The numbers indicate how often each experiment was undertaken.

exposing the sample to the heat flux. No pilot flame or sparking device was used in the set-up.

Initially, the critical heat flux required for smouldering and flaming ignitions was found using a systematic, iterative, bisection method. The samples were exposed to a heat flux and, if (flaming or smouldering) ignition occurred, a lower heat flux was selected and a new sample tested. If no ignition occurred, a higher heat flux was used. Once the critical heat fluxes for flaming and smouldering ignition and had been found, the ignition behaviour at heat fluxes between the two critical heat fluxes and up to 50 $kW \cdot m^{-2}$ was studied. This method allows the fastest determination of the critical heat flux for ignition. The number of experiments carried out for each heat flux and sample size are shown in Fig. 2.2. The experiment was terminated if no ignition was observed after 30 min or when the thermocouple traces reached steady state conditions.

2.3 Results

Figure 2.3 shows samples before and after experimentation. As the heat flux is increased and the ignitions become stronger, the samples become increasingly destroyed. These images provide qualitative evidence of the reaction which is augmented by detailed temperature measurements.

Temperature data measured in the samples are used to distinguish the different types of ignition upon exposure of the sample to a heat flux. The types of ignition are classified as follows: no ignition, partial smoulder, complete smoulder and flaming ignition. Peak temperatures for smouldering were typically in the range 300–400°C, while

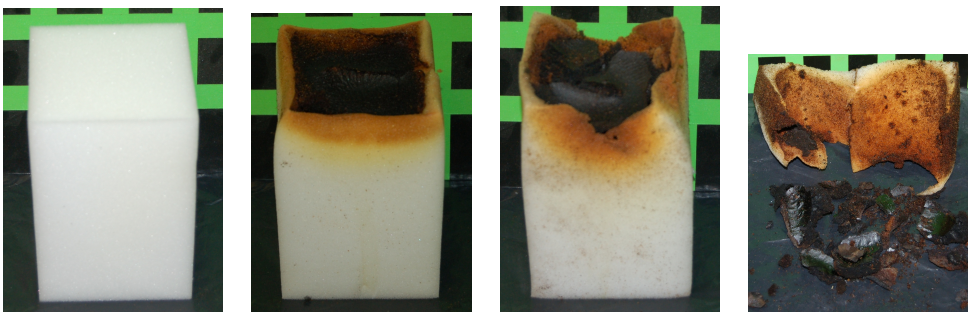

(a) (b) (c) (d)

Figure 2.3. Images of 100 mm samples showing (a) virgin foam, (b) charred foam in which a smoulder front did not propagate, (c) a sample in which smouldering occurred and (d) a sample which underwent flaming ignition.

peak temperatures measured during flaming were 600–700°C, except in the case of the 50 mm samples when flaming was visually observed but temperatures in the sample remained around 350–450°C. After the combustion was complete, the thermocouples were allowed to reach steady state before the experiment was terminated.

The reference temperatures measured in the apparatus for 100 mm samples without a foam sample at heat fluxes of 14, 28, 44 and 56 $kW \cdot m^{-2}$ are shown in Fig. 2.4a. As the heat flux is increased, the steady state temperatures reached by the thermocouples increases linearly. Temperatures are constant up to a depth of 65 mm after which the temperature begins to decrease. Figure 2.4b shows that mean steady state reference temperature scales linearly with applied heat flux. Error bars indicate the maximum and minimum recorded temperatures. If the thermocouples exceed the steady state temperatures given by this analysis during an experiment, it can be assumed that there is a significant exothermic reaction occurring. Therefore, these are presented as a reference to show the temperature when, for a given heat flux, reaction is occurring. Steady state temperatures after the reaction may be higher because the thermocouples are heated by the smouldering front and insulated by the residue, which prevents them from returning to ambient temperature.

The temperature data discussed in the following sections are presented in two ways. The first is analysis of the temperature–time series, showing the temperature evolution at each thermocouple in the sample over the time of the experiment. This allows the development of the reaction over time to be assessed. The second is an analysis of

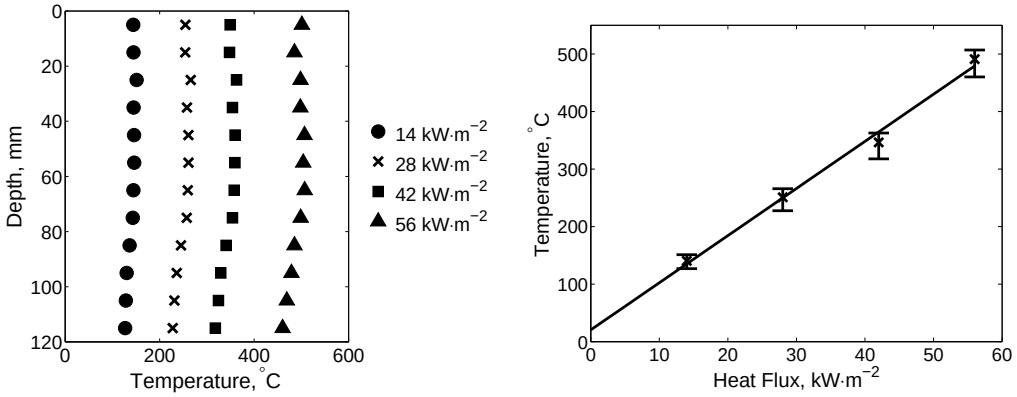

Figure 2.4. (a) Steady state temperatures of exposed thermocouples without the foam sample for four heat fluxes and (b) relationship of heat flux and temperature. The marker is the mean and the error bars relate to the maximum and minimum measured values.

the temperature distribution through the sample depth at three or four different times during the reaction. These points are chosen to be just after exposure to the heat flux, during the smouldering or flaming reaction and during the final steady state period. This method allows us to see the propagation of a heat wave through the sample. The error is given as the mean error for all experiments where repeats were carried out. This was calculated to be 17%.

2.3.1 50 mm samples

Figure 2.5 shows temperature data for four experiments at heat fluxes 10, 18, 37 and 39 kW·m^{-2}. After 40 min, exposure to a heat flux of 10 kW·m^{-2} did not lead to ignition of the foam and only in-depth conduction was observed with no exothermic or endothermic reactions taking place (Fig. 2.5a). The temperature profile shown in Fig. 2.5b shows that the temperature throughout the sample increases in time with the maximum temperature always observed at the free surface. The temperature decreases with depth, as expected in an inert solid. The maximum observed temperature is 275°C.

A heat flux of 18 kW·m^{-2} (Figs 2.5c and 2.5d) shows the onset of exothermic reactions at 3–4 min. This is shown in the temperature profiles as an increase in temperature at depths of 25 and 35 mm at 5 min compared to the temperature at 15 mm. The maximum temperature is 337°C.

A stronger smouldering reaction was observed upon exposure to a heat flux of

37 kW·m^{-2} (Fig. 2.5e). The temperature profile Fig. 2.5f shows that after 5 min of exposure, the front has spread to a depth of 65 mm and shows a significant temperature gradient between 65 and 85 mm. The maximum observed temperature was 461°C.

Figure 2.5g shows an experiment where a higher heat flux (39 kW·m^{-2}) resulted in flaming and more extensive consumption of the foam, allowing the thermocouples above the flame to measure the temperature of the hot gases (up to 700°C). The flaming did not propagate through the sample and the reaction was quenched at around 105 mm (Fig. 2.5h). The temperature profile shows that there is rapid propagation through the sample as after 1 min, heat has reached the thermocouple 55 mm from the free surface.

2.3.2 100 mm samples

Figure 2.6 shows temperature traces for experiments at four heat fluxes – 8, 8.3, 32.5 and 33 kW·m^{-2}. No ignition was observed at a heat flux of 8.0 kW·m^{-2} (Fig. 2.6a). The peak in the thermocouple near the surface at about 4 min (298°C) was due to degradation of the foam at the surface and exposure of the thermocouple directly to the radiant heat. This is observed in Fig. 2.6b where at 15 min the peak temperature is seen at the thermocouple 15 mm below the surface.

Partial smoulder ignition at a heat flux of 8.3 kW·m^{-2} propagated approximately 55 mm into the sample after 20 min of heating (Fig. 2.6c). Temperatures exceed 300°C for a significant time as the smoulder front propagates through the sample. The maximum temperature is 377°C at a depth of 15 mm. The propagation can be seen in Fig. 2.6d as the peak temperature moved from 15 mm at 8 min to 25 mm after 15 min.

A heat flux of 32.5 kW·m^{-2} (Fig. 2.6e) results in complete smoulder of the sample enhanced by the higher heat flux. The temperature behind the smouldering front is 250–305°C, compared to 75–275°C in Fig. 2.6c. The front propagated from 15–65 mm between 1 and 3 min after exposure. The final steady state temperatures are around 300°C as shown in Fig. 2.6f.

Flaming ignition is seen at a heat flux of 34.6 kW·m^{-2} in Fig. 2.6g where the maximum temperature is 715°C. Figure 2.6h shows the rapid spread through the foam and the steady state temperatures lower than those observed for the complete smoulder case. This is because the foam surrounding the thermocouples has been consumed by

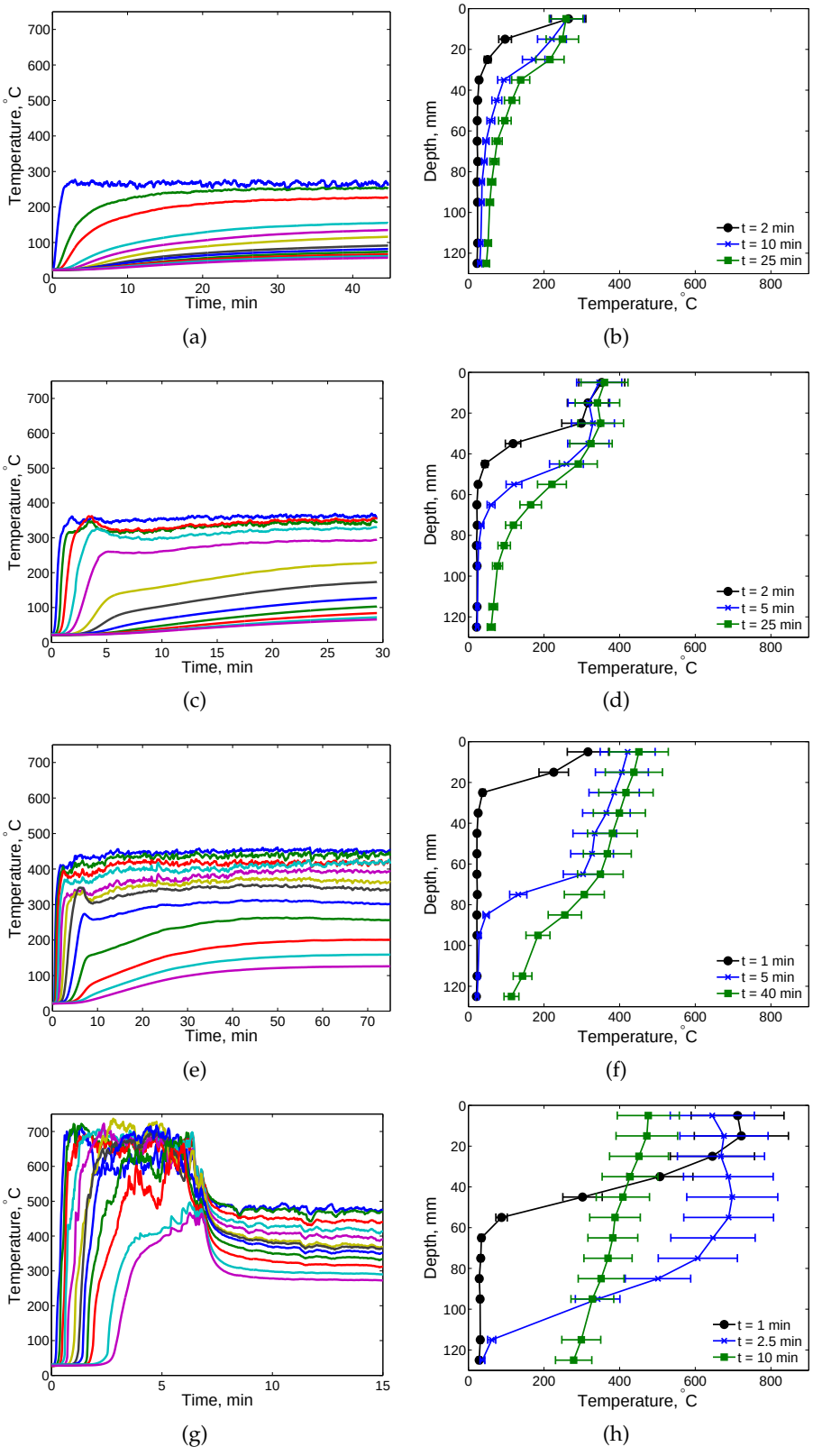

Figure 2.5. Temperature profiles for selected experiments on 50 mm sample (a & b) 10.0 kW·m^{-2}, (c & d) 18.0 kW·m^{-2}, (e & f) 37.3 kW·m^{-2}, (g & h) 39.0 kW·m^{-2}. The leftmost line corresponds to temperature 5 mm beneath the surface. Moving right, the lines represent depths increasing by 10 mm up to 125 mm.

the flaming fire exposing them to increased heat losses. After flaming ignition, the front propagated through the sample in 2.5 min compared to 20 min for smouldering.

2.3.3 140 mm samples

Figures 2.7a and 2.7b show an experiment at a heat flux of 7.3 $kW \cdot m^{-2}$ in which no smouldering occurred. Smouldering is observed at 7.8 $kW \cdot m^{-2}$ (Fig. 2.7c) with ignition occurring after 10 min exposure. The maximum temperature was 398°C. The smoulder front propagated to 55 mm at 22 min after exposure as shown in Fig. 2.7d.

At 28.8 $kW \cdot m^{-2}$, complete smoulder of the sample is observed (Fig. 2.7e) reaching a maximum temperature of 383°C. The temperature profile Fig. 2.7f shows propagation of the smoulder front with steep temperature gradients over short distances indicating the position of the hot oxidation and colder pyrolysis fronts. A steady state temperature of 275–375°C is observed. Compared with the measurements on the sample of 100 mm at a heat flux of 32.5 $kW \cdot m^{-2}$ (Fig. 2.6e), the spread rate is 30% higher, even at a lower heat flux. This is a clear indication of a stronger smouldering reaction as the sample size is increased and the heat losses are reduced.

Flaming ignition is shown in Fig. 2.7g for a heat flux of 30.6 $kW \cdot m^{-2}$. Rapid propagation is observed in Fig. 2.7h with the front moving from a depth of 35–85 mm in 30 s. A maximum temperature of 711°C is reached. As in the 100 mm samples, the thermocouples reach a lower steady state temperature than in the smouldering cases.

2.3.4 Summary of results

Figure 2.8 shows the number of times at which each sample size was tested at a given heat flux. The shading represents the ignition type with light gray representing no ignition, mid gray representing smouldering ignition and dark gray flaming ignition. We can clearly see that the flaming ignition of the 50 mm samples is more erratic than the larger samples. We can also see that there is a significant decrease in the critical heat fluxes required for both smouldering and flaming ignition as the sample size is increased. The numbers indicate how many experiments were undertaken at a given heat flux.

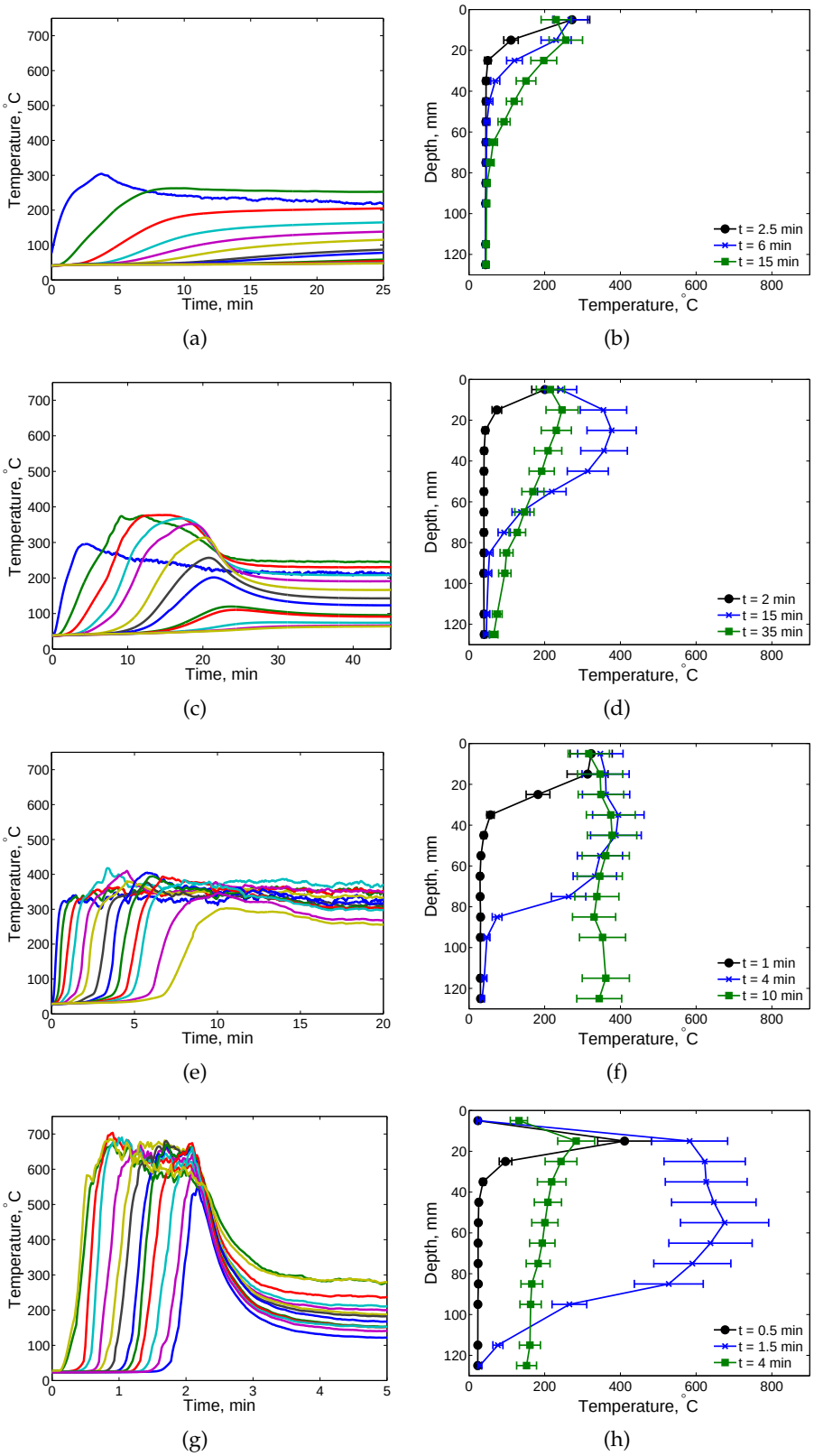

Figure 2.6. Temperature profiles for selected experiments using 100mm sample (a & b) 8.0 $kW \cdot m^{-2}$, (c & d) 8.3 $kW \cdot m^{-2}$, (e & f) 32.5 $kW \cdot m^{-2}$, (g & h) 34.6 $kW \cdot m^{-2}$. Distance form the surface increases from left to right. The leftmost line is the temperature at the thermocouple 5 mm below the surface increasing in depth at 10 mm intervals to 125 mm.

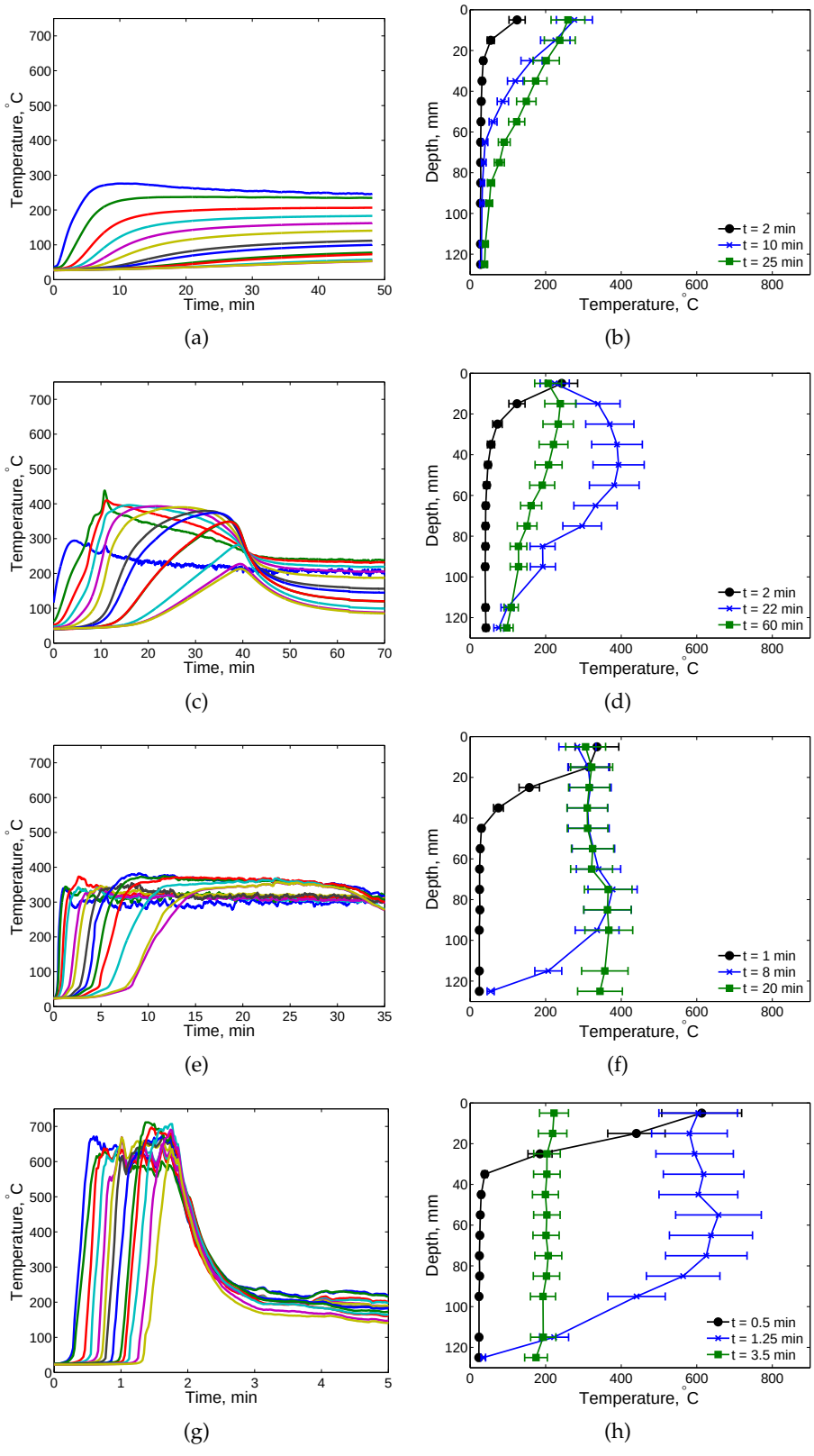

Figure 2.7. Temperature profiles for selected experiment using 140 mm samples (a & b) 7.3 kW·m^{-2}, (c & d) 7.8 kW·m^{-2}, (e & f) 28.8 kW·m^{-2}, (g & h) 30.6 kW·m^{-2}. Distance form the surface increases from left to right. The leftmost line is the temperature at the thermocouple 5 mm below the surface increasing in depth at 10 mm intervals to 125 mm.

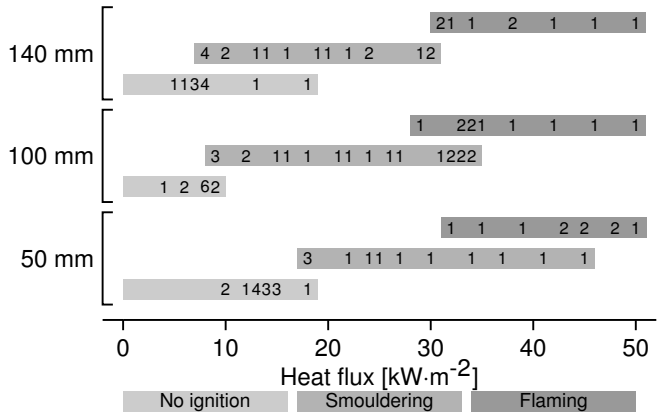

Figure 2.8. Test matrix showing the heat flux and sample size relationships tested and the resulting ignition types. Numbers indicate how many times samples were tested at the heat flux.

Table 2.1. Critical heat flux for ignition of the sample sizes studied and those found in the literature.

Sample size [mm]	Critical heat flux for smouldering ignition [$kW \cdot m^{-2}$]	Critical heat flux for flaming ignition [$kW \cdot m^{-2}$]
50	18–19	32–45
100	8–9	32–37
140	7–8	30–31
100 [20]	N/A	35
300 [5]	6	N/A

2.3.5 Critical heat flux for ignition

Smouldering and flaming ignitions for the three sample sizes were observed visually as well as using the temperature data seen in Figs 2.5–2.7. The critical heat flux ranges are detailed in Table 2.1. The results are in agreement with the work of Anderson et al. [5] and Bustamante et al. [20].

The trend observed is that as sample size is increased, the critical heat flux for smouldering and flaming ignition is reduced. This is in agreement with the theory that smouldering is significantly influenced by heat losses from the sample sides and scales with the surface area to volume ratio [8]. The dependence on heat flux seems to be reduced at sizes greater than 140 mm suggesting that the critical heat flux becomes independent of sample size for large samples.

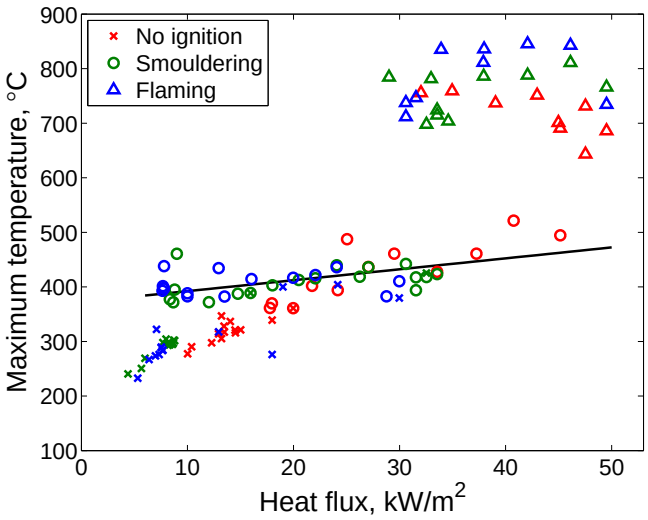

Figure 2.9. The maximum temperatures observed during experiments. Crosses represent no ignition, circles represent smouldering and triangles represent flaming ignition. Red, green and blue represent 50, 100 and 140 mm samples respectively. We see that in the no ignition cases, the temperature increases with heat flux before there is a step which coincides with the onset of smouldering. There is another step up to temperatures in the region of 700°C corresponding to the onset of flaming ignition.

2.3.6 Maximum temperature and time to ignition

Figure 2.9 shows the maximum temperatures observed in each experiment. The figure shows three regimes: the first, at low heat fluxes when ignition does not occur, shows a steady increase in maximum temperature with heat flux up to around 300°C. These cases of no ignition are marked by crosses. As the heat flux is increased, a step in the maximum temperature up to around 400°C is observed. This region is represented by circles and corresponds to smouldering ignitions. This step is more pronounced for the 100 and 140 mm samples than the 50 mm samples, suggesting a different behaviour for the onset of smouldering at this size. The maximum temperature then increases with heat flux up to approximately 425°C before a second step to temperatures in the region of 700°C. This corresponds to flaming ignition and is denoted by triangles. The critical heat fluxes found by this analysis are in the ranges in Table 2.1. This diagnostic validates the definition of 350°C as the ignition criterion for smouldering.

The time to ignition for experiments in which smouldering or flaming occurred is shown in Fig. 2.10. Ignition was defined as the thermocouple located 25 mm from the free surface reaching 350°C. This condition was defined *a posteriori* based on the

analysis presented above. For smouldering ignitions, time to ignition ranged from 2–20 min, whereas for flaming this was typically less than 2 min and flames were generally observed less than 5 s after exposure to the heat flux.

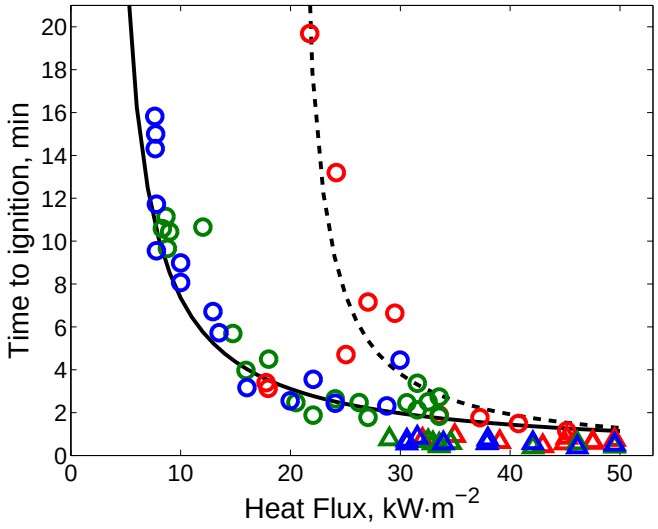

(a)

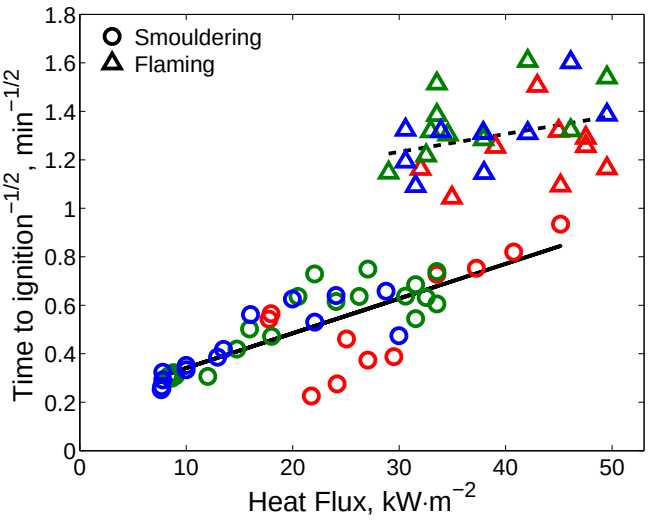

(b)

Figure 2.10. Time to ignition showing (a) asymptotic behaviour and (b) $1/\sqrt{t_{ig}}$ for smouldering (circles) and flaming (triangles) samples. Red, green and blue symbols represent 50, 100 and 140 mm sample sizes respectively.

Figure 2.10a shows the time to ignition as a function of incident heat flux. It is observed that the time to ignition decreases as the heat flux is increased from the critical heat flux for smouldering initiation. At high heat fluxes, the time to ignition decreases significantly to less than 30 s. It is seen that the ignition time of the 50 mm samples follows a different trend from that of the 100 and 140 mm samples.

Figure 2.10b shows the inverse of the square root of time to ignition. All samples follow a linear relationship as predicted by classical ignition theory [21] indicating that as the applied heat flux is increased, the time to ignition decreases. This suggests that the the processes are driven by heat transfer . Again, the 50 mm samples appear to follow a different trend from the 100 and 140 mm samples suggesting that controlling mechanisms of ignition at the size are different from those for larger samples.

2.3.7 Smoulder spread rate

Spread rate was found to be a function of sample size as shown in Fig. 2.11. Spread rate was calculated between the thermocouples located 25 and 35 mm below the free surface. This location is chosen because the heat directly transferred from external heat flux is lower than for locations closer to the surface, while still having good oxygen supply from the free surface to allow smouldering propagation.

The smoulder spread rates range from approximately 5–10 mm·min^{-1} for smouldering at heat fluxes just above the critical heat flux and increase up to around 25 mm·min^{-1} before the onset of flaming. The error in the spread rate is estimated to be $\pm$25% due to the uncertainty of $\pm$2.5 mm in the thermocouple placement in the foam. The spread rates measured for smouldering are in agreement with the work of Anderson et al. [5] using a similar experimental set-up but are higher than those generally found for unassisted smouldering, for example between 0.12 and 1.5 mm·s^{-1} [3, 17] for PU ignited with an electrical coil. The increased spread rate could be explained by the increase in energy supplied to the reaction zone by the cone heater.

Figure 2.11 shows the spread rate as a function of depth for smouldering in a 100 mm sample at heat fluxes of 8, 26 and 33 kW·m^{-2}. There is a steady increase in smoulder spread rate as the heat flux is increased. The spread rates between 15 and 25 mm depth are 6, 18 and 22 mm·min^{-1} respectively. A strong dependence on depth is seen with spread rates decreasing to 3, 8 and 18 mm·min^{-1} at a depth of 50 mm. The spread at 16 and 33 kW·m^{-2} reaches 95 mm; however, the spread rate has reduced to 4 and 13 mm·min^{-1}. The same trend is seen for the 50 and 140 mm samples; however, for the 50 mm samples, the maximum spread depth is 75 mm.

It is known that the ignition of smouldering combustion is controlled by heat

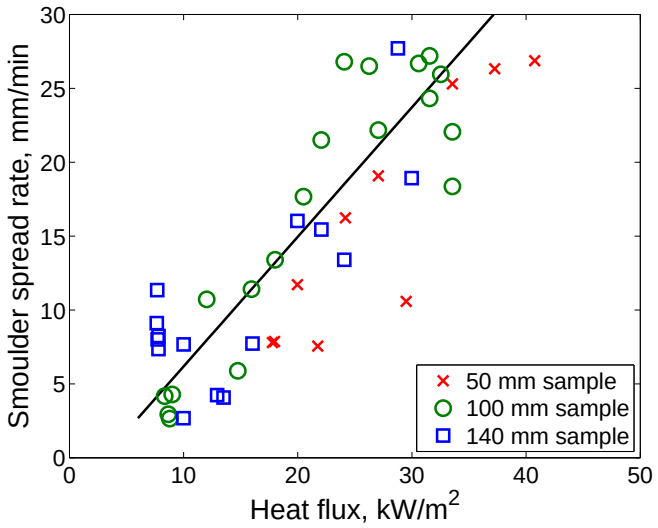

Figure 2.11. Smoulder spread rate as a function of heat flux measured between depths 25 and 35 mm. Circles are 50 mm samples, squares 100 mm samples and triangles 140 mm samples.

transfer and kinetics and the spread is controlled by the availability of oxygen and heat losses [6, 8]. Therefore, this decrease could be explained by the decrease in available oxygen as the smoulder propagates into the sample. This means that oxygen has to diffuse further before it reaches the reaction front and limits the spread rate. This effect has been previously reported by Palmer [22] and Krause [11]. Near the free surface, there is a large supply of oxygen and the reaction is dominated by the heat supplied by the heater.

2.4 Discussion

2.4.1 Sample size

The effect of sample size has been shown to have a strong impact on the smouldering and flaming ignition of polyurethane foams. The critical heat flux for smouldering and flaming are shown to decrease as the sample size is increased. This relationship appears to become less strong for larger samples. The behavior of the 50 mm samples is seen to differ significantly from that of the 100 and 140 mm samples. This suggests that different mechanisms control the ignition at 50 mm compared to larger sizes. This is due either to the small surface area available for oxygen diffusion to the sample which would limit the reaction rate, or increased heat losses to the surroundings for

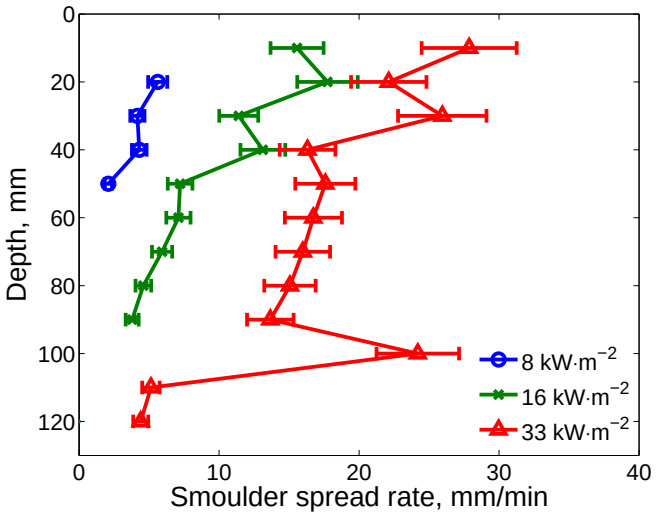

Figure 2.12. Spread rate of the smouldering front as a function of depth for samples of 100 mm subject to heat fluxes of between 8 and 33 kW·m^{-2}. Spread rate is seen to increase with heat flux. The error is calculated at 12% based on the repeatability of experiments.

the 50 mm sample which has a higher surface area to volume ratio than the larger sizes. Unfortunately, it is not possible to conclude on which mechanism is responsible using the data obtained from the current experimental set-up.

2.4.2 Transition to flaming

The transition between smouldering and flaming ignition is a complex phenomenon marked by rapid changes in spread rate and peak temperatures. There are two possible mechanisms for this transition: gas phase ignition or the transition from smouldering to flaming. The gas phase ignition may be due either to auto-ignition or piloted ignition at the cone heater which, at high heat fluxes, operates at temperatures exceeding 700°C.

Transition from sustained smoulder to flaming was not observed in any of the experiments. However, it was not possible to conclude on transition from incipient smouldering to flaming.

There are two reasons that the transition from incipient smouldering to flaming would not be observed with the current diagnostics set-up: flaming ignition would take place at a much faster time scale than that required for a smouldering signature to develop in the temperature data, and transition would occur on a thin layer within the foam, which the spatial temperature resolution used here (10 mm) would be too coarse

to capture.

Bustamante et al. [20] found the minimum heat flux for flaming auto-ignition of the same PU foam as used in this work was 35 $kW \cdot m^{-2}$ (compared to 9 $kW \cdot m^{-2}$ for piloted ignition). These experiments were carried out in the cone calorimeter using samples of square cross section 100 mm. This heat flux for auto-ignition agrees well with the range found here for flaming ignition for the same sample size (32–37 $kW \cdot m^{-2}$). This suggests that the mechanisms leading to flaming ignition in [20] are the same as the mechanisms in this work. Bustamante et al. concluded that flaming ignition was an auto-ignition process but did not consider smouldering and transition to flaming as a possible mechanism.

Putzeys et al. [17] found that a minimum heat flux between 8 and 8.75 $kW \cdot m^{-2}$ will result in the transition from smouldering to flaming of a $50 \times 50 \times 125$ mm sample of PU foam with internal forced flow and sample sides heated to 200°C by external means. This value is much lower than that measured here for 50 mm size (45–48 $kW \cdot m^{-2}$), but the heating of the samples sides and increased air flow will dramatically enhance the smouldering combustion, increasing the likelihood of transition to flaming.

Using the temperature data collected and comparing the tests here to those available in the literature, it is not possible to provide a definite mechanism for flaming ignition. Further investigations using enhanced apparatus such as higher thermocouple resolution to capture the smoulder reaction in more detail, gas analysis, high speed cameras, advanced flame detection techniques or changing the separation between the sample and the cone heater but keeping the heat flux constant could assist in the determination of the process leading to flaming ignition.

2.5 Conclusions

The effect of sample size on radiant smouldering ignition had been theoretically proposed before but this is the first time that it is demonstrated experimentally. The onset of smouldering ignition was observed in the ranges 13-14 $kW \cdot m^{-2}$, 8-9 $kW \cdot m^{-2}$, 7-8 $kW \cdot m^{-2}$ for 50, 100 and 140 mm sample sizes respectively. The onset of flaming ignition was observed in the ranges 45-48 $kW \cdot m^{-2}$, 32-37 $kW \cdot m^{-2}$, 30-31 $kW \cdot m^{-2}$,

respectively.

The onset of smouldering ignition is observed at significantly lower heat fluxes than flaming (approximately 70–80% lower). This offers a route to initiate flaming fires from much weaker ignition sources by the mechanism of transition from smouldering to flaming. Critical heat fluxes for both smouldering and flaming ignition increase with the sample size, with smouldering ignition being significantly more sensitive to sample size than flaming ignition under the range studied. Since most standard testing is conducted a one single sample size on the order of 100 mm, the observation reported here that the lowest flammability is observed for the largest samples could have implications for testing procedures and translation of small-scale testing to real applications in the built environment.

Acknowledgements

Financial support for this work was provided by the Engineering and Physical Sciences Research Council and International Fire Investigators and Consultants Ltd.

References

[1] A. Bar Ilan, G. Rein, A. C. Fernandez Pello, J. L. Torero, and D. L. Urban. Forced forward smoldering experiments in microgravity. *Experimental Thermal and Fluid Science*, 28(7):743 – 751, 2004. doi: 10.1016/j.expthermflusci.2003.12.012. Third Mediterranean Combustion Symposium.

[2] A. Bar Ilan, G. Rein, D. C. Walther, A. C. Fernandez Pello, J. L. Torero, and D. L. Urban. The effect of buoyancy on opposed smoldering. *Combustion Science and Technology*, 176(12):2027–2055, 2004. doi: 10.1080/00102200490514822.

[3] J. L. Torero and A. C. Fernandez Pello. Forward smolder of polyurethane foam in a forced air flow. *Combustion and Flame*, 106(1-2):89–109, 1996. doi: 10.1016/0010-2180(95)00245-6.

[4] D. C. Walther, R. A. Anthenien, and A. C. Fernandez Pello. Smolder ignition of polyurethane foam: effect of oxygen concentration. *Fire Safety Journal*, 34(4): 343–359, 2000. doi: 10.1016/S0379-7112(00)00007-2.

[5] M. K. Anderson, R. T. Sleight, and J. L. Torero. Downward smolder of polyurethane foam: ignition signatures. *Fire Safety Journal*, 35(2):131–147, 2000. doi: 10.1016/S0379-7112(00)00016-3.

[6] T. J. Ohlemiller. *SFPE Fire Protection Handbook*, chapter 2-10: Smouldering Combustion, pages 2–201–2–210. National Fire Protection Association, Quincy, MA 02269, 3rd edition, 2002.

[7] D. Drysdale. *An Introduction to Fire Dynamics*. John Wiley and Sons Ltd, Chichester, UK, 2nd edition, 1998.

[8] G. Rein. Smouldering combustion phenomena in science and technology. *International Review of Chemical Engineering*, 1:3–18, 2009. URL hdl.handle.net/1842/2678.

[9] J. L. Torero. *Buoyancy Effects on Smoldering of Polyurethane Foam*. PhD thesis, University of California, Berkeley, 1992. URL www.era.lib.ed.ac.uk/handle/1842/2134.

[10] T. J. Ohlemiller. Modeling of smoldering combustion propagation. *Progress in Energy and Combustion Science*, 11(4):277–310, 1985. doi: 10.1016/0360-1285(85)90004-8.

[11] U. Krause and M. Schmidt. Propagation of smouldering in dust deposits caused by glowing nests or embedded hot bodies. *Journal of Loss Prevention in the Process Industries*, 13(3-5):319 – 326, 2000. doi: 10.1016/S0950-4230(99)00031-5.

[12] U. Krause and M. Schmidt. The influence of initial conditions on the propagation of smouldering fires in dust accumulations. *Journal of Loss Prevention in the Process Industries*, 14(6):527 – 532, 2001. doi: 10.1016/S0950-4230(01)00039-0.

[13] M. Schmidt, C. Lohrer, and U. Krause. Self-ignition of dust at reduced volume

fractions of ambient oxygen. *Journal of Loss Prevention in the Process Industries*, 16 (2):141 – 147, 2003. doi: 10.1016/S0950-4230(02)00095-5.

[14] B. Schartel, M. Bartholmai, and U. Knoll. Some comments on the use of cone calorimeter data. *Polymer Degradation and Stability*, 88(3):540–547, 2005. doi: 10.1016/j.polymdegradstab.2004.12.016.

[15] B. Schartel and T. R. Hull. Development of fire-retarded materialsinterpretation of cone calorimeter data. *Fire and Materials*, 31:327–354, 2007. doi: 10.1002/fam.949.

[16] S. J. Ritchie, K. D. Steckler, A. Hamins, T. G. Cleary, J. C. Yang, and T. Kashiwagi. The effect of sample size on the heat release rate of charring materials. *Fire Safety Science 5*, pages 177–188, 1997. doi: 10.3801/IAFSS.FSS.5-177.

[17] O. M. Putzeys, A. C. Fernandez Pello, G. Rein, and D. L. Urban. The Piloted Transition to Flaming in Smoldering Fire Retarded and Non-Fire Retarded Polyurethane Foam. *Fire and Materials*, 32:485–499, 2008. doi: 10.1002/fam.981.

[18] O. Putzeys, A. Bar Ilan, G. Rein, A. C. Fernandez Pello, and D. L. Urban. The role of secondary char oxidation in the transition from smoldering to flaming. *Proceedings of the Combustion Institute*, 31(2):2669 – 2676, 2007. doi: 10.1016/j.proci.2006.08.006.

[19] M. T. Gratkowski, N. A. Dembsey, and C. L. Beyler. Radiant smoldering ignition of plywood. *Fire Safety Journal*, 41(6):427 – 443, 2006. doi: 10.1016/j.firesaf.2006.03.006.

[20] L. Bustamante Valencia, T. Rogaume, E. Guillaume, G. Rein, and J. L. Torero. Analysis of principal gas products during combustion of polyether polyurethane foam at different irradiance levels. *Fire Safety Journal*, 44(7):933–940, 2009. doi: 10.1016/j.firesaf.2009.05.003.

[21] J. L. Torero. *SFPE Fire Protection Handbook*, chapter 11, Flaming Ignition of Solid Fuels, pages 2–260–2–277. National Fire Protection Association, Quincy, MA 02269, 4th edition, 2008.

[22] K. N. Palmer. Smouldering combustion in dusts and firbous materials. *Combustion and Flame*, 1:129–154, 1957.

3

Ignition of combustible fuel beds by hot particles: an experimental and theoretical study

Summary

The process of spotting occurs in wildland fires when fire-lofted embers or hot particles land downwind, leading to ignition of new, discrete fires. This common mechanism of wildland fire propagation can result in rapid spread of the fire, potentially causing property damage and increased risk to life safety of both firefighters and civilians. Despite the increasing frequency of, and losses due to wildland fires, there has been relatively little research on ignition of fuel beds by embers and hot particles. In this work, an experimental and theoretical study of ignition of homogeneous cellulose fuel beds by hot metal particles is undertaken. This type of well-characterized laboratory fuel provides a more controllable fuel bed than natural fuels, and the use of hot metal particles simplifies interpretation of the experiments by reducing uncertainty due to unknown effects of the ember combustion reaction. Spherical steel particles with diameters in the range 0.8 to 19.1 mm heated to temperatures between 500 and 1300°C are used in the experiments. A relationship between the size of the particle and temperature required for flaming or smouldering ignition is found. These results are used to assess a simplified analysis based on hot-spot ignition theory to determine the particle size–temperature relationship required for ignition of a cellulose fuel bed.

Nomenclature

Letters

a	surface area
A	pre-exponential factor
b	volumetric heat capacity ratio
c	specific heat capacity
C_1	curve fitting constant
C_2	curve fitting constant
E	activation energy
ΔH	heat of combustion
k	thermal conductivity
n	coordinate system parameter
r	particle radius
R	universal gas constant
t	time
T	temperature
V	volume
x	distance

Greek symbols

β	dimensionless inverse temperature
δ	Frank-Kamenetskii hot spot parameter
θ	dimensionless temperature
ρ	density
η	dimensionless distance
τ	dimensionless time

Subscripts

p	particle
0	initial

3.1 Introduction

Firebrand spotting is a major mechanism for spread of wildland and wildland urban interface (WUI) fires under dry, hot, and windy conditions that produce the most devastating fires. Spotting leads to more rapid fire spread than flame front propagation because embers generated by burning vegetation or structures are lofted by fire plumes and transported downwind to ignite secondary fires or structures remote from the fire front. Similarly, many structures destroyed during WUI fires are not ignited by direct flame impingement, but rather by embers penetrating vents/eaves or direct ignition of roof construction and other 'soft' targets. Following the devastating 1994 Sydney wildland fires, a statistical study determined that 75% of houses were ignited by firebrands, while 25% were ignited by firebrands and flame radiation [1]. Molten/burning particles can sometimes be generated by high-voltage powerline conductors clashing in high winds. When these hot particles (typically copper or aluminum) reach the ground they may ignite fires in surrounding vegetation. Furthermore, civilians and firefighters alike can become trapped between spot fires with no escape route.

The conditions under which embers and heated particles can ignite a spot fire have not been widely investigated. Only a few studies have examined the critical

conditions that can lead to fire initiation after the landing of a firebrand or particle on a particular fuel bed. These studies are primarily experimental in nature [2–8], and no comprehensive theoretical studies have yet been conducted to analyse the problem or develop generalized predictive tools. Consequently, previous models of wildland fire propagation [9–11] have limited capabilities to predict the initiation of spot fires.

The work presented here is a combined experimental and theoretical study of fuel bed ignition by hot particles. Inert steel spheres are used to approximate firebrands/heated particles to remove uncertainty introduced with burning embers (ember temperature, char layer thickness, combustion characteristics, thermal properties, etc.). Similarly, powdered cellulose is used as the target fuel because it is homogeneous in composition and has known properties. Finally, a simplified analytical treatment based on the classical hot spot theory is reviewed and its predictive capabilities are assessed.

3.2 Background

3.2.1 Firebrand/particle generation and transport

The first step of spot fires is the generation of the firebrand. Firebrand generation is the process through which natural fuels broken into smaller burning pieces during a fire and lofted by a buoyant fire-induced plume or powerlines interact generating molten metal particles. Yoshioka et al. [12] and Manzello et al. [7, 13] have characterized the number and size distribution of brands generated by different fuels. Firebrands generated by a single Douglas Fir can range in size from 200 mm to 10 mm in diameter.

The trajectories and burning rates of firebrands or heated particles lofted by fires have been studied more extensively [14–23]. Collectively, the studies suggest that small embers or particles are easily lofted and can travel long distances. However, they may burn out or have a low temperature at landing, and are therefore less likely to cause ignition. In comparison, large embers or particles may have long burn times, but they are more difficult to transport and therefore do not travel far from the fire front. Embers or particles of intermediate size have a relatively long burn time and can be lofted considerable distances.

3.2.2 Spot fire formation: ignition (or non-ignition) of fuel beds after particle landing

The aspect of spot fire formation that is least understood is what happens after a firebrand or heated particle lands on a target fuel bed. Of greatest interest is whether or not ignition (smouldering ignition, flaming ignition, or smouldering followed by transition to flaming) occurs. This complex process depends on several factors, including the size and state of the brand or particle (temperature, smouldering/glowing, flaming), the characteristics of the fuel bed on which it lands (temperature, density, porosity, moisture content), and environmental conditions (temperature, humidity, wind velocity). Ignition of fuel beds by firebrands and heated surfaces has been studied primarily experimentally, in particular by workers at NIST [4–7]. Studies on ignition by metal particles have been reported by Rowntree and Stokes [2, 3].

Using single glowing embers of Douglas Fir (5 or 10 mm diameter, 51 and 76 mm length respectively) under air flow of 0.5 or 1 $m \cdot s^{-1}$, Manzello et al. [7] found that smouldering ignition would occur in shredded paper but no ignition would occur in pine needles or hardwoods. For flaming embers under the same conditions, flaming ignition would occur in all fuels except hardwood mulch at 11% moisture content. Using four glowing embers, smouldering ignition could be achieved in dry hardwood mulch. However, four flaming embers were not capable of igniting hardwood at 11% moisture content. Similar results are found using disc-shaped embers [4, 5] where flaming ignition occurred only when flaming embers are dropped. It was also observed that multiple flaming embers resulted in flaming ignition where single embers would cause no ignition. In general, smouldering particles are not capable of igniting fuels, whereas flaming embers will likely result in ignition of thin, dry fuels.

Electrically heated hot-spots were used by Caine et al. [8] to study the ignition of four porous fuels. As hot-spot size was increased, the power required to ignite the material was observed to increase which is believed to be explained by the existence of a critical temperature for ignition. No obvious relationship between the hot-spot diameter and the temperature required for ignition in any of the four fuels was found.

These experimental studies differ from the experiments reported in this paper because burning embers rather than inert particles or particles artificially maintained

at elevated temperatures were used. Therefore, ignition is influenced both by the combustion reaction and heat transfer between the particle and the fuel bed.

A few theoretical studies related to ignition of fuel beds have been conducted. It has been suggested [2, 3] that the energy content (Joules) of a particle can be used as an ignition criterion, analogous to the minimum ignition energy concept for gases. Essentially, if the energy content of a particle is greater than a particular threshold, then ignition occurs. However, Babrauskas [24] has critiqued this approach and justifiably concludes that it is insufficient because particles of different size with the same energy do not necessarily result in ignition. He also notes that laboratory studies to date do not allow the determination of which thermal properties control incendivity. Babrauskas concludes that the 'hot spot' ignition theory will allow reasonable prediction of particle size–temperature relationships for ignition. Hot spot theory was originally developed in the 1960s and 1970s [25–29] and applied later [30–32] to ignition of natural fuels. More recently, detailed numerical models have been applied to simulate spot fire initiation [33–35].

3.3 Experiment description

The experimental apparatus used in this work is shown in Fig. 3.1. Spherical steel particles of diameter 0.8, 1.6, 2.4, 3.2, 4.4, 6.2, 9.5, 12.7, 15.9, and 19.1 mm heated to temperatures between 500 and 1300°C were used. The fuel bed is mounted in the bottom of a wind tunnel with the sample surface flush with bottom of the tunnel. The wind tunnel is 550 mm in length with a 130×80 mm cross section. The sample holder is 150 mm long, 100 mm wide and 50 mm deep and its leading edge is 150 mm from the inlet of the tunnel. The target fuel was approximately 130 g of dry, fine powdered α-cellulose placed, uncompacted, in the sample holder. In order to ensure uniform properties throughout, the mass of cellulose used for each experiment was weighed before testing to ensure the bulk porosity remained constant at 200 $\mathrm{kg \cdot m^{-3}}$. Compressed air is introduced to the wind tunnel at a velocity of 0.5 $\mathrm{m \cdot s^{-1}}$. Sheathed K-type thermocouples are inserted into the fuel sample at locations shown in Fig. 3.1a. Glass panels allow for observation and video recording of the test. Only solid phase

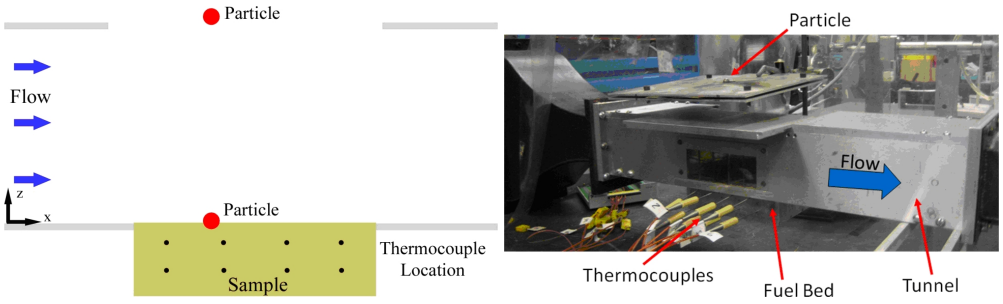

(a) (b)

Figure 3.1. (a) Simplified schematic and (b) photograph of experimental apparatus.

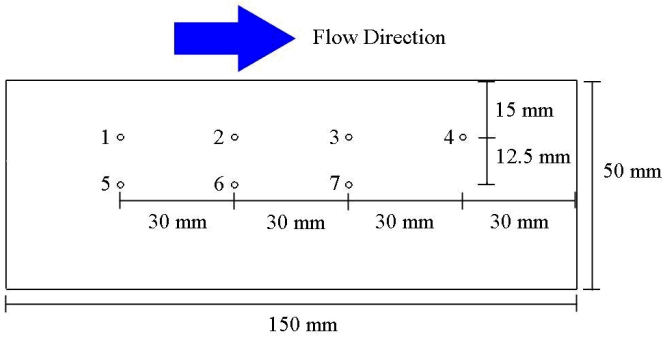

Figure 3.2. Fuel bed dimensions and thermocouple locations.

temperatures are measured in this set-up. There is a removable section in the roof of the tunnel to allow hot particles to be dropped on the sample.

During an experiment, a particle of the desired size is heated with a premixed propane flame. Once the particle has reached the required temperature, as measured by a thermocouple inserted into the particle, it is dropped onto the sample surface from a height of approximately 20 mm. The particle is dropped approximately 35 mm downstream from the leading edge of the sample. Fuel bed temperature is recorded along the centerline at seven locations, as shown in Fig. 3.2.

The depth to which the hot spheres penetrated the fuel bed was not controlled and was found to vary depending on the size of the sphere. Large spheres were more likely to be partially embedded while smaller particles could be completely embedded. The depth of the particle below the surface is likely to have an effect on ignition, but this was not studied in this work.

3.4 Experimental results

Experiments are conducted to identify the effect of particle size and temperature on ignition of powdered cellulose. Depending on the particle characteristics, both flaming and smouldering ignition were observed. In flaming ignition, a flame kernel initiated around the hot particle; if the particle was hot enough, this flame would propagate across the free surface of the sample and eventually extinguish. In-depth smouldering would then be seen to continue for several hours.

In the case of smouldering ignition, a smoulder front would be established around the hot particle. This front would then propagate laterally as well as in depth. In all cases where smouldering was ignited, the sample was seen to burn to completion. Transition from smouldering to flaming was not observed.

3.4.1 Temperature profiles

Figure 3.3 shows the temperature profile for a sample in which flaming occurred initially across the surface of the sample followed by in depth smouldering. Peak fuel bed temperatures are in the range 465–550°C. Temperatures in depth were higher than those closer to the free surface, due to heat losses. The temperature peak in the solid phase advances both laterally and in depth from the point where the hot particle was dropped.

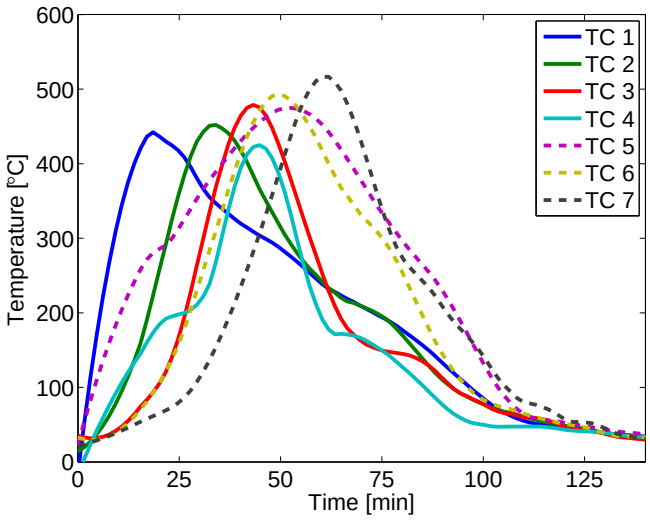

Figure 3.3. Temperature profiles in the fuel bed for a sample in which flaming was observed. Thermocouple locations refer to those in Fig. 2.

3.4.2 Smoulder spread rate

The smoulder spread rate of the solid phase reactions was found to be a function of depth and distance from the hot particle. Spread rate was calculated by finding the times at which each thermocouple reached 300°C and dividing the distance between the thermocouples by the time between adjacent thermocouples reaching this temperature.

For the example above, at a depth of 15 mm below the free surface, spread rates were 2.0, 3.1 and 5.3 mm·min^{-1} at positions between 30 and 60, 60 and 90, and 90 and 120 mm from the leading edge, respectively. This suggests that as the size of the reaction front grows, the spread rate increases. However, at a depth of 17.5 mm below the free surface, this effect is much reduced and the spread rates are 2.9 and 2.7 mm·min^{-1} between thermocouple locations 30 and 60 mm and 60 and 90 mm from the leading edge respectively. These spread rates are in agreement with others reported in the literature [36].

3.4.3 Propensity for ignition

Figure 3.4 shows the ignition propensity as a function of particle size and temperature. Triangles represent direct flaming ignition, circles are smouldering ignition, and crosses represent no ignition. The data clearly show a demarcation between no ignition, smouldering ignition, and flaming ignition. It can be seen that for both flaming and smouldering ignition, smaller particles require higher temperatures than larger particles. The trends in Fig. 3.4 are qualitatively consistent with the data of Stokes and Rowntree [2, 3]. Due to the experimental method for delivering the hot particles, it was not always possible to ensure the particles were exactly the same temperature upon landing on the fuel and obtained the same level of submergence in the cellulose. This results in some overlap between the ignition types in some cases.

Figure 3.4 contains two lines that demarcate the regions of flaming and smouldering ignition. These lines are of the form

$$2r_p = C_1 T_p \sqrt{\exp\left(\frac{C_2}{T_p}\right)}, \tag{3.1}$$

where C_1 and C_2 were selected to fit the data. The functional form of Eq. 3.1 is based on

the hot spot theory discussed in Section 3.5.1 (see Eq. 3.21).

Table 3.1. Values of constants for demarcation of ignition regimes.

	C_1 [m/K]	C_2 [K]
Smouldering	0.0004	4862
Flaming	0.0011	4262

For the range of particles tested, the minimum particle temperature at which smouldering could be initiated was 550°C, and the minimum temperature at which flaming ignition occurred was 650°C. In both cases, this was for a particle diameter of 19.1 mm. Flaming could only be observed for particles larger than 2.4 mm heated to 1200°C. Flaming was not observed with particles smaller than 9.5 mm and with the particle temperature range studied here.

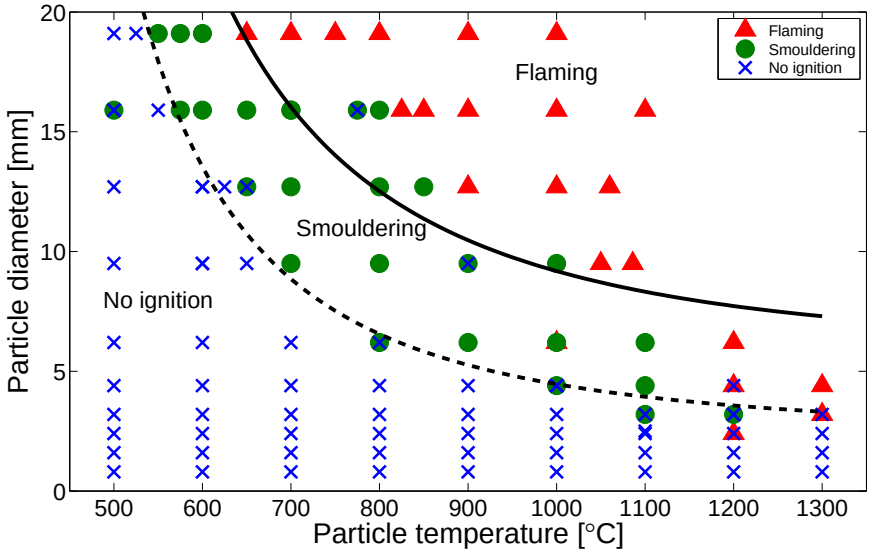

Figure 3.4. Ignition propensity of dry cellulose using heated steel spheres.

Figure 3.5 shows energy plotted against particle size where energy is calculated using the specific enthalpy for a given particle temperature and mass of the sphere. It can be seen that a correlation between particle energy and ignition is not sufficient to explain the observed results. For example, an energy of 200 J will result in flaming ignition for particles 9.5 and 12.7 mm, but only smouldering ignition for particles of 15.9 and 19.1 mm. This suggests that the ignition process is complex and governed not only by the energy of an ember but also the temperature and size, in agreement with the comments by Babrauskas [24].

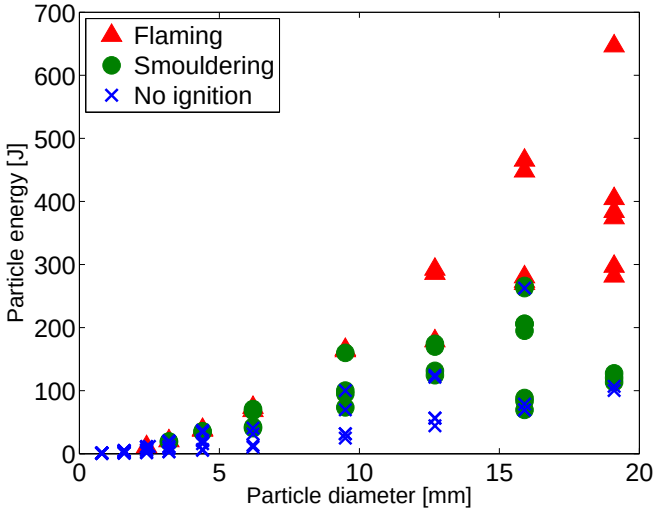

Figure 3.5. Particle energy versus particle size. Showing flaming ignition (triangles), smouldering ignition (circles) and no ignition (crosses).

3.5 Simplified theoretical analysis

3.5.1 Hot spot theory

It has been suggested that hot spot theory [24–28] can be used to model the ignition of natural fuels by heated particles. In a sequence of three papers, Jones [30–32] applied hot spot theory to simulate the ignition of forest litter by copper particles. In Jones [32], the theory of Gol'dshleger et al. [25] is applied. This same theory [25] has been recommended by Bowes [37] for its compromise between accuracy and tractability, and has also been applied by Babrauskas [24] to model the barley grass ignition experiments of Rowntree and Stokes [3] involving heated particles. Since the hot spot theory of Gol'dshleger et al. [25] seems to be a logical starting point for modelling the present experiments, it is presented briefly below and then applied to the current experiments.

The governing equations for a non-reactive hot spot particle (subscript p) completely embedded in an infinite target fuel are as follows. For $0 < x < r$:

$$\rho_p c_p \frac{dT_p}{dt} = \frac{a_p}{V_p} k \, \nabla T|_{x=r^+} , \tag{3.2}$$

and for $r < x < \infty$:

$$\rho c \frac{\partial T}{\partial t} = \nabla \cdot k \nabla T + \rho A \Delta H \exp\left(-\frac{E}{RT}\right). \tag{3.3}$$

In writing Eq. 3.2, the energy equation for the particle, it has been assumed that $k_p \gg k$ (i.e., the particle temperature is uniform due to its high thermal conductivity) and that the particle is in good thermal contact with the surrounding fuel bed so that the rate of heat transfer from the particle is $a_p k \nabla T$ where a_p is the particle surface area.

The initial conditions for the particle and the target fuel are, for $0 < x < r$:

$$T_p\big|_{t=0} = T_{p0}, \tag{3.4}$$

and for $r < x < \infty$:

$$T|_{t=0} = T_0. \tag{3.5}$$

The boundary conditions on Eq. 3.3 are

$$T|_{x\to\infty} = T_0 \tag{3.6}$$

and

$$T|_{x=r^+} = T_p. \tag{3.7}$$

Equations 3.2–3.7 are non-dimensionalized by introducing dimensionless temperature, distance, and time variables:

$$\theta = \frac{E}{RT_{p0}^2}\left(T - T_{p0}\right), \tag{3.8}$$

$$\xi = \frac{x}{r}, \tag{3.9}$$

$$\tau = \frac{t}{\frac{cRT_{p0}^2}{AE\Delta H \exp\left(-\frac{E}{RT_{p0}}\right)}}. \tag{3.10}$$

Three additional dimensionless parameters (δ, the Frank-Kamenetskii hot spot parameter; b, the volumetric heat capacity ratio; and β, the dimensionless inverse particle temperature) are defined as follows:

$$\delta = r\sqrt{\frac{\rho A \Delta H}{k}\frac{E}{RT_{p0}^2}\exp\left(-\frac{E}{RT_{p0}}\right)}, \tag{3.11}$$

$$b = \frac{\rho c}{\rho_p c_p}, \tag{3.12}$$

$$\beta = \frac{RT_{p0}}{E}. \tag{3.13}$$

The one-dimensional constant-property governing equations (i.e., the 1D dimensionless counterparts to Eqs 3.2 and 3.3) for the particle and target fuel bed become

$$\frac{d\theta_p}{d\tau} = \frac{n+1}{\delta^2} b \left.\frac{\partial\theta}{\partial\xi}\right|_{\xi=1^+} \tag{3.14}$$

and

$$\frac{\partial\theta}{\partial\tau} = \frac{1}{\delta^2}\left(\frac{\partial^2\theta}{\partial^2\xi^2} + \frac{n}{\xi}\frac{\partial\theta}{\partial\xi}\right) + \exp\left(\frac{\theta}{1+\beta\theta}\right). \tag{3.15}$$

where n is the coordinate system parameter ($n = 0$ for Cartesian coordinates, $n = 1$ for cylindrical coordinates, and $n = 2$ for spherical coordinates).

The initial conditions are, for $0 < \xi < 1$:

$$\theta_p\big|_{\tau=0} = \theta_{p0} = 0, \tag{3.16}$$

and for $1 < \xi < \infty$:

$$\theta\big|_{\tau=0} = \theta_0 = -\theta_\Delta. \tag{3.17}$$

The boundary conditions on Eq. 3.15 are:

$$\theta\big|_{\xi=1^+} = \theta_p, \tag{3.18}$$

$$\theta\big|_{\xi\to\infty} = \theta_0. \tag{3.19}$$

Equations 3.14–3.19 cannot be solved exactly, and numerical solution is required. Of primary interest is the value of the δ at which thermal runaway (ignition) occurs ($\delta_c r$). It should be noted that Eqs 3.2–3.7 do not include heat losses from the system as a whole since it is assumed to be infinite. In a mathematical sense, thermal runaway may occur at long time scales for certain parameter values even without a hot spot. However, here we consider ignition to be thermal runaway that occurs at a time scale that is much shorter than that associated with the adiabatic induction period. Gol'dshleger et al. [25] conducted numerical simulations to determine the value of $\delta_c r$ and found that the following curve-fit matched their numerical results within 10%:

$$\delta_{cr} \approx 0.4\sqrt{b^2 + 0.25n(n+1)(b+0.1b^3)}(2.25(n-1) - \theta_0)^2(1 - 0.5\beta\theta_0). \tag{3.20}$$

Once δ_{cr} is calculated from Eq. 3.20, the critical hot spot radius r_{cr} (i.e., the minimum particle radius for ignition) can be calculated from the definition of δ (Eq. 3.11) as

$$r_{cr} = \delta_{cr}\sqrt{\frac{k}{\rho A \Delta H}\frac{RT_{p0}^2}{E}\exp\left(\frac{E}{RT_{p0}}\right)}. \tag{3.21}$$

3.5.2 Application to present experiments

Thermophysical properties of cellulose and the particle are necessary to calculate the critical radius size for ignition. The thermophysical properties used in this analysis are given in Table 3.2.

Figure 3.6 compares the critical particle diameter for ignition calculated via Eq. 3.21 with experimental data.

3.5.3 Assessment of hot spot theory predictive capabilities for present experiment

It can be seen from Fig. 3.6 that the hot spot theory presented above, when provided with the input parameters given in Table 3.2, qualitatively reproduces the experimental data but is not quantitatively accurate. However, the hot spot theory is conservative for particles smaller than ~2.4 mm in diameter that have temperatures greater than 850°C because it suggests that ignition occurs for some size/temperature combinations, but

Table 3.2. Thermophysical properties of target fuel bed (cellulose) and heated particle (steel)

Parameter	Value	Units	Reference	Description
k	0.1	$W \cdot m^{-1} \cdot K^{-1}$	Estimated	Thermal conductivity (target)
ρ	200	$kg \cdot m^{-3}$	Measured	Density (target)
c	2.0	$kJ \cdot kg^{-1} \cdot K^{-1}$	Estimated	Specific heat capacity (target)
ρ_p	7833	$kg \cdot m^{-3}$	[38]	Density (particle)
c_p	465	$kJ \cdot kg^{-1} \cdot K^{-1}$	[38]	Specific heat capacity (particle)
A	1×10^{17} [a]	s^{-1}	[39]	Pre-exponential factor
E	222 [a]	$kJ \cdot mol^{-1}$	[39]	Activation energy
H	10 [b]	$MJ \cdot kg^{-1}$	[40]	Heat of combustion
T_0	300	K	Measured	Initial temperature

[a] Average from 8 TGA experiments at 40°C/min heating rate
[b] The heat of complete combustion of cellulose is approximately 15 $MJ \cdot kg^{-1}$ [40] but since CO is expected to form in considerable amounts, the heat of combustion is reduced by 1/3 to 10 $MJ \cdot kg^{-1}$

the experiments show that ignition does not occur.

Some aspects of the present experiments not included in the hot spot theory include:

1. The mechanism of flaming ignition may be somewhat different from that described by hot spot theory (thermal runaway inside the condensed phase). It is possible that a heated particle sitting on top of the cellulose bed acts as a localized heat source, causing the powdered cellulose to pyrolyse at a rate that is sufficient to produce a flammable mixture in the vicinity of the heated particle, which in turn acts as an ignition pilot. Gas-phase ignition (outside of the fuel bed) may occur if the residence time of the combustible gas mixture flowing by the heated particle is comparable to the ignition delay time of that mixture at the particle temperature. Ignition would occur in the gas phase, and a diffusion flame then becomes anchored to the surface.

2. Hot spot theory assumes the particle is completely embedded in an infinite medium, but in the experiments the heated particles sit on top of, or are partially embedded in the fuel bed.

3. Surface heat losses are not accounted for. The particle loses heat by convection

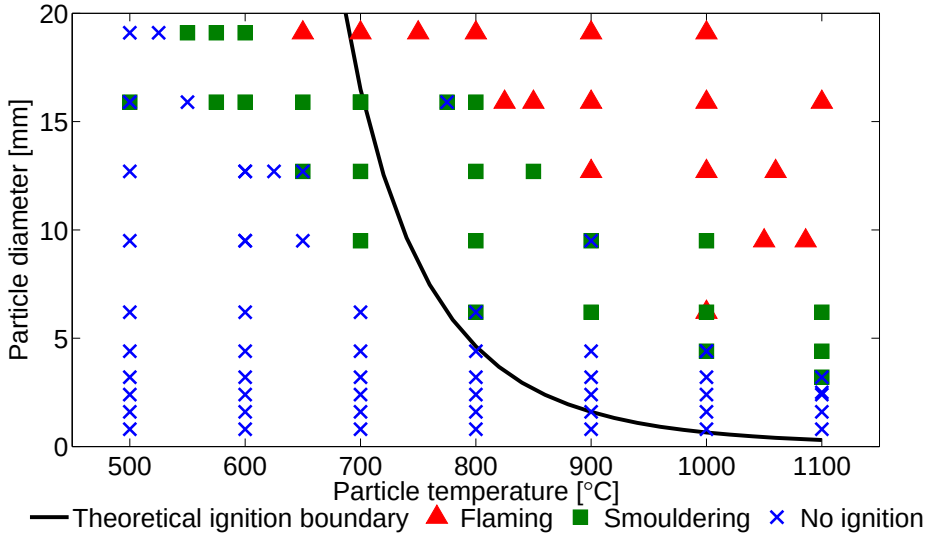

Figure 3.6. Comparison of experimental data with hot spot theory (Eq. 3.21) using the parameters in 3.2.

and radiation to the ambient and this effect is not included in the simplified analysis.

4. Oxygen availability is not accounted for. Equations 3.3 and 3.15 have an exothermic source term on the right hand side. Thus, these equations inherently assume that the pore space contains sufficient oxygen to drive an exothermic oxidative reaction. However, if oxygen inside the pore space is completely consumed, then thermal decomposition of cellulose is likely to be endothermic.

5. The above analysis assumes that consumption of reactants is negligible (zeroth order Arrhenius reaction), but reactant consumption may not be negligible.

6. The above analysis assumes that a single reaction occurs whereas in actuality multiple reactions may occur.

7. Hot spot theory does not account for any effects of volume change such as shrinkage, swelling, or compaction of the fuel bed by particles.

3.6 Concluding remarks

Ignition of cellulose fuel beds by hot spherical particles has been studied experimentally and a model of hot spot ignition presented.

- The results show as particle size is reduced, increased temperature is required for ignition. For a particle size of 2.4 mm, temperatures of 1200°C were required for flaming ignition and this was reduced to 650°C for particles of 19.1 mm.
- Ignition propensity is a function of both particle size and particle temperature.
- There is not a unique correlation between particle energy and ignition propensity.
- Hot spot ignition theory provides qualitative agreement with experimental results but is not quantitatively predictive for the present experiments.

Acknowledgements

Thanks go to the Royal Society of Edinburgh, International Fire Investigators and Consultants Ltd and Engineering and Physical Research Council (UK) for providing the financial assistance for the first author's (RH) work. Part of this work was supported by the University of California, Berkeley.

References

[1] G. C. Ramsey and N. A. McArthur. Building in the urban interface: Lessons from the january 1994 sydney bushfires. In *Bushfire '95*, Hobart, Tasmania, 1995.

[2] A. D. Stokes. Fire ignition by copper particles of controlled size. , *Journal of Electrical and Electronics Engineering, Australia*, 10:188–194, 1990.

[3] G. W. G. Rowntree and A. D. Stokes. Fire ignition by aluminum particles of controlled size. *Journal of Electrical and Electronics Engineering, Australia*, 14: 117–123, 1994.

[4] S. L. Manzello, T. G. Cleary, J. R. Shields, and J. C. Yang. On the ignition of fuel beds by firebrands. *Fire and Materials*, 30:77–87, 2006.

[5] S. L. Manzello, T. G. Cleary, J. R. Shields, and J. C. Yang. Ignition of mulch and grasses by firebrands in wildland urban interface fires. *International Journal of Wildland Fire*, 15(3):427–431, 2006. doi: 10.1071/WF06031.

[6] W. Pitts. Ignition of cellulosic fuels by heated and radiative surfaces. Technical Report 1481, NIST, 2007.

[7] S. L. Manzello, T. G. Cleary, J. R. Shields, A. Maranghides, W. Mell, and J. C. Yang. Experimental investigation of firebrands: Generation and ignition of fuel beds. *Fire Safety Journal*, 43(3):226 – 233, 2008. doi: 10.1016/j.firesaf.2006.06.010.

[8] P. Caine, S. J. Puttick, J. Brindley, A. C. McIntosh, and J. F. Griffiths. Ignition of bulk solid materials by a localised hotspot. In *Hazards XXI*, pages 1991–2000, 2009.

[9] M. A. Finney. FARSITE: Fire Area Simulator-model development and evaluation. Technical Report Research Paper RMRS-RP-4, Ogden, UT, US Department of Agriculture, Forest Service, Rocky Mountain Research Station, 1998.

[10] R. Linn, J. Resiner, J. J. Colman, and J. Winterkamp. Studying wildfire behavior using firetec. *International Journal of Wildland Fire*, 11:233–246, 2002.

[11] W. Mell, M. A. Jenkins, J. Gould, and C. Cheney. A physics-based approach to modeling grassland fires. *International Journal of Wildland Fire*, 16:1–22, 2007.

[12] H. Yoshioka, Y. Hayashi, H. Masuda, and T. Noguchi. Real-scale fire wind tunnel experiment on generation of firebrands from a house on fire. *Fire Science and Technology*, 23:142–150, 2004.

[13] S. L. Manzello, J. R. Shields, T. G. Cleary, A. Maranghides, W. E. Mell, J. C. Yang, Y. Hayashi, D. Nii, and T. Kurita. On the development and characterization of a firebrand generator. *Fire Safety Journal*, 43(4):258–268, 2008. doi: 10.1016/j.firesaf.2007.10.001.

[14] C. Sánchez Tarifa, P. Pérez del Notario, and F. García Moreno. On the flight paths and lifetimes of burning particles of wood. *Symposium (International) on Combustion*, 10(1):1021–1037, 1965.

[15] S. L. Lee and J. M. Hellman. Firebrand trajectory study using an empirical velocity-dependent burning law. *Combustion and Flame*, 15(3):265–274, 1970.

[16] F. A. Albini. Spot fire distance from burning trees: a predictive model. Technical Report GTR-INT-56, USDA Forest Service, 1979.

[17] F. A. Albini. Potential spotting distance from wind-driven surface fires. Technical Report Research Paper ZNT-309, USDA Forest Service, 1983.

[18] S. D. Tse and A. C. Fernandez-Pello. On the flight paths of metal particles and embers generated by power lines in high winds–a potential source of wildland fires. *Fire Safety Journal*, 30(4):333–356, 1998.

[19] J. P. Woycheese. Wooden disk combustion for spot fire spread. In *Interflam 2001*, pages 101–112, 2001.

[20] K. Himoto and T. Tanaka. Transport of disk-shaped firebrands in a turbulent boundary layer. *Fire Safety Science-Proceedings of the 8th International Symposium*, pages 433–444, 2005.

[21] R. A. Anthenien, S. D. Tse, and A. C. Fernandez-Pello. On the trajectories of embers initially elevated or lofted by small scale ground fire plumes in high winds. *Fire Safety Journal*, 41(5):349–363, 2006.

[22] N. Sardoy, J.-L. Consalvi, B. Porterie, and A. C. Fernandez-Pello. Modeling transport and combustion of firebrands from burning trees. *Combustion and Flame*, 150(3):151–169, 2007.

[23] E. Koo, P. Pagni, and R. Linn. Using firetec to describe firebrand behavior in wildfires. In *Fire and Materials 2007*, 2007.

[24] V. Babrauskas. *Ignition Handbook: Principles and Applications to Fire Safety Engineering, Fire Investigation, Risk Management, and Forensic Science*, chapter 14: The A-Z, page 843. Fire Science Publishers, 2003.

[25] U. I. Gol'dshleger, K. V. Pribytkova, and V. V. Barzykin. Ignition of a condensed explosive by a hot object of finite dimensions. *Fizika Goreniya I Vzryva*, 9:119–123, 1973.

[26] J. Zinn. Initiation of explosions by hot spots. *Journal of Chemical Physics*, 36, 1949 (1962).

[27] T. Boddington. The growth and decay of hot spots and the relation between structure and stability. *Symposium (International) on Combustion*, 9(1):287–293, 1963.

[28] M. H. Friedman. A correlation of impact sensitivities by means of the hot spot model. *Symposium (International) on Combustion*, 9(1):294–302, 1963.

[29] P. H. Thomas. A comparison of some hot spot theories. *Combustion and Flame*, 9(4): 369–372, 1965.

[30] J. C. Jones. Predictive calculations of the effect of an accidental heat source on a bed of forest litter. *Journal of Fire Sciences*, 11:80–086, 1993.

[31] J. C. Jones. Further calculations concerning the accidental supply of heat to a bed of forest material. *Journal of Fire Sciences*, 12:502–505, 1994.

[32] J. C. Jones. Improved calculations concerning the ignition of forest litter by hot particle ingress. *Journal of Fire Sciences*, 13:350–356, 1995.

[33] A. I. Zvyagilskaya and A. N. Subbotin. Influence of moisture content and heat and mass exchange with the surrounding medium on the critical conditions of initiation of surface fire. *Combustion, Explosions, and Shock Waves*, 32:558–564, 1996.

[34] A. M. Grishin, A. A. Dolgov, V. P. Zima, D. A. Kryuchkov, V. V. Reino, A. N. Subbottan, and R. S. Tsvyk. Ignition of a layer of combustible forest materials. *Combustion, Explosions, and Shock Waves*, 34:613–620, 1998.

[35] C. Lautenberger and A. C. Fernandez-Pello. Modeling ignition of combustible fuel beds by embers and heated particles. In *Forest Fires 2008*, 2008.

[36] G. Rein. Smouldering combustion phenomena in science and technology. *International Review of Chemical Engineering*, 1:3–18, 2009. URL hdl.handle.net/1842/2678.

[37] P. C. Bowes. *Self-heating: evaluating and controling the hazards*. Her Majesty's Stationery Office, London, 1st edition, 1984.

[38] P. DiNenno, editor. *The SFPE Handbook of Fire Protection Engineering*, chapter Appendix B, Table B-6, pages A30–A31. National Fire Protection Association, Quincy, MA, 3rd edition, 2002.

[39] M. Grønli, M. J. Antal, and G. Varhegyi. A round-robin study of cellulose pyrolysis kinetics by thermogravimetry. *Industrial and Engineering Chemistry Research*, 38(6):2238–2244, 1999.

[40] Y. Chen, A. Frendi, S. S. Tewari, and M. Sibulkin. Combustion properties of pure and fire-retarded cellulose. *Combustion and Flame*, 84(1-2):121–140, 1991.

4

Ignition and suppression of small-scale smouldering coal fires

Summary

The ignition, burning and suppression of subsurface coal fires have been studied using laboratory-scale experiments. Coal particles in the range 7–45 mm were studied in a $100 \times 100 \times 100$ mm^3 smouldering box. Time to ignition was seen to be dependent on particle size with a minimum time to ignition of 140 min for particles of 30 mm. Maximum smouldering temperatures were found to be in the range 720–930°C and mass loss at the time of suppression around 40%. These were found to be independent of particle size for particles greater than 20 mm. The spread rate was found to be on the order of 0.7 mm·min^{-1}, typical of smouldering fires. The effectiveness of a pipe, shower and spray for delivery of a suppression agent was assessed. The pipe and shower were found to result in high levels of run-off requiring on average 3 and 0.75 l·kg^{-1}of water to extinguish fire. The spray used approximately 1.25 l·kg^{-1}. The effect of particle size on the water required for extinguishing using a spray was found to be weak, reducing from 1.4 l·kg^{-1}for particles of diameter 7 mm to 0.9 l·kg^{-1}for particles of 45 mm diameter.

4.1 Introduction

Subsurface fires propagate by smouldering combustion which is defined as the slow, low-temperature flameless form of combustion sustained by the heat evolved when oxygen directly attacks the surface of a condensed-phase fuel [1]. The characteristics of smouldering mean that it is hard to detect, may exist for extended periods of time and is difficult to extinguish. In the context of this work, we refer to suppression as all the processes aiming to reach the extinction of the fire, i.e. the chemical processes of combustion have been permanently stopped.

This work seeks to provide an insight into the ignition, spread and suppression of subsurface smouldering coal fires using small-scale experiments. The large size and complex nature of subsurface coal fires mean that they are not simple to study in the field. Therefore, in order to understand the mechanisms which govern them, it is necessary to conduct studies in the laboratory where controlled conditions result in repeatable smouldering fronts as well as allowing detailed measurements.

Prior to presenting the experimental results, a review of the smouldering process and the current methods employed to extinguish these fires is given.

4.2 Structure of the smouldering front

Once ignited, smouldering propagates at a slow speed on the order of mm per hour and is governed by the rate at which oxygen can diffuse to the reaction front [1]. Thermal properties of the fuel, moisture content, organic fraction, and flow permeability are also important parameters dictating the ignition, spread and extinction of subsurface fires.

Smouldering fires can burn in shallow or deep fronts [2]. Shallow fronts burn near the free surface, which allows ample supply of oxygen to the reaction zone but results in higher heat losses. Deep subsurface fires burn many metres below the ground and therefore have a limited supply of oxygen but are more insulated from heat losses [3]. The structure of a smouldering front as detailed by Ohlemiller [1] and Rein [4] is outlined below.

1. Preheating of the undisturbed fuel: heat from the reacting front is transported and preheats the fuel up to temperatures where water evaporation takes place.

This front does not emit gases in any significant quantity.

2. Evaporation: this endothermic reaction occurs at temperatures below 100°C, emitting water vapour. In this front the mass loss depends on the moisture content of the fuel.

3. Burning region: this front is where the pyrolysis and oxidation reactions take place and net quantities of heat are released. The pyrolysis reaction absorbs heat and converts the fuel into volatile gases (mainly methane, light and polyaromatic hydrocarbons and water vapour), leaving behind a solid, carbonaceous char. Pyrolysis generally starts at temperatures above 200–250°C. Subsequent heating above this temperature increases the rate of the pyrolysis reactions. The oxidation reaction involves the exothermic reaction of the solid fuel and char left by the pyrolysis front. The peak temperature is found in this region and this is where most of the fuel mass is lost. This front may overlap with the pyrolysis front depending on the propagation mode and oxygen availability. The oxidation reaction typically occurs at temperatures over 300°C and is the main source of CO and CO_2 emissions. More CO_2 is formed where the oxygen supply is large (e.g. closer to the free surface) and CO where it is small (e.g. deeper into the fuel layers).

4. Char and ash region: this is where the smouldering has ceased and the remaining matter cools down to ambient temperature. The ash left is the mineral content present in the original fuel and remaining char is the result of incomplete burning.

4.3 Suppression of smouldering coal fires

Kim [5] and Colaizzi [6] show that extinguishing is a costly, resource intensive procedure which often fails to produce the desired result. It is estimated that subsurface coal fires in the United States affect over 400 ha, and estimated reclamation costs exceed $42 million [5]. Common mechanisms of suppression include sealing of the affected area to prevent oxygen ingress and injection of an ambient temperature inert gas to displace oxygen. However, these methods require long timescales and large quantities

of materials. Additional methods such as injection of a cryogenic liquid have been investigated but remain problematic and costly [5].

Figure 4.1 shows an artistic representation of a subsurface coal fire and typical damage to the environment and infrastructure. Hypothetical growth of the fire with time is indicated. The low porosity of the coal means that permeability to flow is low and therefore oxygen transfer to the reaction zone is slow. The presence of mine shaft networks allows the supply of oxygen to deep layers. Fires in coal mines and seams are generally ignited in locations where coal is present as relatively small particles, the nature of which results in a high surface area on which the smoulder reaction can occur.

There are three main mechanisms that could lead to the extinction of a smouldering fire in situ: cooling, smothering and burn-out. Burn-out does not involve a suppresskion agent and is greatly accelerated by excavation of the fuel. This is only viable for shallow fires, and will not be discussed here.

The first two mechanisms are based on the physical and chemical process governing smouldering fires. For a smouldering reaction to propagate, a feedback mechanism must be established where the heat released from the reacting fuel is sufficient to overcome the heat losses and to preheat the surrounding fuel. If the heat balance is altered by increasing heat loss to the surroundings, the rate of the pyrolysis reaction will decrease and the smouldering combustion could be quenched; this mechanism is exploited in suppression by cooling. In forced cooling, the coal temperature is reduced below a critical re-ignition temperature by injecting a suppression agent below the surface and allowing it to propagate through the ground to the seat of the fire. Given the large size of coal seams, this method requires large quantities of the suppression agent and it is challenging to ensure that sufficient quantities reach the reaction zone as the fluid disperses through the subsurface layers. Suppression agents can be gas or liquid. More invasive cooling methods include total or partial flooding with water on the surface.

Smothering exploits the experimental observations by Ohlemiller [1], Palmer [7] and Walther et al. [8], showing that if the concentration of oxygen is reduced below a critical value, the oxidation reaction will stop and insufficient heat will be released. This critical concentration has not been studied in detail, however for smouldering peat

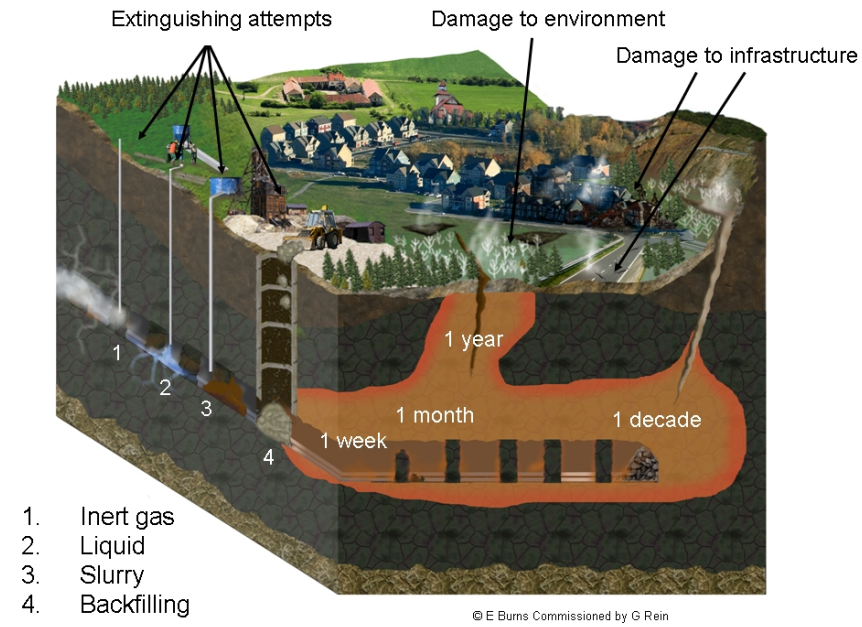

Figure 4.1. Artistic conception of a smouldering fire in an abandoned coal mine and illustration of possible fire damage and suppression attempts. Illustration by E. Burns, 2008 (commissioned by G. Rein, University of Edinburgh).

fires is found to be around 16% [9]. This can be attempted by covering the area of the fire with a 'cap' to seal it from oxygen ingress. More expensive and invasive methods to block oxygen pathways include back-filling or flooding with water.

Because oxygen supply has the strongest effect on the smouldering spread rate [1, 4, 9], it might be tempting then to assume that smothering by oxygen displacement is the most effective way to suppress the fire. However, the size and thermal properties of coal seams, which are typically on the order of 100 m in length with thickness ranging 1 to 6 m [10], play an important role. The thermal inertia of coal is high and it is generally well insulated by adjacent rock or soil (k = 0.13 W·m^{-1}·K^{-1}, ρ = 1300–1500 kg·m^{-3} and Cp = 0.8–1.6 kJ·kg^{-1}·K^{-1} [11]). This would require that oxygen is displaced below the critical concentration for long periods of time for the material to cool naturally to a temperature low enough to prevent re-ignition. For example, a sphere of 1 m will take on the order of 100 days to cool from 900°C to 80°C when the ambient ground temperature is 10°C. For larger masses, natural cooling will take longer. Therefore, the method by which oxygen is excluded must remain operational for extended periods of time. It is thought that poorly maintained exclusion methods will fail within one

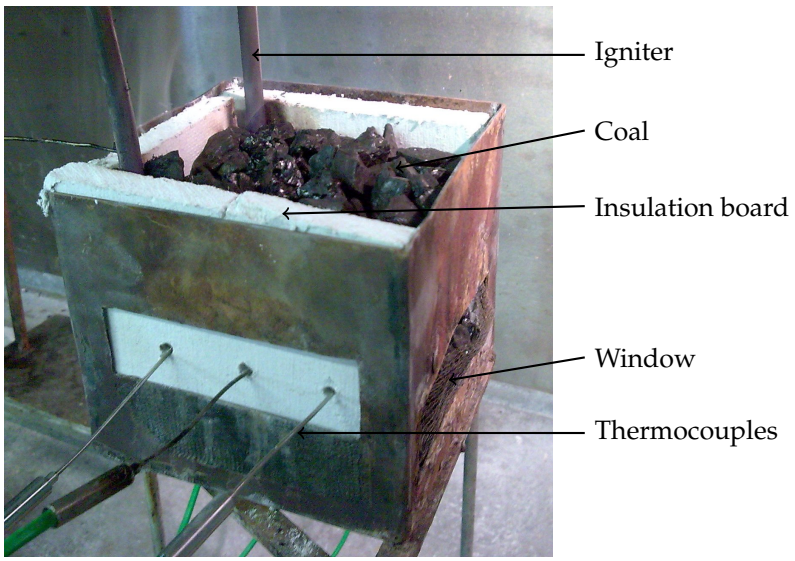

Figure 4.2. The experimental apparatus with key features labelled.

to three years [5]. For these reasons, it is considered that oxygen displacement is a long-term and secondary approach to suppress subsurface fires.

Suppression by forced cooling, the objective of this paper, offers results in shorter time scales and potentially higher efficiency. However, the process is still not well understood and requires further study if it is to be implemented efficiently to real fires.

4.4 Experimental work

The experiments were conducted in a $100\times100\times100$ mm^3 box constructed from steel, lined with insulating board on the vertical faces and open at the top. Coal samples occupy all the free volume of the box. A U-shaped electrical heater of length 290 mm is introduced on one side of the sample as an ignition source. The setup is based on that of Rein et al. [2] for studying peat fires. Opposite the heater, a window measuring 95×30 mm^2 is created on the wall and the bottom of the box has 25 uniformly distributed holes measuring 6 mm in diameter. These holes allow air to flow through the coal sample to assist combustion. K-type thermocouples were placed at seven locations in the sample: one on the heater and six spaced in three rows of two thermocouples at distances 20, 50 and 90 mm from the igniter at a depth of 50 mm. The experimental set-up is shown in Fig. 4.2. The temperature traces were used to infer ignition, propagation rate, smouldering temperature, oxygen dependence and suppression.

Anthracitic coal was used in these experiments (Premium House Coal, CPL Distribution, UK). The true density was measured to be 1200±3% kg·m^3. The ignition protocol consisted of supplying the heater with approximately 80 W for 150 min. This protocol was chosen as a strong ignition source minimises sensitivity of the results to the ignition protocol and allows ignition across a wide range of particle sizes.

The ignition and suppression experiments were undertaken as a function of the particle size of the coal. The original coal particles were broken and sorted by measuring the longest side of the pieces. The mean particle size ranges used were 7±3 mm, 10±5 mm, 15±5 mm, 20±5 mm, 25±5 mm, 30±10 mm, 35±5 mm and 45±5 mm.

4.4.1 Base case experiment

Before the experimental series is conducted, it is necessary to define an experimental protocol capable of providing a repeatable smouldering fire. This led to the definition of the ignition protocol presented above. In order to ensure the suppression results were independent of the ignition protocol used, the smouldering fire was allowed to develop for 150 min after ignition before suppression was attempted. For the particle sizes studied, this is enough time for the fire to spread and involve the entire sample mass upon commencing the suppression.

Figure 4.3 shows the temperature traces for experiments using (a) 15 mm, (b) 30 mm and (c) 40 mm particles. The temperature profile near the igniter is seen to be governed by the heat applied by the igniter until approximately 50 min for 15 mm particles (Fig. 4.3a) and 125 min for the larger particles (Figs 4.3b and 4.3c). The sudden change in gradient at these times indicates ignition and additional heat release in this region. After ignition, the reaction is then seen to propagate away from the igniter. In all cases, the spread of a strong smouldering front to 90 mm away from the igniter after it has been switched off indicates that the fire is self-sustaining. The maximum temperatures are reached just prior to suppression at 300 min. The spread rate can be calculated using the average temperatures in each location and the distance between them. The average spread rate for 30 mm particles is 0.11±0.3 mm·min^{-1} (the same order of magnitude reported by Nolter and Vice [12] for the Centralia mine fire which advanced at an average of 20 m/year). At 300 min, the suppression is started and the temperatures

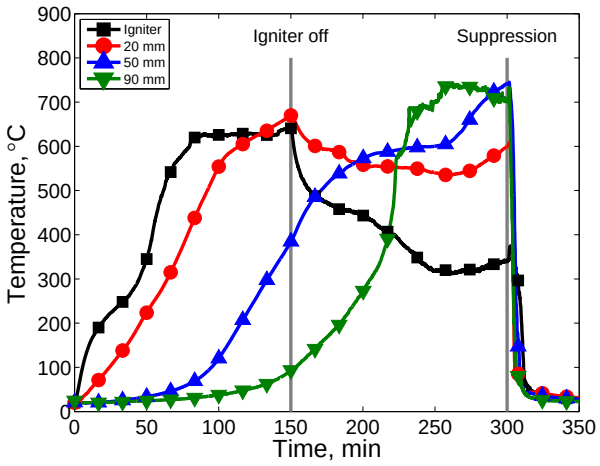

(a)

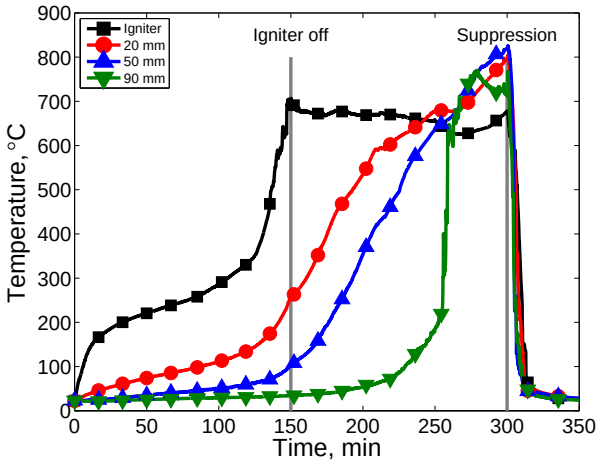

(b)

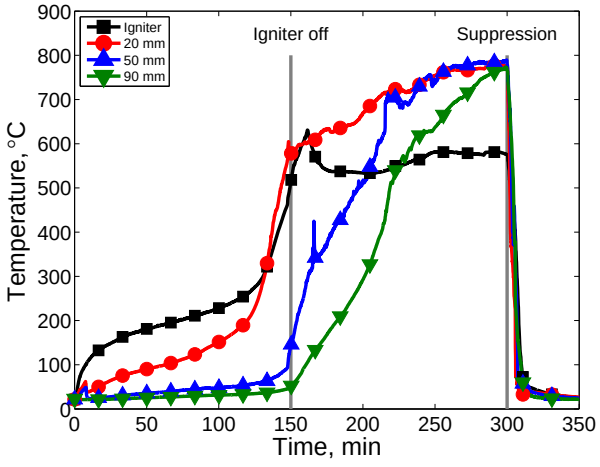

(c)

Figure 4.3. Temperature measurements for samples of (a) 15 mm, (b) 30 mm and (c) 40 mm particle size. The black line is temperature at the igniter, red is the average temperature 20 mm from the igniter, blue is 50 mm and green 90 mm from the igniter.

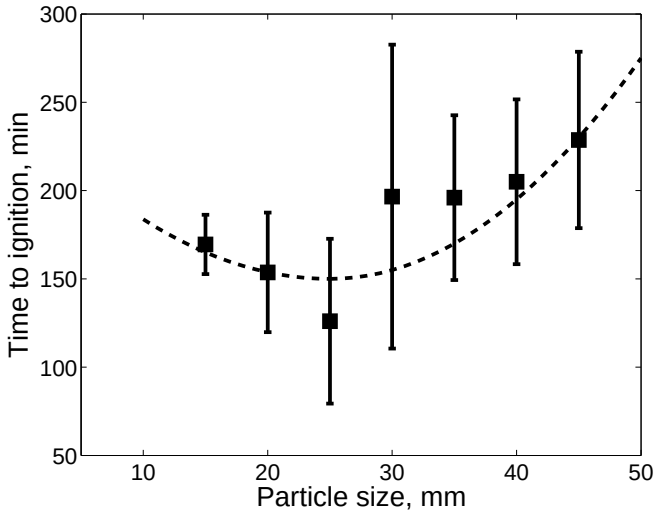

Figure 4.4. Experimentally observed relationship between time to ignition and particle size. Error bars show the maximum and minimum values for between three and five repeats.

decrease rapidly.

4.4.2 Ignition and propagation experiments

The effect of particle size on the ignition and propagation dynamics was investigated. Particle size affects the porosity of the coal sample, the flow permeability, the effective thermal conductivity and the surface area available for heterogeneous reactions. Figure 4.4 shows the time to ignition for samples of different particle size. Ignition is deemed to occur when temperatures measured 50 mm from the igniter exceed those at 20 mm from the igniter. This criterion was chosen as it is independent of heat transfer effects from to the igniter and infers a chemical reaction with net heat release has been established. It can be seen in Fig. 4.4 that the ignition time decreases from 170 min for particles of 15 mm to 125 min for particles of 30 mm in size but then begins to increase as heat transfer to the larger coal becomes more significant up to 220 min for particles of 45 mm. It was not possible to ignite particles smaller than 7 mm in the time scale of these experiments (150 min). This suggests that for small particles, the reaction is limited by oxygen flow to through the bed and for larger particles, heat transfer to the coal plays an important role in the ignition.

Figure 4.5 shows the maximum smouldering temperature as a function of particle size. For particles greater than 15 mm, the maximum temperature is unaffected by the

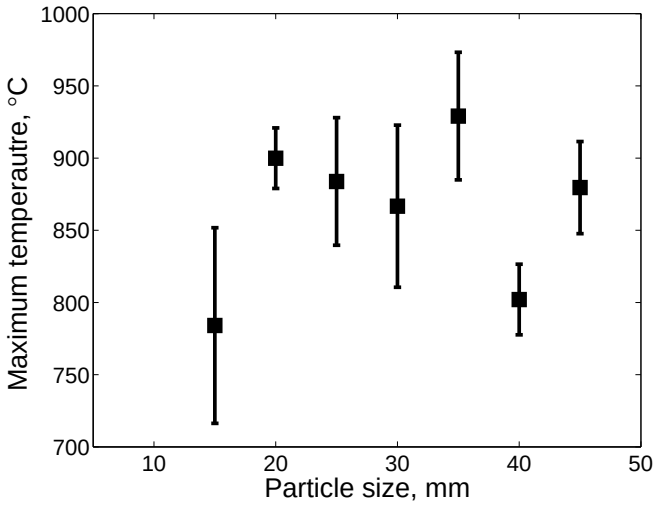

Figure 4.5. Experimentally observed relationship between maximum smouldering temperature and particle size. Error bars show the maximum and minimum values for between three and five repeats.

particle size with temperatures in the range 720–930°C being observed. These temperatures are similar to measurements in the field [5, 13] and in large-scale experiments [14].

The extent of the reaction can be obtained by the mass loss of the coal during the experiment. This was defined by measuring the oven-dried final mass of coal and subtracting this from the initial mass of coal to obtain the total mass lost in the experiment. The average mass loss as a function of particle size is shown in Fig. 4.6. The relationship shows that for particles larger than 20 mm, the mass loss remains constant at around 40% suggesting that the extent of the reaction is a weak function of particle size. This is possibly the result of increased permeability to flow for the large particles compared to smaller particle beds where the spread is limited by low flow permeability.

4.4.3 Suppression experiments

The effectiveness of three suppression mechanisms was studied: single point injection, shower and spray. Water was used as the suppression agent. The single point injection was a pipe positioned 10 mm below the surface of the sample. Water was allowed to flow freely through the pipe into the coal. The shower was generated by allowing water to flow through holes of 4 mm diameter in the bottom of a liquid reservoir and

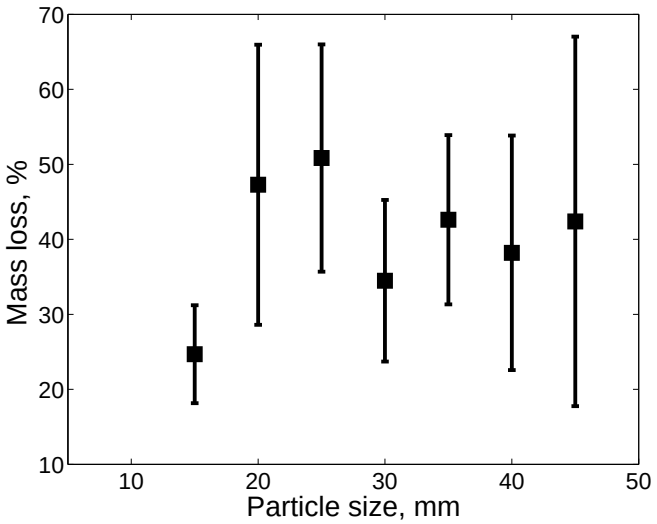

Figure 4.6. Experimentally observed relationship between mass loss after suppression and particle size. Error bars show the maximum and minimum values for between three and five repeats.

the spray was generated using a hand operated atomizer. The water flow rates of each method are 10 ml·s^{-1}, 10 ml·s^{-1} and 2 ml·s^{-1} respectively.

The fire was deemed extinguished when all the temperature measurements in the box were below 50°C, as this is below the self ignition temperature found by Kuenzer et al. [13] and Zhang et al. [14]. Measurements of the amount of water required for suppression were made by measuring the duration of the application and multiplying by the flow rate specific to each suppression method. The run-off generated was collected and measured immediately after suppression. Run-off gives an indication of efficiency as large values mean that more water has to be applied to achieve the same suppression effect. A method which results in low run-off will therefore be more efficient. Temperature plots at the time of suppression for each of the suppression methods are shown in Fig. 4.7. The pipe (Fig. 4.7a) is seen to take around 10 min from the beginning of suppression until temperatures in the bed reach 50°C. Figure 4.7b shows that cooling due to the shower takes 1–2 min while cooling with the spray (Fig. 4.7c) also takes around 10 min.

The results of water required and run-off for each suppression method can be seen in Fig. 4.8. The most efficient method with respect to total water required is the shower, however using a spray results in less water run-off and better control of the flow. The injection pipe is significantly less efficient, requiring three times more water than a

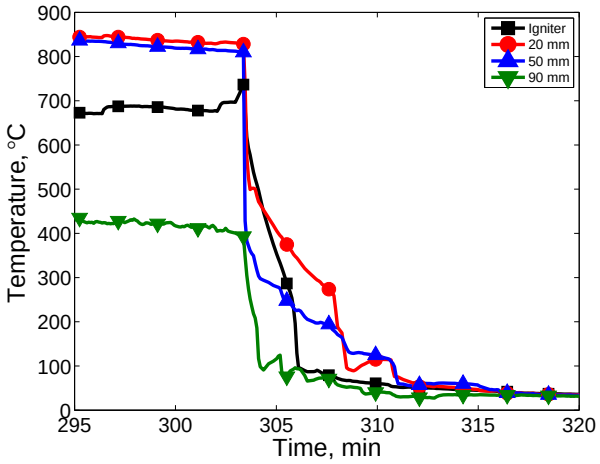

(a)

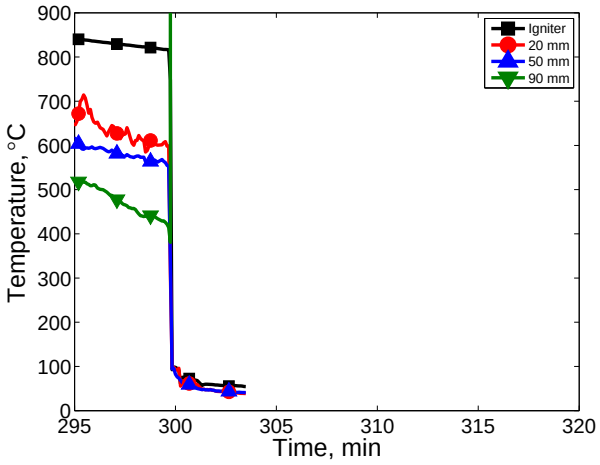

(b)

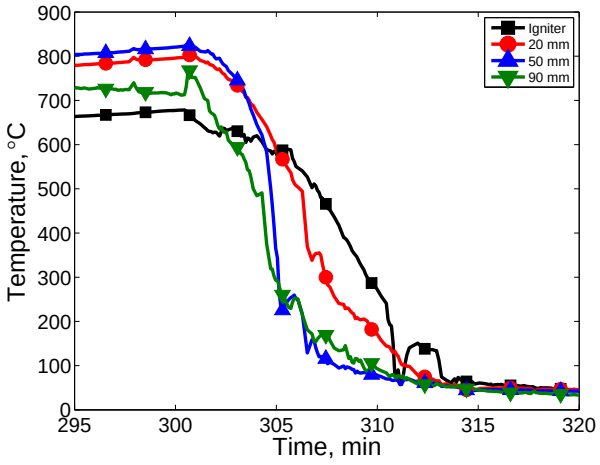

(c)

Figure 4.7. Temperature profiles at suppression for different methods. (a) the pipe which takes approximately 5 min to cool the material, (b) the shower which cools the material rapidly and (c) the spray which takes 10 min to cool the material. The black line is temperature at the igniter, red is the average temperature 20 mm from the igniter, blue is 50 mm and green 90 mm from the igniter.

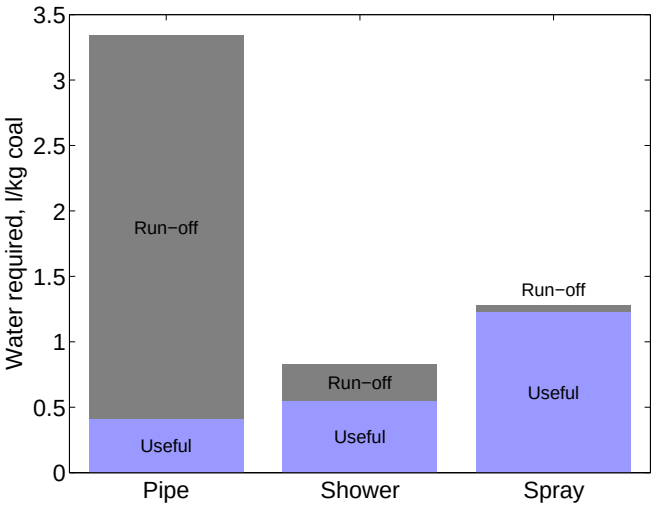

Figure 4.8. Comparison of suppression methods showing effective or absorbed water (blue) and run-off (gray) for coal particles of diameter 30 mm.

spray of which more than 80% is lost as run-off.

The reason for the poor performance of the injection pipe was observed to be due to channelling of the liquid through the coal bed. Channelling arises when the majority of the water takes the same flow path through the bed. The result is that the contact surface area between the water and the coal is small and there is little global evaporation which results in poor heat transfer. This, coupled with a low residence time of water, results in large quantities of water being required.

The shower reduces this problem by applying the water over a larger area. This results in the coal being cooled more uniformly and the generation of steam occurs throughout the bed, assisting the extinguishing by displacing the oxygen. However, the large volumetric flow rate results in high liquid velocities through the bed which again results in channelling, larger run-off and poor control of the flow. The spray allows greater control of the water application and more uniform distribution across the free surface of the coal. It is believed that it is the even distribution of water over the coal surface and lower flow velocity through the bed that leads to the enhanced suppression properties of the spray. The droplet form of the water is not believed to be a significant mechanism as these agglomerate upon contact with the surface.

Figure 4.9 shows the amount of water required using a spray to extinguish the small-scale smouldering fires. The water required is expressed per unit mass of burning

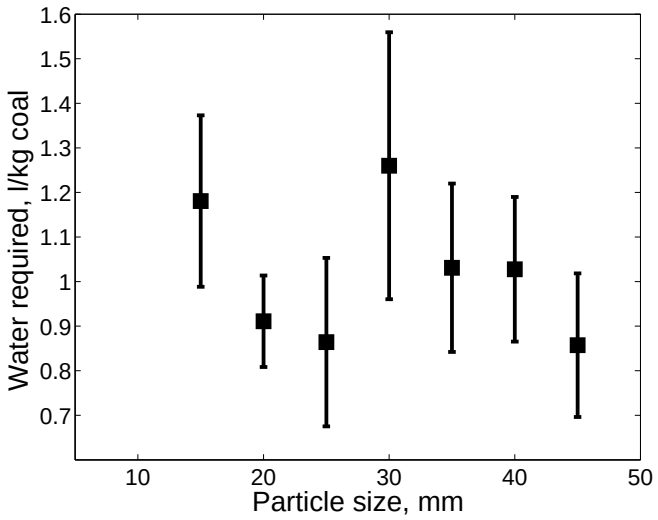

Figure 4.9. Experimentally observed relationship between water required for extinguishing per burning coal mass vs. particle size using a spray. Error bars show the maximum and minimum values for between three and five repeats.

coal assuming that the entire bed is burning at the time suppression is attempted. This assumption is confirmed by visual observation and temperature measurements in all experiments. The trend suggests that the amount of water per mass of coal decreases with particle size and levels off for larger particles.

The measurements of the volume of water per burning coal mass required to extinguish a smouldering fire is in the range 0.9–1.4 $\mathrm{l{\cdot}kg^{-1}}$. A figure larger than this could be required in field-scale fires to account for the water lost due to the complex flow path through the subsurface.

Using the thermal properties of coal and water and the average temperature at the time of suppression, the theoretical quantity of water required per mass of burning coal can be estimated by

$$m_w = \frac{m_c C_{p,c} \Delta T_c}{C_{p,w} (100 - T_w) + \lambda}, \tag{4.1}$$

where m_w is the mass of water required, m_c is the mass of coal undergoing combustion, $C_{p,c}$ is the specific heat capacity of coal, ΔT_c is the temperature difference between the average coal temperature at the time of suppression and the extinguished coal, T_w is the initial temperature of the water and $C_{p,w}$ and λ are the specific and latent heats of water respectively. It is assumed that the water is heated to 100°C and transformed to steam

upon contact with the burning coal and thereafter is not heated to any significantly higher temperature.

The amount of water required is found to be approximately 0.5 $l \cdot kg^{-1}$. This is the same order of magnitude as the experimental results. The difference can be attributed to the effects of heterogeneous heat transfer, fluid flow and adsorption of water by the coal.

This study is the first time experiments of this nature have been undertaken in the laboratory. Additional work is required to determine the effects of scale in the reaction. Especially important would be determination of a relationship which will allow the scale-up of data from small-scale experiments to allow it to be applied to field-scale subsurface coal fires.

4.5 Conclusions

Small-scale experiments have been used to investigate the ignition and spread of smouldering coal fires and the effectiveness of three water suppression methods on these fires.

The combustion reaction was characterized by maximum temperatures of 720–930°C, which were seen to be independent of particle size for particles larger than 20 mm and the burning rate increased for larger particles. These temperatures are similar to those measured in the field and large-scale experiments [5, 13, 14]. Time to ignition was found to be a function of particle size with a minimum time to ignition of approximately 125 min for particles of size 30 mm. The mass loss after suppression was found to be 40% which was independent of the particle size.

Water was confirmed as an effective suppression agent and was used in small-scale tests. The suppression of subsurface fires is dictated by the ability of the delivery method to reach the source of the fire. It has been shown that in small-scale tests, significant differences in suppression efficiency can arise due to the nature of the application. The amount of water required to suppress a smouldering coal fire was found to be on the order of 0.9 to 1.4 $l \cdot kg^{-1}$ of burning coal.

Further work is required to understand the effects of scale on the reaction and extin-

guishing to allow extrapolation of the results from laboratory scale to real subsurface coal fires.

Acknowledgements

The authors are grateful for the financial support of the Engineering and Physical Sciences Research Council, International Fire Investigators and Consultants Ltd and the Small Grants scheme at the University of Edinburgh. Thanks also to Glenn Stracher for his tireless help in preparing the chapter *Coal and Peat Fires: a Global Perspective, Volume 1: Coal – Geology and Combustion* on which this manuscript is based. The assistance of José Garcia, Murray Galloway, Freddy Jervis and Wolfram Jahn in undertaking the experiments is appreciated.

References

[1] T. J. Ohlemiller. *SFPE Fire Protection Handbook*, chapter 2-10: Smouldering Combustion, pages 2–201–2–210. National Fire Protection Association, Quincy, MA 02269, 3rd edition, 2002.

[2] G. Rein, N. Cleaver, C. Ashton, P. Pironi, and J. L. Torero. The severity of smouldering peat fires and damage to the forest soil. *Catena*, 74(3):304–309, 2008. doi: 10.1016/j.catena.2008.05.008.

[3] G. Rein. Smouldering combustion phenomena in science and technology. *International Review of Chemical Engineering*, 1:3–18, 2009. URL hdl.handle.net/1842/2678.

[4] G. Rein, S. Cohen, and A. Simeoni. Carbon emissions from smouldering peat in shallow and strong fronts. *Proceedings of the Combustion Institute*, 32(2):2489–2496, 2009. doi: 10.1016/j.proci.2008.07.008.

[5] A. G. Kim. Cryogenic injection to control a coal waste bank fire. *International Journal of Coal Geology*, 59(1-2):63–73, 2004. doi: 10.1016/j.coal.2003.08.009.

[6] G. J. Colaizzi. Prevention, control and/or extinguishment of coal seam fires using cellular grout. *International Journal of Coal Geology*, 59(1-2):75–81, 2004. doi: 10.1016/j.coal.2003.11.004.

[7] K. N. Palmer. Smouldering combustion in dusts and firbous materials. *Combustion and Flame*, 1:129–154, 1957.

[8] D. C. Walther, R. A. Anthenien, and A. C. Fernandez Pello. Smolder ignition of polyurethane foam: effect of oxygen concentration. *Fire Safety Journal*, 34(4): 343–359, 2000. doi: 10.1016/S0379-7112(00)00007-2.

[9] C. M. Belcher, J. M. Yearsley, R. M. Hadden, J. C. McElwain, and G. Rein. Baseline intrinsic flammability of Earth's ecosystems estimated from paleoatmospheric oxygen over the past 350 million years. *Proceedings of the National Academy of Sciences*, 107(52):22448–22453, 2010. doi: 10.1073/pnas.1011974107.

[10] D. Murchison and T. S. Westol, editors. *Coal and coal bearing strata*. Oliver & Boyd, 1968.

[11] V. Babrauskas. *Ignition Handbook*, chapter 14, pages 719–724. Fire Science Publishers, 2003.

[12] M. A. Nolter and D. H. Vice. Looking back at the Centralia coal fire: a synopsis of its present status. *International Journal of Coal Geology*, 59(1-2):99–106, 2004. doi: 10.1016/j.coal.2003.12.008.

[13] C. Kuenzer, J. Zhang, A. Tetzlaff, P. van Dijk, S. Voigt, H. Mehl, and W. Wagner. Uncontrolled coal fires and their environmental impacts: Investigating two arid mining regions in north-central China. *Applied Geography*, 27(1):42–62, 2007. doi: 10.1016/j.apgeog.2006.09.007.

[14] J. Zhang, C. Kuenzer, A. Tetzlaff, D. Oertel, B. Zhukov, and W. Wagner. Thermal characteristics of coal fires 2: Results of measurements on simulated coal fires. *Journal of Applied Geophysics*, 63(3-4):135–147, 2007. doi: 10.1016/j.jappgeo.2007.08.003.

5

Dynamics of smouldering peat fires under controlled conditions

Summary

Smouldering peat fires are a significant threat to the natural environment. These fires contribute to greenhouse gas emissions, consume large quantities of biomass and damage ecosystems. A series of small-scale experiments has been carried out in the FM Global Fire Propagation Apparatus under a range of heat fluxes and oxidizer flows to investigate the effect these conditions have on the smoulder. Mass loss, in-depth temperatures, char evolution and CO and CO_2 emissions are recorded and used to study the smoulder reaction. Two regimes are observed; the first corresponds to the progression of the pyrolysis front through the sample and is strongly influenced by the applied heat flux, and the second is char oxidation which is more strongly influenced by the flow of air to the reaction zone. Regime I is characterized by a peak in mass loss rate, increasing temperatures near the surface of the sample and low yields of CO and CO_2, while Regime II corresponds to lower mass loss rate, high temperatures at the bottom the sample and higher yields of CO and CO_2. This is the first time that smouldering has been studied in this configuration. The results can be used to understand real peat fire events and smouldering in similar fuels and configurations.

5.1 Introduction

Peat is a naturally occurring fuel which is formed by the anaerobic decay of organic material in acidic conditions. It has a high carbon content and will undergo exothermic oxidation if it is heated in the presence of oxygen [1]. As with other cellulose-based fuels, when ignited, it can undergo smouldering combustion. Smouldering burns slowly, propagating through a mass of material driven by the heat released from the heterogeneous, exothermic reaction of oxygen and the carbon-rich solid fuel [2–4]. The long duration means that smouldering contributes significantly to the damage to the ecosystem as well as the release of carbon and aerosol emissions during real peat fires. During the large peat fires that occurred in Indonesia in 1997, Page et al. [5] estimated that 0.8–2.6 Pg of carbon was released to the atmosphere (13–40% of annual global carbon emissions from fossil fuel burning) and that peat fires accounted for 20% of the burnt area but resulted in 94% of the total emissions. Therefore, understanding these types of fires is vital to aid understanding of fires in the natural environment and their impact on climate and the ecosystem.

The smoulder behaviour of peat has previously been studied by Fransden [1, 6, 7]. Ignition was studied as a function of moisture and organic contents, and bulk density. It was found that ignition was likely at moisture contents lower than 90% and that there existed a relationship between the organic and moisture contents of peat which would permit combustion. In general, peat with higher organic content could burn at higher moisture levels. Using oxygen consumption calorimetry, he showed that the heat evolved from smouldering peat fires was $14.2 \pm 4.5\%$ MJ·kg^{-1}; however, the use of this method for smouldering fires has not been verified. Rein et al. [8, 9] studied the effect of moisture content on ignition, smoulder intensity and spread in small-scale experiments using boreal peat and a strong ignition source. They found that ignition and sustained combustion would only occur below a critical moisture content of 125% on a dry basis. Temperatures in excess of 300°C for periods of over an hour, and mass loss of greater than 90% after combustion were recorded.

Belcher et al. [10] studied the effect of oxygen concentration on the propagation of peat fires. Using an experimental set-up similar to that of Rein et al. [8], samples of

dry peat were ignited in oxygen atmospheres ranging from 13–21%. The spread of the smoulder was observed to identify the effect of oxygen concentration on the smoulder reaction. It was found that smoulder would not propagate at oxygen concentrations lower than 16%.

Emissions from smouldering peat have been studied by Rein et al. [9] using the cone calorimeter. Samples of peat were exposed to heat fluxes between 30 and 70 $kW \cdot m^{-2}$. The yield of CO and CO_2 on a dry base were found to be 0.17 and 0.42 $kg \cdot kg^{-1}$ respectively, while the CO/CO_2 ratio was around 0.3–0.6 $kg \cdot kg^{-1}$. The CO yield was independent of incident heat flux and moisture content while the CO_2 was weakly dependent on these variables. The emissions of smouldering Indonesian peat with 30% moisture content (dry base) were studied by Christial et al. [11]. They found a CO/CO_2 ratio of 0.04 $kg \cdot kg^{-1}$; however, smouldering is not quantified nor are the time evolution data of the smoulder given.

Smouldering fires are known to be controlled by the heat losses from and the oxidizer flux to the reaction zone [3, 4]. In order to study smouldering in the laboratory, it is necessary to control these conditions. The heat losses can be controlled by altering the heat balance of the system, for example increasing the size of a sample will increase the insulation of the reaction front and applying an external heat flux will reduce the effect of the heat losses [8, 9]. Meanwhile, the oxidizer flux to the reaction can be altered in two ways: either the velocity of the air flow can be controlled [12–15] or constant flow rates with varying oxygen concentrations can be used [10, 13]. The former results in a more complex set-up because the increased oxidizer flow is coupled with an increase in the convective heat losses from the reaction zone.

In this paper, we use a novel methodology to control both of these governing mechanisms of smouldering in peat in order to understand the dynamics of smouldering in this material. The data obtained from experiments are analysed in order to understand the dynamics of peat smouldering across a wide range of burning conditions. Mass loss rate, temperature, char fraction evolution and emission data are used to describe the smouldering process.

5.2 Experimental set-up

Experiments were carried out using the FM Global Fire Propagation Apparatus [16], a small-scale calorimeter commonly used to determine the combustion characteristics of materials. A schematic of the apparatus is shown in Fig. 5.1. Four halogen lamps provide a uniform heat flux across the surface of a sample of diameter 125 mm and depth 30 mm. The environment in which the combustion occurs can be controlled with respect to the flow velocity and composition. The mass loss, temperatures in the sample and composition of exhaust gases are measured and used to characterize the smouldering behaviour under given conditions. No pilot flame is used in these experiments as flaming combustion is not of interest. The sample holder is constructed from 2 mm thick steel mesh with porosity of 26%, to allow the oxidizer to flow through the sample (see Schemel et al. [17]), resulting in a more realistic smouldering environment compared to previous work [9]. The initial mass of peat was constant at approximately 80 g. Temperature measurements were made using K-type thermocouples located on the surface, 10, 20 and 30 mm below the surface on which the heat flux is incident. Data were recorded every second for the duration of the experiment.

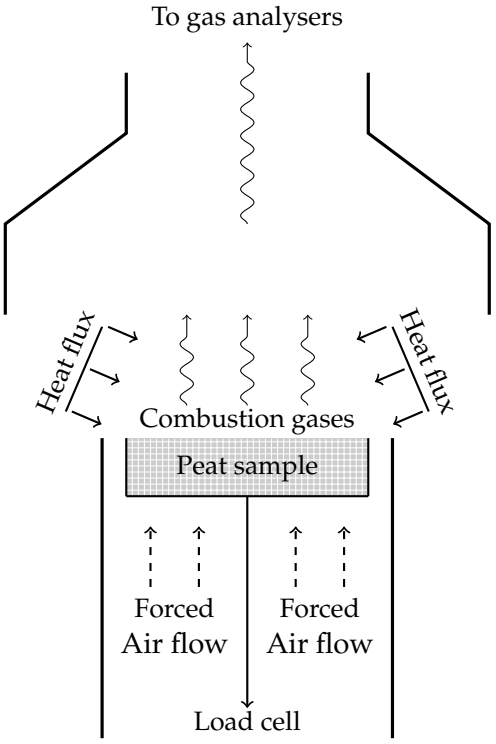

Figure 5.1. Schematic of the FPA.

Commercially available sphagnum moss peat was used in these experiments. This peat is available in the UK under the brand Shamrock Irish Moss Peat. Commercial peat has the advantages of being easy to obtain consistently, and having a homogeneous structure with few twigs, roots and other vegetable matter which occur in natural fuels. This material has been studied previously by Belcher et al [10]. The peat is oven-dried at 80°C for at least 48 h to ensure all moisture has been removed, before being allowed to cool to ambient temperature in sealed polythene bags for at least 3 hours prior to testing. The bulk density of the peat after drying is approximately 220 $kg \cdot m^{-3}$. Drying ensures constant sample composition and allows a simplified analysis to be undertaken as the water evaporation mechanism is removed from the reaction framework. This results in a conservative estimate of burning rates in natural environments. The applied heat flux is incident on the downstream (top) surface of the sample (with respect to the oxidizer flow). Experiments were undertaken at heat fluxes of 7.5, 10, 20, 30 and 40 $kW \cdot m^{-2}$ and air flows of 0, 40, 70 and 300 $mm \cdot s^{-1}$. The heat flux received by the sample is uniform across the surface to within 10%. Three types of heat flux exposure were studied: 1 min, 10 min and for the duration of the experiment. Unless specified, heat fluxes relate to the full duration exposure. The 1 min exposure was used to allow the smoulder reaction to develop naturally after ignition such that the char and peat fractions of the sample could be recorded at different stages of the reaction. This involved removing the sample from the apparatus and measuring the quantities of char and peat remaining. The 10 min exposure experiments were used to assess the degree to which the applied heat flux affected the reaction. In order to understand the simultaneous and competing reactions of oxidation and pyrolysis, additional experiments were carried out under flow of 70 $mm \cdot s^{-1}$ of pure nitrogen. The use of nitrogen allows the study of the pyrolysis reactions which occur within the peat without the effects of the oxidation reactions. Experiments were terminated when the mass loss rate had reduced to zero and the concentrations of CO and CO_2 had returned to steady, ambient concentrations.

5.2.1 Flow characterization

The flow through the porous fuel is known to affect the smoulder dynamics [18]. Therefore, it is necessary to define the flow field around and through the sample. Flow speeds corresponding to volumetric flow rates of 50, 100 and 200 $l \cdot min^{-1}$ around the sample are measured. The upstream flow (i.e. before impingement on the sample), was characterized by measuring the flow speed in five upstream locations using a hot wire anemometer. Measurements were taken at the centre of the flow duct, and at points 70 and 140 mm along the radius at 90° intervals in the absence of the sample and applied heat flux. With a sample in place (and no heat flux), the flow was measured at four points between the edge of the sample holder and edge of the flow duct. The flow speed through the sample could then be calculated. The upstream flow speeds and calculated flow speeds through the sample are given in Table 5.1.

Before impingement, average upstream speeds range from 40 to 400 $mm \cdot s^{-1}$. The velocity at 50 $l \cdot min^{-1}$ was lower than the sensitivity of the device but a calculation suggests a value of the order 40 $mm \cdot s^{-1}$. The flow around the sample was considerably higher than the upstream flow and ranged from 120 ± 30 to 830 ± 200 $mm \cdot s^{-1}$. This is because the pressure drop through the peat results in most flow going around the sample and only a small fraction through the sample. The flow through the sample was calculated by a mass balance of the flow around and upstream of the sample. These flows are also shown in Table 6.1. Flow above the sample of 130 $mm \cdot s^{-1}$ was measured at a flow rate of 200 $l \cdot min^{-1}$; this is within the calculated range, showing that the calculation yields reliable results. The exact flow field will be altered by the buoyant flow induced by the heating of the sample, therefore reference is made to the upstream velocity when discussing the experimental conditions.

Table 5.1. Range of upstream flow speed and calculated flow speed through the sample for the volumetric flow rates studied. Flow of 130 $mm \cdot s^{-1}$ was measured above the sample in the case of the 200 $l \cdot min^{-1}$ flow, suggesting that the calculations are reliable.

Flow rate, $l \cdot min^{-1}$	Upstream speed, $mm \cdot s^{-1}$ Measured range	Flow through sample, $mm \cdot s^{-1}$ Calculated range
50	40	0–15
100	20–150	50–90
200	130–400	120–300

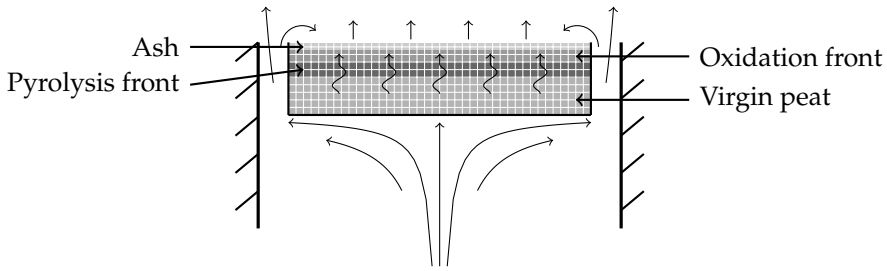

Figure 5.2. Schematic of the flow field around and through a sample of peat in the FPA and the relative positions of the pyrolysis and oxidation fronts near the beginning of the experiment.

5.2.2 Test matrix

Table 5.2 shows the test matrix for the experiments carried out in this work. Thirty-eight experiments were carried out with constant exposure to the heat flux, twenty-six experiments with 10 min exposure and eleven with constant heat flux exposure in nitrogen atmosphere. Experiments were repeated to ensure consistency of results and to provide estimates of the error. In total, results from 75 experiments are reported. Twenty-six additional experiments were undertaken with 1 min exposure to a heat flux of 20 $kW \cdot m^{-2}$ and a flow of 70 $mm \cdot s^{-1}$ in order to assess the time evolution of the peat and char fractions in the sample.

Most experiments were carried out with the lamps on for the duration of the test and under air atmosphere. The experiments in a nitrogen atmosphere allowed the pyrolysis reactions to be studied independently of the oxidation reactions. Tests where the lamps were turned off after 1 and 10 min are used to study the behaviour of unassisted smoulder propagation. Experiments were repeated to assess the errors and ensure repeatability and consistency of the results.

5.3 Results and discussion

5.3.1 Overview

The mass loss rates for experiments with exposure to 20 $kW \cdot m^{-2}$ for 1 min, 10 min and for the experiment duration under air and nitrogen environments are shown in Fig. 5.3. The 1 min exposure results in a significantly different profile from the 10 min and full duration exposure. In this case, the initial mass loss rate is high as the effects

Table 5.2. Test matrix showing the heat flux/flow conditions under which the experiments were conducted. The experiments are grouped into three sets: continuous exposure to the heat flux, 10 min exposure to the heat flux and constant exposure to the heat flux in a nitrogen atmosphere.

Flow speed $mm \cdot s^{-1}$	Continuous heat flux					10 min exposure					Continuous heat flux N_2 atmosphere				
300	1	2	2	1	2	-	-	-	-	-	-	-	-	-	-
70	3	6	2	1	1	3	2	6	1	-	4	2	2	1	-
40	1	4	1	1	1	-	2	-	-	-	-	1	1	-	-
Natural flow	1	4	4	1	1	1	4	4	2	1	2	3	2	1	1
Heat flux, $kW \cdot m^{-2}$	7.5	10	20	30	40	7.5	10	20	30	40	7.5	10	20	30	40

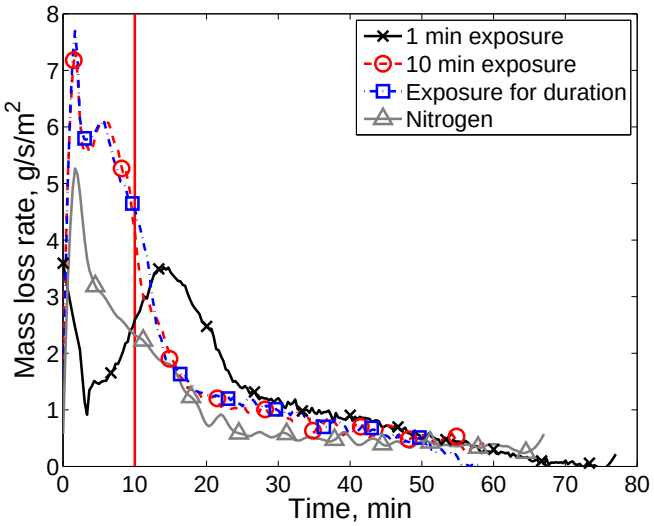

Figure 5.3. Comparison of the mass loss rates for experiments exposed to 20 $kW \cdot m^{-2}$ for 1 min, 10 min and the duration of the experiment.

of the applied heat flux dominate. After the lamps are switched off, the mass loss rate decreases from 3 $g \cdot s^{-1} \cdot m^{-2}$ to 1 $g \cdot s^{-1} \cdot m^{-2}$ before increasing to a maximum of 3.5 $g \cdot s^{-1} \cdot m^{-2}$ during the following 15 min. The mass loss rate then decreases rapidly to around 1.5 $g \cdot s^{-1}$ at around 23 min. After this the mass loss decreases slowly for the next 50 min.

The 10 min and full duration exposure exhibit different behaviour from the 1 min exposure experiments. At the beginning of the experiment, the mass loss rate increases rapidly to 7.5 $g \cdot s^{-1} \cdot m^{-2}$, followed by a slight decay before a second peak. Thereafter, there is a rapid decrease in mass loss rate to around 1.5 $g \cdot s^{-1} \cdot m^{-2}$ at 18 min. The mass loss rate then decreases at a slower rate until around 60 min. The difference

in behaviour between this and the 1 min exposure can be attributed to the effect of the heat flux applied by the lamps on the smoulder reaction. The additional heat supplied by longer durations promotes the pyrolysis reactions and acts to reduce heat losses from the front. This results in a higher mass loss rate under these exposure conditions than the naturally developing smoulder. The difference between the 10 min and full duration exposures is small – there is only a slight decrease in the mass loss rate immediately after the heat flux is switched off. This suggests that at a heat flux of 20 $kW \cdot m^{-2}$ after 10 min, the heat flux has little impact on the reaction. This is especially evident at times greater than 30 min as the mass loss rates for natural smoulder after 1 min exposure, 10 min exposure and full duration exposure are all similarly decreasing from 1 $g \cdot s^{-1} \cdot m^{-2}$.

The mass loss rate for experiments carried out under nitrogen shows different behaviour again. Initially the mass loss rate increases to around 5 $g \cdot s^{-1} \cdot m^{-2}$ at the same time as the initial peak in the experiments carried out under air. The mass loss rate then decreases steadily until around 20 min, when it becomes approximately constant at 0.5 $g \cdot s^{-1} \cdot m^{-2}$ for the duration of the experiment, which was limited by the available nitrogen. This shows that the pyrolysis and oxidative reactions occur in a ratio of around 2:1 at the beginning of the reaction. This also suggests that the secondary peak observed in the mass loss rate under air is due to oxidative reactions, as it is not observed under nitrogen environment.

From these experiments, two regimes of mass loss rate are consistently observed irrespective of the duration of the applied heat flux: an initial regime of high mass loss rate (Regime I) and a second regime of lower and decreasing mass loss rate (Regime II). The following discussion uses and expands upon this framework.

5.3.2 1 min exposure: regime characterization

A series of experiments was undertaken to assess the evolution of the smoulder reaction in the sample. Samples of peat were ignited by exposure to a heat flux of 20 $kW \cdot m^{-2}$ for 1 min and the smoulder reaction was allowed to proceed unassisted. The progress of the reaction was monitored by assessing the fractions of char and peat which remained at various times during the reaction. This was measured by removing the sample from

the apparatus and measuring the mass of char and peat remaining in the sample holder. This was repeated using different samples at different times during the smoulder reaction. Fig. 5.4 shows the evolution of the peat and char fractions in the sample and the mass loss rate as a function of time after exposure to the heat flux. At the beginning of the experiment only peat is present; however, 1 min after the heat flux has been switched off approximately 18% of the initial mass of peat has been lost. This has been converted to char (approximately 12% of the initial mass) and gaseous pyrolysis products. The fraction of peat decreases as the pyrolysis and oxidation fronts propagate through the sample. The rapid decrease in char fraction and formation of a significant quantity (55% of the initial sample mass) of carbon-rich char during the initial 15 min of the reaction means that although pyrolysis and oxidation reactions are occurring, the pyrolysis front is propagating faster than the oxidation front. This corresponds to Regime I. After 15 min, there is no peat remaining and the char fraction reaches a maximum of 55% – this means that the whole sample has been pyrolysed and the pyrolysis reaction cannot continue. From around 25 min until the end of the reaction (70 min) the char fraction decreases as it oxidizes to form gaseous combustion products. This reaction was observed to occur on the upstream side (bottom) of the sample and this period corresponds to Regime II.

The mass loss rate for a 1 min exposure experiment is also shown in Fig. 5.4. The mass loss rate is initially high due to the influence from the incident heat flux. However, after this is shut off, the mass loss rate decreases to around 1 $g \cdot s^{-1} \cdot m^{-2}$ before increasing over the next 10 min to a maximum of 3.4 $g \cdot s^{-1} \cdot m^{-2}$. This peak in mass loss rate occurs just prior to the peak in char fraction, i.e. when both oxidative and pyrolysis reactions are occurring. After the peak in char fraction, the pyrolysis reaction cannot continue and the mass loss rate decreases sharply to around 1.5 $g \cdot s^{-1} \cdot m^{-2}$ at 23 min. This represents the change from Regime I to Regime II where the pyrolysis reaction which dominated Regime I stops and only oxidation can occur. In Regime II, the mass loss rate decreases steadily as the char is oxidized.

During the period of high mass loss, both pyrolysis and oxidation reactions are occurring in the peat. After 20 min, there is no peat remaining and therefore the pyrolysis reaction stops. This results in a rapid decrease in the mass loss rate (as this is

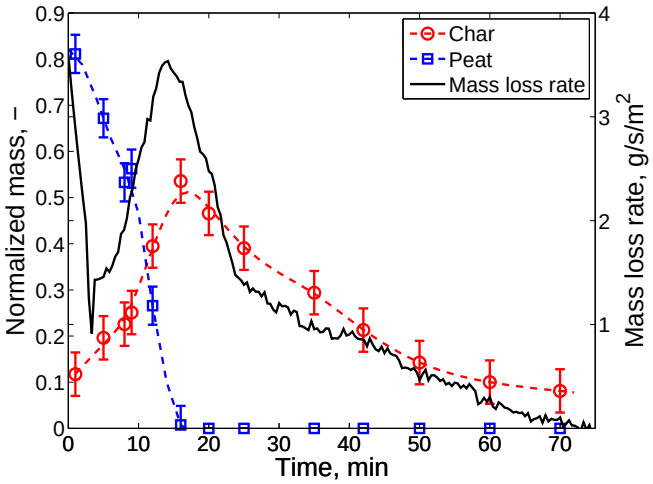

Figure 5.4. The evolution of char and peat fractions throughout the experiment and the mass loss rate. The fraction of peat decreases and the fraction of char increases from the beginning of the experiment until around 20 min. During this period, the pyrolysis front is propagating through the sample, resulting in the formation of char from the thermal decomposition of peat. After 20 min, the pyrolysis front has propagated through the sample and the resulting char is undergoing oxidation to form ash and gaseous products. Error bars represent the average error from three repeats.

now only a result of oxidation reactions) until 23 minutes when only oxidation occurs. This transition occurs when the sample is entirely char and approximately 35% of the initial sample mass remains.

The apparent discrepancy between the peak char and the cessation of the pyrolysis reaction can be attributed to the measurement of the char. This was done visually assuming the peat is converted to char in a one step process. In reality this is not the case and it is likely that the char will pyrolyse further, meaning that the sample will undergo further pyrolysis even though visually it appears to be entirely char.

This analysis leads to the following reaction framework for the experiments with 1 min duration exposure: during the initial phases of the reaction, the pyrolysis and oxidative reactions occur, however the pyrolysis front (driven by the heat released by the oxidative reactions) propagates through the sample faster than the oxidative front and a carbon-rich char is produced – this corresponds to Regime I. Once the pyrolysis reaction has stopped, only oxidation occurs resulting in a lower mass loss rate. This corresponds to Regime II. In this regime, the oxidation of the char is observed to occur on the bottom (upstream) side of the sample, resulting in low mass loss rates as the

reaction is limited by the surface area available for the oxygen to react.

Analysis of the mass loss rates across a wide range of burning conditions indicates that the above framework is consistent. Subsequent analysis is based on these observations.

5.3.3 10 min exposure: mass loss rate and temperature

The effect of the exposure duration was further studied by comparing 10 min exposure to continuous exposure. Figure 5.5 shows a comparison of the mass loss rate for experiments at 10 kW·m^{-2} for the duration of the test and for 10 min, with the transition indicated by the shaded region. It is seen that the mass loss continues in Regime I even after the heat flux is no longer applied, showing that this regime is representative of a self-sustaining smouldering phenomenon. The mass loss behaviour of the 10 min exposure duration experiment in which the lamps are switched off differs only during the period immediately after the lamps have been switched off. At this time, the mass loss rate decreases sharply before increasing again to that of the experiment with the lamps on for the duration. The mass loss rate then continues to decrease and the transition to Regime II occurs at approximately the same time in both experiments (19 and 20 min respectively) indicating that this second regime is independent of the applied heat flux.

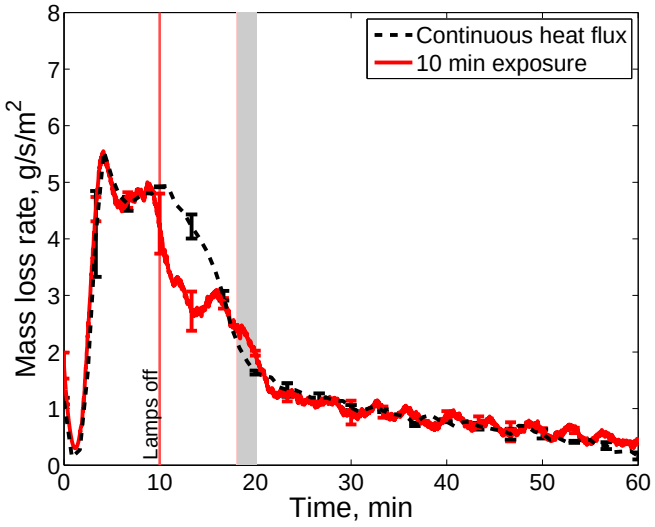

Figure 5.5. Mass loss rates for heat flux of 10 kW·m^{-2} for 10 min and the whole duration, under air environments. This shows the independence of the regimes on the applied heat flux.

Figure 5.6 shows temperature and mass loss data for exposure to 20 kW·m^{-2} for 10 minutes. The maximum recorded surface temperature was 550°C after 9 min (after this time, the thermocouple was observed to become exposed). The temperature 10 mm below the surface reaches a temperature of 500°C after 17 min before also cooling as the surrounding peat is consumed, exposing the thermocouple. Temperatures 20 and 30 mm beneath the surface initially heat rapidly to around 500°C during Regime I then increase at a lower rate to a maximum of 560°C during Regime II. The sustained elevated temperatures are evidence of an exothermic reaction occurring on the bottom (downstream side) of the sample during Regime II.

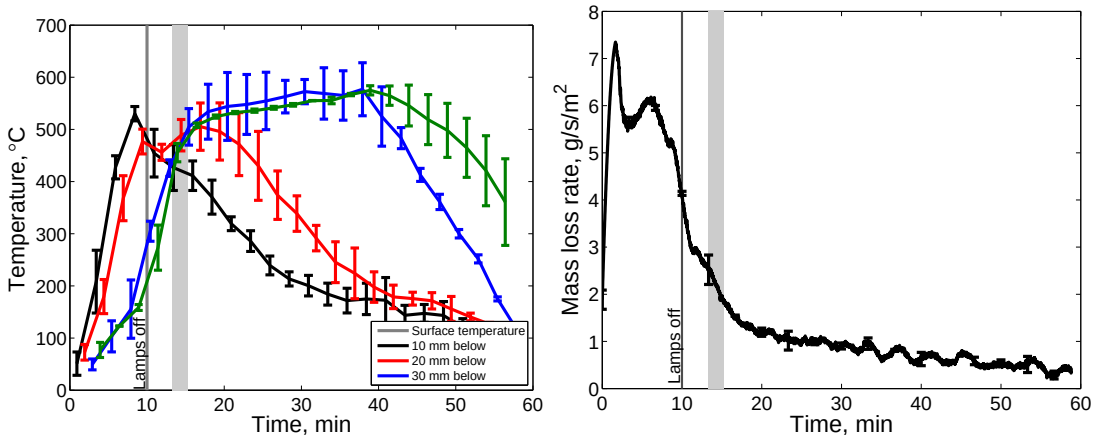

(a) (b)

Figure 5.6. (a) Temperatures at the surface, 10 and 20 mm below the surface and (b) mass loss rate for a sample of peat exposed to 20 kW·m^{-2} for 10 min and subject to a flow of 100 l·min^{-1}.

5.3.4 Constant exposure

The effect of heat flux was studied under exposure to the heat flux for the duration of the experiment. Typical mass loss, mass loss rate, temperature and emissions data collected for experiments at heat fluxes of 7.5, 10 and 20 kW·m^{-2} (applied for the duration of the experiments) and flow of 70 mm·s^{-1} are shown in Fig. 5.7.

Figure 5.7a shows the normalized mass loss for the three experiments. This shows that as the incident heat flux is increased, time to the onset of significant mass loss decreases. It also shows the transition from a period of high mass loss rate at the beginning of the experiment to lower mass loss rate, indicated by the shaded regions.

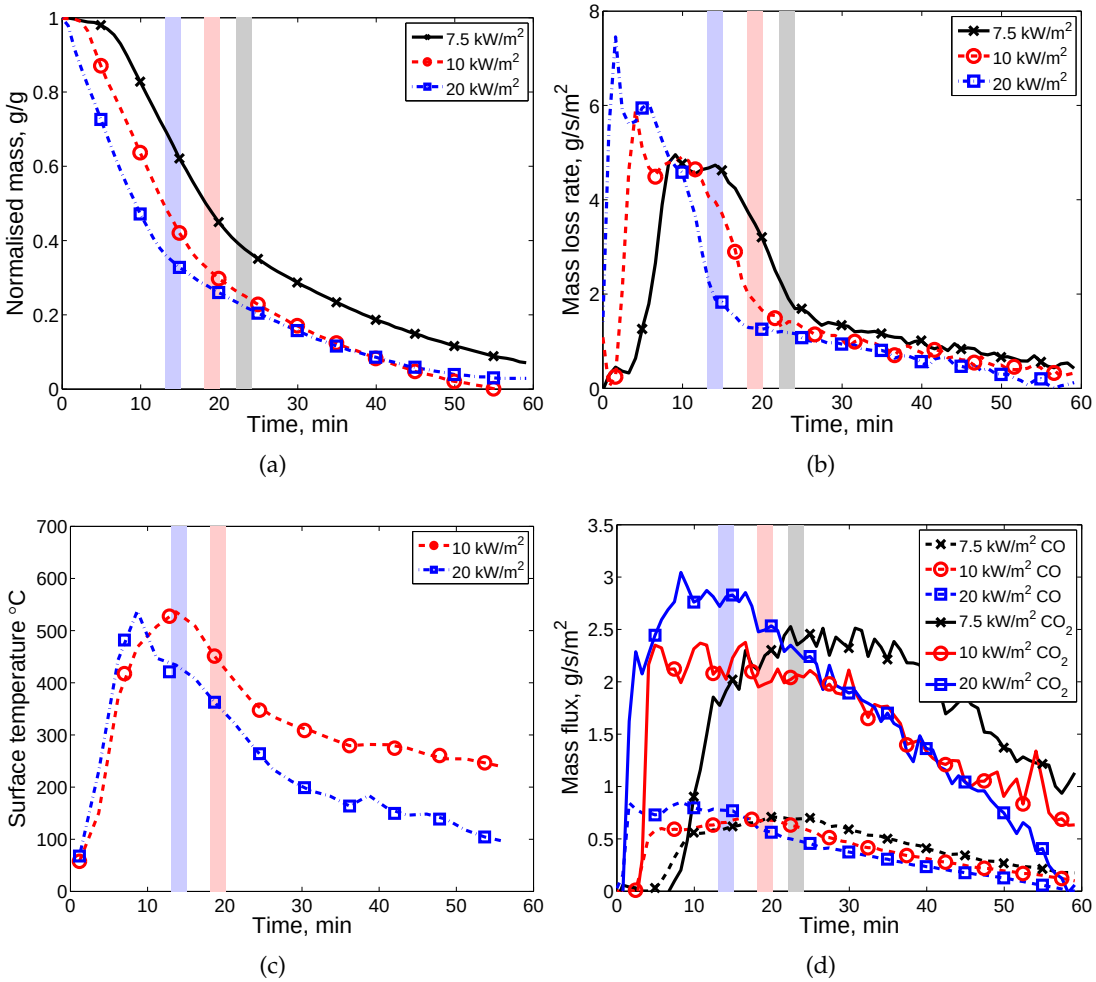

Figure 5.7. (a) Normalized mass, (b) mass loss rates, (c) surface temperatures and (d) CO and CO_2 flux for experiments at 7.5, 10 and 20 kW·m^{-2} and flow of 70 mm·s^{-1}. Two distinctive regimes are shown, the transition between which is highlighted by the shaded regions.

The time of the transition is found by locating the maximum of the second derivative of the mass loss rate curve.

The peak mass loss rate is seen to depend on the applied heat flux. For a heat flux of 7.5 kW·m^{-2}, the mass loss rate increases rapidly to approximately 5 g·s^{-1}·m^{-2} after 10 min. There is then a period of roughly 5 min during which the mass loss rate remains high before it starts to decrease. After a sharp decline to approximately 2 g·s^{-1}·m^{-2} over 10 min, there is a transition in the mass loss rate and it gradually decreases to zero over the next 38 min. Similar trends are seen for exposure to 10 and 20 kW·m^{-2}; the peak mass loss rate at these heat fluxes is 6 and 7.5 g·s^{-1}·m^{-2}, reached in 2 and 4 min respectively.

Surface temperatures (Fig. 5.7c) show that the peak temperature is independent of applied heat flux at around 530°C. However, the time to reach this peak decreases from 14 to 9 min for heat fluxes of 10 and 20 $kW \cdot m^{-2}$. The transition in the mass loss rate occurs at a time just after the peak in surface temperature, indicating that at this time the reaction has propagated away from the surface.

The mass flux of CO and CO_2 for the experiments is shown in Fig. 5.7d. There is little dependence of the magnitude of the peak with heat flux, however the time taken to reach the peak reduces with increasing flux. Typical fluxes are 0.7 $g \cdot s^{-1} \cdot m^{-2}$ for CO and 2.5 $g \cdot s^{-1} \cdot m^{-2}$ for CO_2. The transition corresponds to a time when the flux of emissions begin to decay. The CO flux initially increases at a high rate, before slowing until the transition, when it starts to decrease. The peak CO_2 flux is approximately 3.5 times higher than the peak CO flux.

Using the observations above, the reaction framework based on two regimes is shown to be constant across the wide range of burning conditions studied. The first, Regime I, is the period of high mass loss rate, increasing emissions flux and surface temperature at the beginning of the experiment. This regime is dominated by the pyrolysis front propagating through the sample converting the peat to carbon-rich char, assisted by the heat released by a relatively small amount of oxidation. The second regime is the period of lower mass loss rate, decaying emissions and corresponds to a char oxidation reaction on the bottom, upstream face of the sample during the latter part of the experiment.

5.3.5 Regime characterization

Mass loss rate

The peak mass loss in Regime I for heat fluxes between 7.5 and 40 $kW \cdot m^{-2}$ and natural and forced flows of 70 $mm \cdot s^{-1}$ of air and 70 $mm \cdot s^{-1}$ of nitrogen, is shown in Fig. 5.8. Experiments in nitrogen atmosphere are used to allow the separation of the pyrolysis and oxidative reactions that occur during smouldering in air. The figure shows that the peak mass loss rate under both air and nitrogen environments is a function of the heat flux. Under air, the mass loss rate at 7.5 $kW \cdot m^{-2}$ is approximately 5 $g \cdot s^{-1} \cdot m^{-2}$ and this

increases to 9.5 $g \cdot s^{-1} \cdot m^{-2}$ for heat fluxes of 40 $kW \cdot m^{-2}$. The flow condition (natural or forced) does not appear to affect the mass loss rate. Data for experiments under nitrogen show lower mass loss rate compared to those in an oxidative environment.

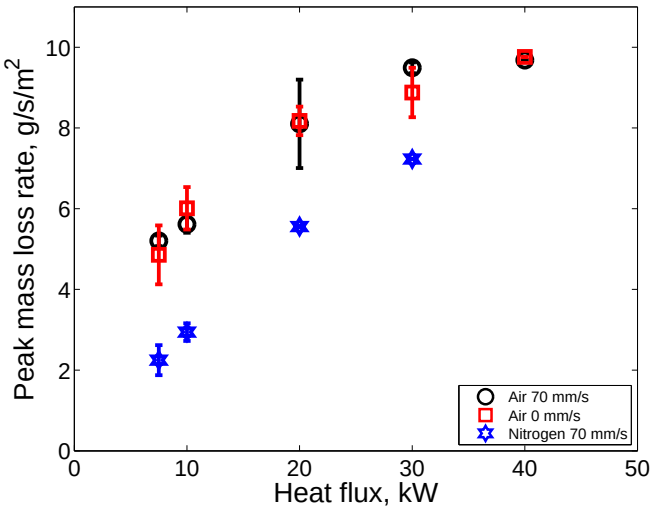

Figure 5.8. The peak mass loss rates in Regime I.

The mass loss rates for experiments under nitrogen environments at heat fluxes of 7.5 and 10 $kW \cdot m^{-2}$ are approximately half the value observed under air. This is because in the former the sample is only undergoing pyrolysis. When oxygen is present, the char formed reacts further to form gaseous products. This additional reaction process results in higher mass loss rates in an oxidative atmosphere compared to pyrolysis alone. At higher heat fluxes, it can be seen that the ratio of mass loss due to oxidation to that of pyrolysis is reduced, as the mass loss rate under nitrogen at 20 $kW \cdot m^{-2}$ is approximately a third lower than under oxidative environment. This suggests that at higher heat fluxes, the oxidation has less effect on the reaction rate compared to low heat fluxes and the reaction becomes dominated by the applied heat flux and pyrolysis reactions.

The time to the peak mass loss rate is presented in Fig. 5.9a. It can be seen that as the heat flux is increased, the time decreases and is negligible above 20 $kW \cdot m^{-2}$. The time to peak mass loss rate correlates well with the visual observations of the gas emissions from the sample.

The duration of Regime I is defined as the time between the beginning of the first peak in mass loss data and end of the period of high mass loss rate (the transition to

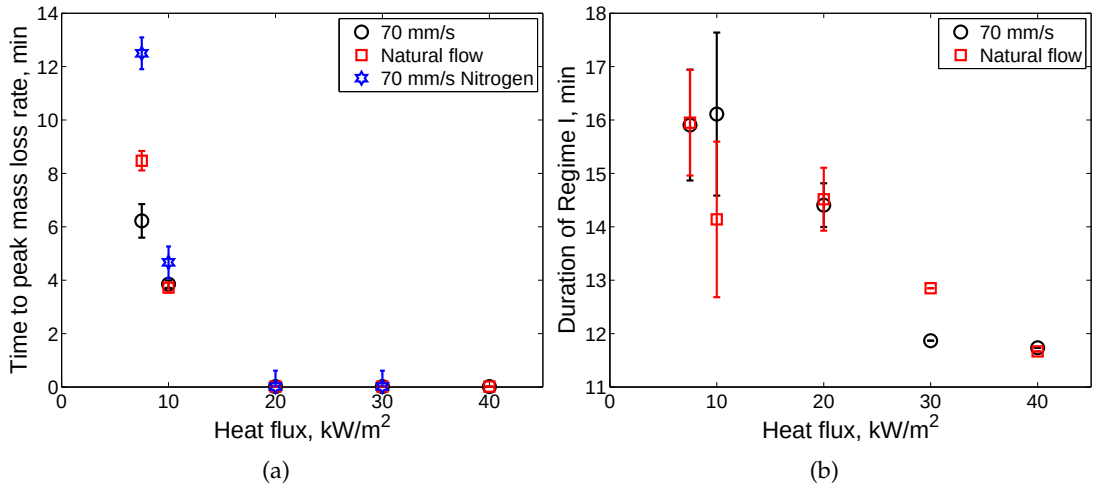

Figure 5.9. (a) The time to reach the peak mass loss rate which is defined as the onset of Regime I and (b) the duration of regime I.

lower mass loss rate in Regime II) and is shown in Fig. 5.9b. It is therefore found by calculating the maximum of the second derivative of the mass loss curve.

It is seen that the duration of Regime I has a strong dependence on the applied heat flux under forced and natural air flow and there is no strong correlation to the supply of oxidizer. The duration ranges from approximately 16 min at heat fluxes of 7.5 $kW \cdot m^{-2}$ to 12 min when the heat flux is increased to 40 $kW \cdot m^{-2}$.

Mass lost at the transition is shown in Fig. 5.10a. It is shown that the transition occurs consistently at mass losses of 65% under air and is independent of the applied heat flux. The constant mass lost confirms the observations made in Section 5.3.2 that the transition occurs after approximately 35% of the sample mass remains as char.

The mass loss rate at the transition is shown in Fig. 5.10b. The transition occurs between 1.5 and 1.9 $g \cdot s^{-1} \cdot m^{-2}$. Under natural flow conditions, the mass loss rate at the transition at low heat fluxes is 1.6 $g \cdot s^{-1} \cdot m^{-2}$, which increases to 1.8 $g \cdot s^{-1} \cdot m^{-2}$ for higher heat fluxes. Meanwhile, for forced flow cases, at low heat fluxes the mass loss rate at transition is 1.7 $g \cdot s^{-1} \cdot m^{-2}$, but at 40 $kW \cdot m^{-2}$ this decreases to 1.6 $g \cdot s^{-1} \cdot m^{-2}$.

The duration of Regime II is shown in Fig. 5.11. The end of Regime II should be the end of the reaction (i.e. mass loss rate equal to zero). However, end effects were eliminated by defining the end of Regime II as the time taken to reach 90% mass loss. The duration of Regime II decreases from 37 to 21 min over the heat flux range studied.

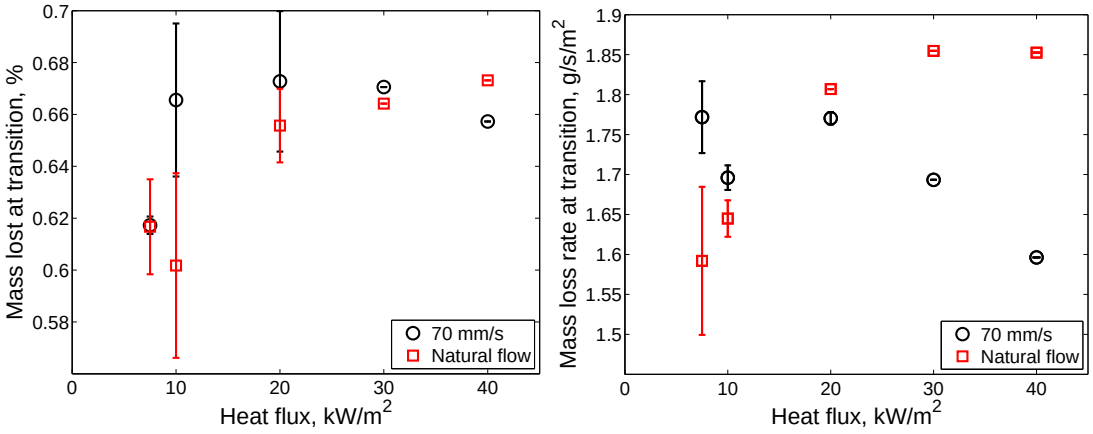

(a) (b)

Figure 5.10. (a) The percent mass lost at the transition from Regime I to Regime II and (b) the mass loss rate at transition.

Figure 5.12 shows the average mass loss rates in the two regimes. In Regime I, the average mass loss rate is strongly dependent on the heat flux (as with the peak mass loss rate (Fig. 5.8)), increasing from around 2.5 to 6 $g \cdot s^{-1} \cdot m^{-2}$. However, there is a weak dependence on the nature of the flow as explained previously. At low heat fluxes, the availability of oxygen results in higher average mass loss rates as the oxidative reactions can occur at a higher rate, but at high heat fluxes when the applied heat flux dominates, the flow acts to cool the sample, slightly reducing the average mass loss rate. Regime II is not dependent on the heat flux, as shown by the constant average mass loss rate of approximately 1 $g \cdot s^{-1} \cdot m^{-2}$.

In-depth temperatures

Temperature measurements were made under heat fluxes of 10 and 20 $kW \cdot m^{-2}$ and flows of 70 $mm \cdot s^{-1}$ of air and nitrogen.

The temperatures and mass loss rate for a test at 10 $kW \cdot m^{-2}$ are shown in Fig. 5.13. These temperature ranges are in agreement with those found by Rein et al. [8] for natural smoulder. At the beginning of the experiment (Regime I) it is observed that the temperatures throughout the sample are increasing. This corresponds to the propagation of the pyrolysis front through the sample. The temperatures at the surface and depths 10 and 20 mm begin reach maximum values of 525, 590 and 600°C respectively. After reaching a maximum these decrease as the sample is consumed and the thermo-

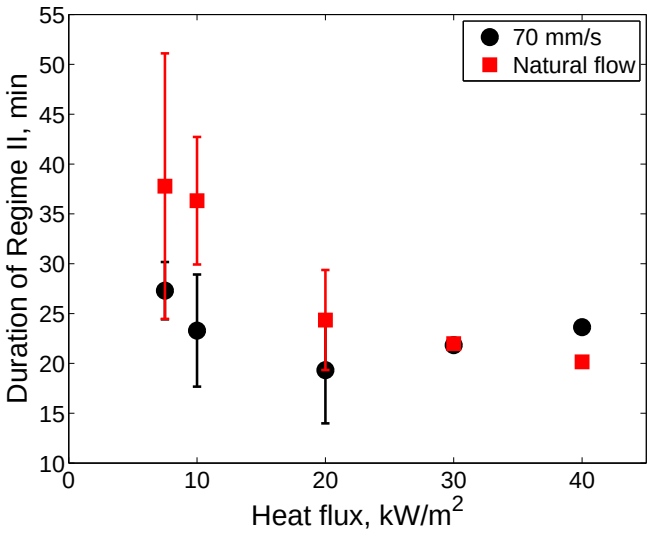

Figure 5.11. The duration of Regime II for natural and forced flow of 70 mm·s^{-1} at the heat fluxes studied.

couples are exposed. The temperature at 30 mm increases to around 500°C prior to the transition from Regime I to Regime II. During Regime II, it remains at an elevated temperature reaching 550°C after 45 min. This indicates that there is sustained heat generation at this location. This is in agreement with the observation that in Regime II the char oxidation reaction occurs on the bottom face of the sample.

Figure 5.14 compares the reactions at 10 kW·m^{-2} under 70 mm·s^{-1} of air and nitrogen. The temperatures observed under nitrogen are lower than those observed in air. This is because under nitrogen, only endothermic pyrolysis and no exothermic oxidation reactions occur and heat must be transferred from the lamps through the solid to drive the reaction.

The mass loss rate under nitrogen is approximately 60% lower than for oxidative atmospheres (Fig. 5.14b). This is evidenced by a peak mass loss rate of 3 g·s^{-1}·m^{-2} for nitrogen compared to 6 g·s^{-1}·m^{-2} for air. This is because the char which is formed by pyrolysis cannot be oxidized to form gaseous products. It can be concluded therefore that approximately half of the mass loss rate is due to the oxidative reactions in Regime I. In Regime II, the mass loss rate in air changes from 1.8 to 0.8 g·s^{-1}·m^{-2} during the same time the mass loss rate under nitrogen decreases from 1.5 g·s^{-1}·m^{-2} to 0.5 g·s^{-1}·m^{-2}. One key difference observed is that under air in Regime I there is a second local peak in mass loss rate after the first. This may be a result of oxidative reactions; however,

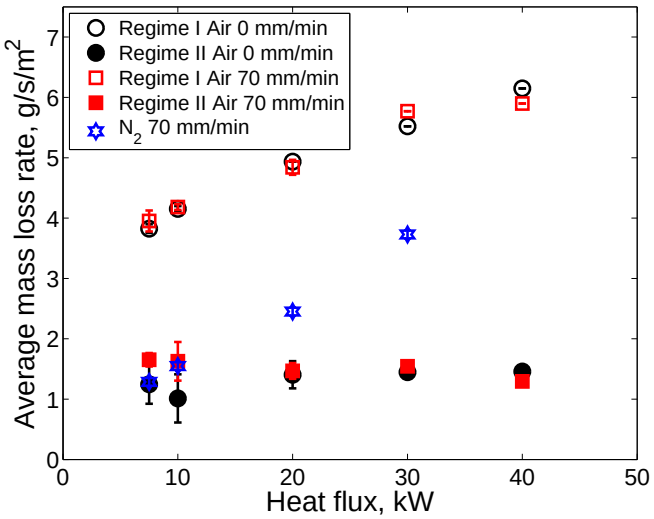

Figure 5.12. The average mass loss rates for Regime I and Regime II.

there are insufficient data to conclude. These observations are consistent at heat fluxes 7.5 and 20 kW·m^{-2}.

5.3.6 Effect of flow

Oxidizer flux to the reaction zone is known to influence the propagation of a smouldering front [3]. The effect of the flow on Regimes I and II is shown in Fig. 5.15 for samples exposed to a heat flux of 10 kW·m^{-2}. This was chosen because the effect of the flow should be more obvious at low heat fluxes.

The peak mass loss rate in Regime I (Fig. 5.15a) is independent of flow. This suggests that Regime I is dominated by the heat insult from the lamps. Regime II also shows constant peak mass loss rate with flow at 1.9 g·s^{-1}·m^{-2}.

The onset of Regimes I and II (defined as the time to peak mass loss rate) is independent of flow at around 4.5 and 19 min for Regimes I and II respectively (Fig. 5.15b). This suggests that the onset of each Regime is controlled by the heat flux applied to the sample. This is in agreement with the conclusions drawn earlier.

The duration of Regime I (Fig. 5.15c) does not change with the flow. However, the duration of Regime II is strongly dependent, reducing from 34 to 13 min as the flow is increased from 0 to 300 mm·s^{-1}. This reinforces the earlier observations that flow of oxidizer affects Regime II.

The average mass loss rate in the two regimes is shown in Fig. 5.15d. Regime

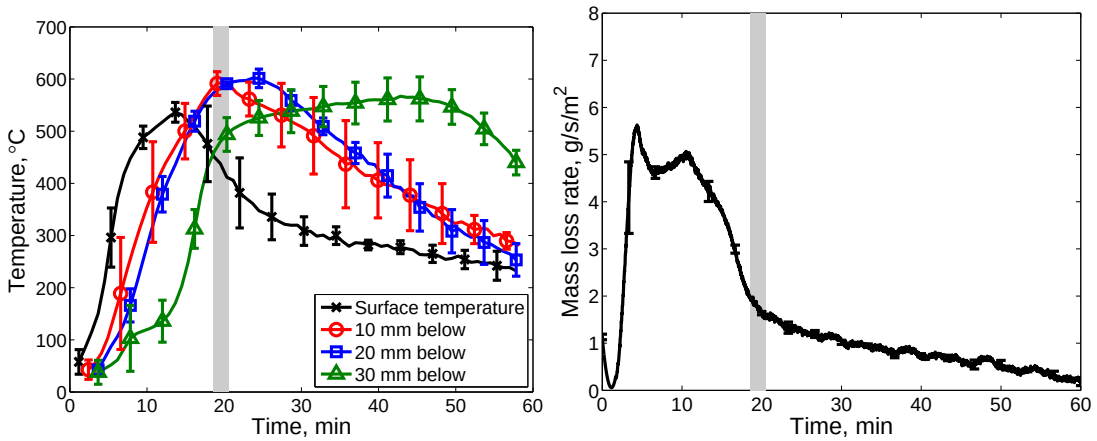

(a) (b)

Figure 5.13. (a) Temperatures at the surface and at depths of 10 and 20 mm and (b) mass loss rate at 10 kW·m^{-2} and flow of 70 mm·s^{-1} of air. The shaded area corresponds to the transition from Regime I to Regime II. Error bars show the standard deviation from 3 experiments.

I is again shown to be weakly influenced by the flow, with mass loss rates around 3.6–3.9 g·s^{-1}·m^{-2}, while Regime II shows an increasing trend in the mass loss rate from 0.9–1.5 g·s^{-1}·m^{-2} over the range of flows studied. This also confirms that Regime II is dependent on the flow, whereas Regime I is dependent on the heat flux applied.

5.3.7 CO and CO_2 emissions

To verify the observations using mass loss rate and temperature data, Fig. 5.16 shows the yields of CO and CO_2 as a function of time. Yields are calculated by dividing the mass flux of a species by the mass loss rate per unit area. This gives a result in kg of emission per kg of peat consumed. At the beginning of the experiment, the yields of CO and CO_2 are low, on the order of 0.2 and 0.5 kg·kg^{-1} respectively. They both then increase to approximately 0.6 to 2 kg·kg^{-1}. This increase corresponds to the time of the transition from Regime I to II and shows that the chemistry in these two regimes is different.

5.4 Conclusions

The smouldering behaviour of sphagnum moss peat has been studied under a range of burning conditions in small-scale laboratory experiments. This is of interest in

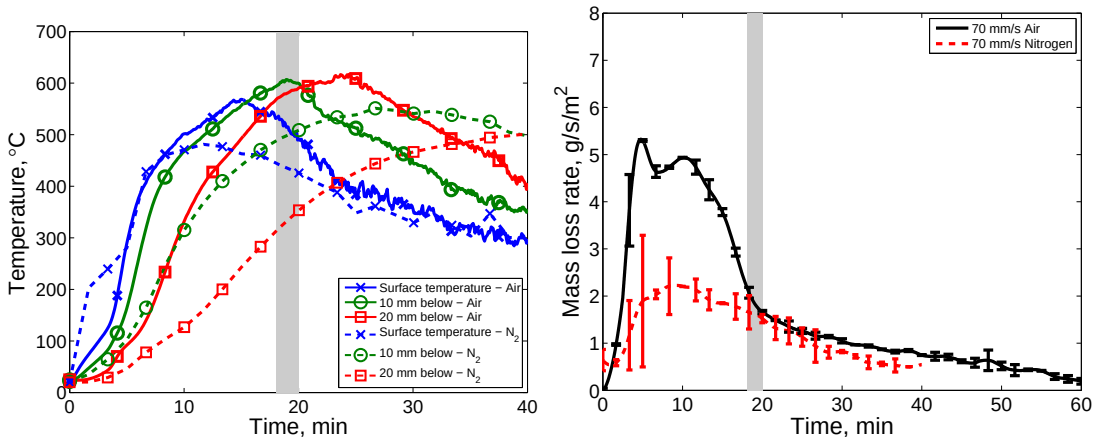

(a) (b)

Figure 5.14. (a) Temperatures at the surface and depths of 10 and 20 mm and (b) mass loss rate for a sample of peat exposed to 10 kW·m^{-2} and subject to a flow of 100 l·min^{-1} of nitrogen.

understanding the dynamics of peat fires, which are a significant threat to tropical and boreal ecosystems worldwide. These results provide a significant step in understanding the smouldering behaviour of natural fuels.

Two smouldering regimes were observed using both mass loss data and independently with analysis of the combustion gases. These regimes were found to be controlled by the incident heat flux and flow of oxidizer respectively. The regimes were found both when an external heat flux was applied and when the smoulder was allowed to progress unassisted. The mass loss behaviour is typical of charring materials corresponding to the formation of a char layer on the surface of the sample before the smoulder continues in depth. Peak temperatures are of the order of 600°C, which is in agreement with previous work on smouldering peat [8, 10], and other than at the surface, do not depend on the external heat flux.

In Regime I, the mass loss rate is controlled by the applied heat flux, suggesting that pyrolysis reactions dominate. This results in the production of char which, in the presence of oxygen, undergoes exothermic reaction. If a strong heat flux is applied, the pyrolysis reactions happen much faster than the oxidative reactions and therefore the former dominate the behaviour. In Regime II, a char layer has formed which insulates the reaction zone. This reduces the rate of the pyrolysis reaction and allows the oxidation to occur relatively faster. In this regime, we see a greater influence of the

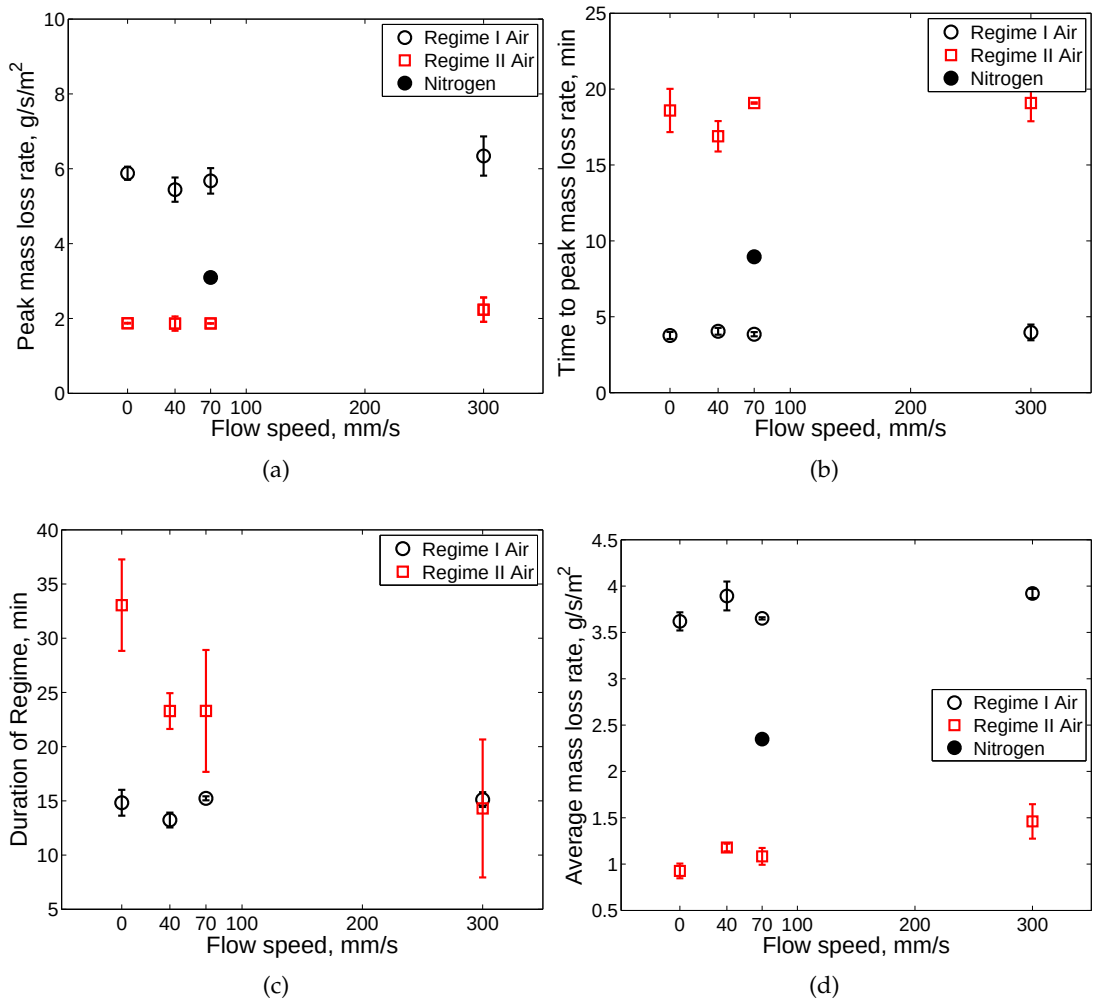

Figure 5.15. The effect of flow on (a) peak mass loss rate in Regime I, (b) onset of Regime I, (c) the duration of Regimes I and II and (d) the average mass loss rates in Regimes I and II under air 10 kW·m^{-2}. Experiments under nitrogen are shown with solid symbols for comparison.

flow speed on the reaction dynamics, as the available oxygen reacts with excess char formed in Regime I, as well as promoting the propagation of the smouldering front.

These results are significant in understanding the smouldering behaviour of organic materials in the natural environment, which is being recognized as a significant contributor to the global carbon cycle, as well as resulting in significant damage to ecosystems.

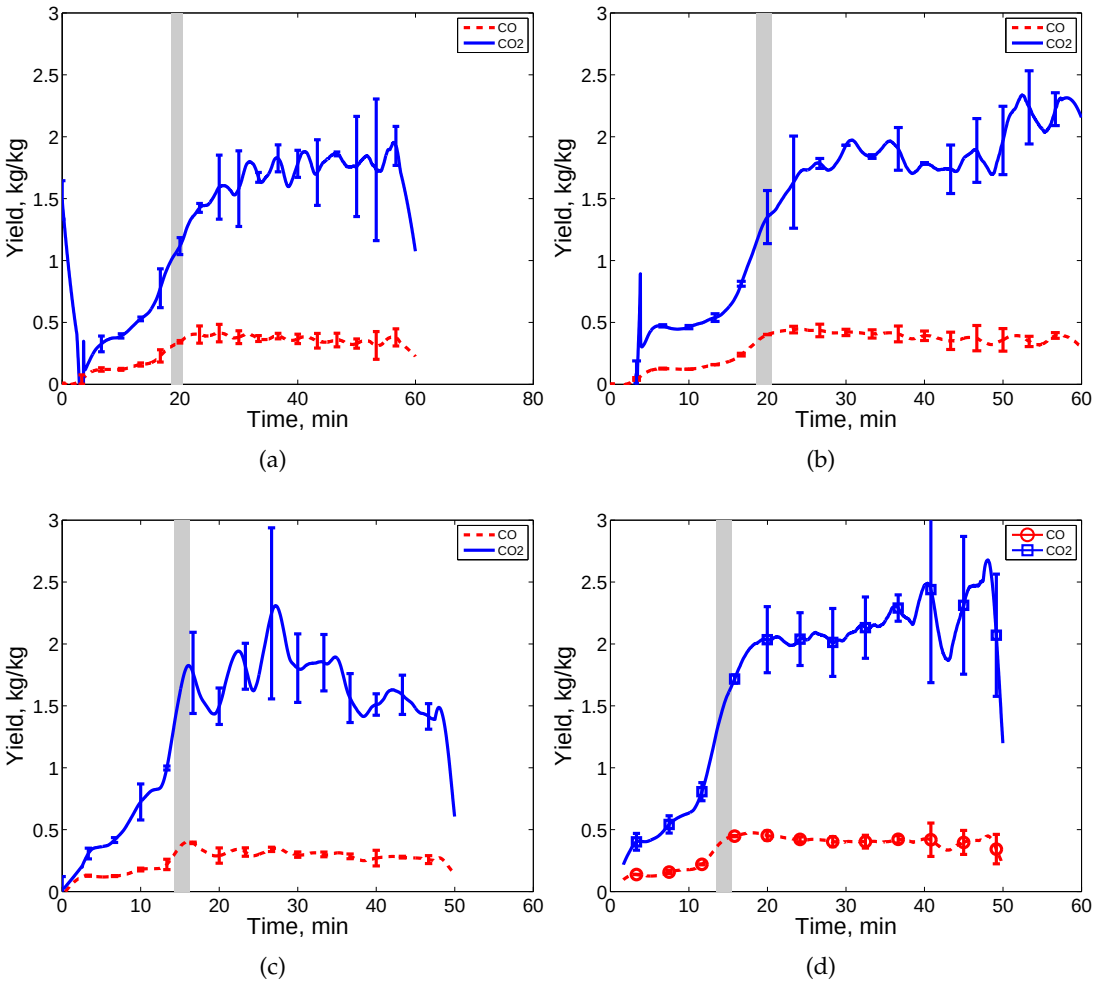

Figure 5.16. Yields of CO and CO_2 for (a) 10 kW·m^{-2} and 0 l·min^{-1}, (b) 10 kW·m^{-2} and 100 l·min^{-1}, (c) 20 kW·m^{-2} and 0 l·min^{-1}, (d) 20 kW·m^{-2} and 100 l·min^{-1}.

References

[1] W. H. Frandsen. Heat evolved from smoldering peat. *International Journal of Wildland Fire*, 1(3):197–204, 1991. doi: 10.1071/WF9910197.

[2] K. N. Palmer. Smouldering combustion in dusts and firbous materials. *Combustion and Flame*, 1:129–154, 1957.

[3] T. J. Ohlemiller. *SFPE Fire Protection Handbook*, chapter 2-10: Smouldering Combustion, pages 2–201–2–210. National Fire Protection Association, Quincy, MA 02269, 3rd edition, 2002.

[4] G. Rein. Smouldering combustion phenomena in science and technology. *International Review of Chemical Engineering*, 1:3–18, 2009. URL hdl.handle.net/1842/2678.

[5] S. E. Page, F. Siegert, J. O. Rieley, H.-D. V. Boehm, A. Jaya, and S. Limin. The amount of carbon released from peat and forest fires in Indonesia during 1997. *Nature*, 420:61–65, 2002. doi: 10.1038/nature01131.

[6] W. H. Frandsen. The influence of moisture and mineral soil on the combustion limits of smouldering forest duff. *Canadian Journal of Forest Research*, 17:1540–1544, 1987.

[7] W. H. Frandsen. Ignition probability of organic soils. *Canadian Journal of Forest Research*, 27:1471–1477, 1997.

[8] G. Rein, N. Cleaver, C. Ashton, P. Pironi, and J. L. Torero. The severity of smouldering peat fires and damage to the forest soil. *Catena*, 74(3):304–309, 2008. doi: 10.1016/j.catena.2008.05.008.

[9] G. Rein, S. Cohen, and A. Simeoni. Carbon emissions from smouldering peat in shallow and strong fronts. *Proceedings of the Combustion Institute*, 32(2):2489–2496, 2009. doi: 10.1016/j.proci.2008.07.008.

[10] C. M. Belcher, J. M. Yearsley, R. M. Hadden, J. C. McElwain, and G. Rein. Baseline intrinsic flammability of Earth's ecosystems estimated from paleoatmospheric oxygen over the past 350 million years. *Proceedings of the National Academy of Sciences*, 107(52):22448–22453, 2010. doi: 10.1073/pnas.1011974107.

[11] T. J. Christian, B. Kleiss, R. J. Yokelson, R. Holzinger, P. J. Crutzen, W. M. Hao, B. H. Saharjo, and D. E. Ward. Comprehensive laboratory measurements of biomass-burning emissions: 1. emissions from Indonesian, African, and other fuels. *Journal of Geophysical Research*, 108(D23):4719, 2003. doi: 10.1029/2003JD003704.

[12] A. Bar Ilan, G. Rein, D. C. Walther, A. C. Fernandez Pello, J. L. Torero, and D. L.

Urban. The effect of buoyancy on opposed smoldering. *Combustion Science and Technology*, 176(12):2027–2055, 2004. doi: 10.1080/00102200490514822.

[13] D. C. Walther, R. A. Anthenien, and A. C. Fernandez Pello. Smolder ignition of polyurethane foam: effect of oxygen concentration. *Fire Safety Journal*, 34(4): 343–359, 2000. doi: 10.1016/S0379-7112(00)00007-2.

[14] J. L. Torero and A. C. Fernandez Pello. Forward smolder of polyurethane foam in a forced air flow. *Combustion and Flame*, 106(1-2):89–109, 1996. doi: 10.1016/0010-2180(95)00245-6.

[15] T. J. Ohlemiller and D. A. Lucca. An experimental comparison of forward and reverse smolder propagation in permeable fuel beds. *Combustion and Flame*, 54 (1-3):131 – 147, 1983. doi: 10.1016/0010-2180(83)90027-5.

[16] ASTM International. ASTM E2058 -09, Standard test methods for measurement of synthetic polymer material flammability using a Fire Propagation Apparatus (FPA), 2009.

[17] C. F. Schemel, A. Simeoni, H. Biteau, J. D. Rivera, and J. L. Torero. A calorimetric study of wildland fuels. *Experimental Thermal and Fluid Science*, 32(7):1381–1389, 2008. doi: 10.1016/j.expthermflusci.2007.11.011.

[18] J. L. Torero. *Buoyancy Effects on Smoldering of Polyurethane Foam*. PhD thesis, University of California, Berkeley, 1992. URL www.era.lib.ed.ac.uk/handle/1842/2134.

6

Carbon emissions from smouldering peat fires under controlled conditions

Summary

Smouldering peat fires are a significant threat to the natural environment. These fires result in the release of large quantities of greenhouse gases to the environment, consume large quantities of biomass and damage peatland ecosystems. A series of small-scale fire calorimetry experiments has been carried out to measure the carbon emissions from smouldering and flaming peat under known burning conditions. Mass loss, temperature and CO and CO_2 concentrations, fluxes and yields are measured and used to study the smoulder dynamics and emissions. During smouldering, two combustion regimes are observed; the first is peat smouldering and is characterized by high mass loss rate and increasing emissions and temperatures. During this regime, the pyrolysis and oxidation fronts are propagating through the peat. The peat is pyrolysed to form a carbon-rich char. The pyrolysis front propagates through the sample faster than the oxidation front and eventually consumes all the peat. After this time, only char oxidation reactions can occur. This oxidation corresponds to the second observed burning regime. Peak mass fluxes in the range 0.8–1.3 $g \cdot s^{-1} \cdot m^{-2}$ and 2.5–3.6 $g \cdot s^{-1} \cdot m^{-2}$ are reported for CO and CO_2 respectively. The yields (emission factors) of CO and CO_2 are 0.12–0.18 and 0.25–0.6 $kg \cdot kg^{-1}$ during the peat smouldering regime and 0.4 and 2 $kg \cdot kg^{-1}$ during the char oxidation regime. A CO/CO_2 ratio of 0.3 is found in during peat smouldering, decreasing to 0.2 in the char oxidation regime. Comparison

is made with experiments in which flaming combustion was initiated. It is found that the flux of CO_2 increases 3.8 times and CO decreases 0.75 times compared to the corresponding time during smouldering, showing that these modes of combustion are driven by different chemical processes. The CO/CO_2 ratio for flaming is less than 0.1. The smouldering fire contributes more significantly to the CO and CO_2 emissions releasing 97% and 85% of the these emissions respectively. Characterizing the emissions as a function of the burning dynamics is a significant step forward from previous work and allows the results to be applied more generally to real fires, which occur under similar conditions to those tested here.

6.1 Introduction

Fires in peat lands are being increasingly recognized as a serious threat to the environment. Peat is a naturally occurring material formed by the anaerobic decay of organic matter. When ignited, peat fires typically propagate at low speeds and can persist for extended periods of time in the subsurface [1]. Page et al. [2] estimated that 0.8–2.6 Pg of carbon was released to the atmosphere during the 1997 peat and forest fires in Indonesia (13–40% of global, annual carbon emissions). It was also estimated that the peat fires accounted for 20% of the area but resulted in 94% of the total emissions. Poulter et al. [3] studied a 1985 peat fire in North Carolina, USA in which they estimated a total release of 1–3.8 Tg of carbon over a period of 15 days. They estimate that 0.32 Pg of carbon is released annually due to fires in temperate peat lands. More recently, there have been significant smouldering peat fires in North Carolina, USA (2008) [4] and Russia (2010) [5] . Historically, peat fires have been reported in tropical and boreal peat regions, but more recently fires have been observed in the arctic tundra [6, 7] indicating that this is an increasing global problem.

The smoulder behaviour of peat has previously been studied in the laboratory by Fransden [8–10]. Using oxygen consumption calorimetry [11], the heat of combustion of smouldering Canadian sphagnum moss peat was found to be $14.2 \pm 4.5\%$ $MJ \cdot kg^{-1}$; however, this measurement technique may not necessarily be applicable to smouldering combustion. Fransden [8, 10] studied the ignition probability as a function

of moisture and organic content and bulk density. Ignition was found to be likely at moisture contents lower than 90% for inorganic content of 35% and there existed a linear relationship between the organic and moisture contents of peat under which it could sustain smouldering combustion. Peat with higher organic content was found to burn at higher moisture levels. This is due to the increased heat released per unit mass which can overcome the endothermic evaporation of water.

Rein et al. [12] studied the effect of moisture content on ignition and spread of smouldering boreal peat in small-scale laboratory experiments. They found that ignition would only occur below a critical moisture content of 125% on a dry basis with an inert fraction of 8±2%. Temperatures in excess of 300°C for periods of over one hour and mass loss of 90% after combustion were reported.

The effect of oxygen concentration on the propagation of peat fires was studied by Belcher et al. [13]. Using the same experimental set-up as Rein et al. [12], ignition of samples of sphagnum moss peat with 15% moisture was attempted under natural convection in atmospheres with oxygen concentrations of 13 to 21% by volume. The probability of ignition was shown to increase with increasing oxygen concentration and it was found that smoulder would not propagate at oxygen concentrations lower than 16%.

The emissions from combustion of Indonesian peat with 30% moisture content (dry base) were studied by Christian et al. [14]. A CO/CO_2 ratio of 0.04 $kg \cdot kg^{-1}$ was reported but the smouldering dynamics were not quantified. Emissions from mg-sized samples of tropical peat heated to 480°C in a sealed vessel in the absence of oxygen are reported by Muraleedharan et al. [15]. CO_2, CO and CH_4 were reprted as the most abundant species with yields of 0.185, 0.037 and 0.005 $kg \cdot kg^{-1}$ respectively. These experiments do not capture the real smoulder process as the sealed vessel prevents oxidative reactions occurring.

Rein et al. [16] studied emissions from smouldering boreal peat using the cone calorimeter [17] (a small-scale combustion calorimeter). Moisture contents of 80 to 600% were exposed to heat fluxes between 30 and 70 $kW \cdot m^{-2}$ for the duration of the experiment under natural flow conditions. The yield of CO and CO_2 on a dry base were found to be 0.17 and 0.42 $kg \cdot kg^{-1}$ respectively, resulting in a CO/CO_2 ratio of

0.3–0.6 $kg \cdot kg^{-1}$.

In this work, the emissions from peat fires under controlled laboratory conditions are studied. This is a novel contribution as it allows quantification of the emissions in terms of the reaction dynamics. In this paper, we use the FM Global Fire Propagation Apparatus (FPA) [18] which allows control of both the flow around a sample and the intensity of the combustion. Mass loss rate, temperature and emissions data are used to describe the smouldering process.

6.1.1 Peat combustion

The high carbon content of peat means that it will readily undergo combustion if heated in the presence of oxygen; this can be either flaming or smouldering combustion. As with any fuel, when heated, peat will initially undergo pyrolysis. This is an endothermic reaction which breaks down the organic molecules to form a solid, carbon-rich char and gaseous pyrolysate (typically high in short-chained hydrocarbons, PAHs and partially oxidized species) [19]. If the pyrolysate vapours are evolved in sufficient concentration in the presence of an ignition source then flaming combustion will be initiated. However if the flux of pyrolysate is low, smouldering combustion will occur. The chemical and physical processes involved in flaming and smouldering combustion differ significantly.

Flaming is a homogeneous, gas phase reaction in which gas evolved from the pyrolysis of the fuel (pyrolysate) reacts with oxygen from the air in the gas phase [19]. Smouldering is a slow, low temperature, heterogeneous oxidation reaction that occurs when oxygen attacks the surface of a solid fuel [1, 20, 21]. The timescales of these modes of combustion are significantly different. Flames spread over the surface of a fuel at a speed typically on the order of 1 $mm \cdot s^{-1}$ [19] and will consume thin fuels resulting in typical gas-phase temperatures in the range 900–1500°C. Smouldering can persist for days, weeks, months and even years [12] as it propagates through and into a fuel. In some extreme cases, smouldering fires have been observed to burn in natural fuels for decades [22]. Typical temperatures for smouldering peat range from 500 to 600°C and propagation rates are on the order of 1–10 $cm \cdot h^{-1}$ [1, 8]. The long duration means that smouldering contributes significantly to the damage to the ecosystem [12]

as well as large release of carbon and aerosol emissions (see e.g. Page et al. [2]).

6.2 Experimental set-up

The FPA is a small-scale fire calorimeter used to determine the combustion characteristics of materials [18]. A schematic of the apparatus is shown in Fig. 6.1. Four halogen lamps provide a uniform radiative heat flux across the surface of a sample of diameter 125 mm and depth 30 mm. The environment in which the combustion occurs can be controlled with respect to the velocity and composition of the flow through and around the sample. The mass loss, temperatures in the sample, flow and composition of exhaust gases are measured and used to characterize the burning behaviour under given conditions.

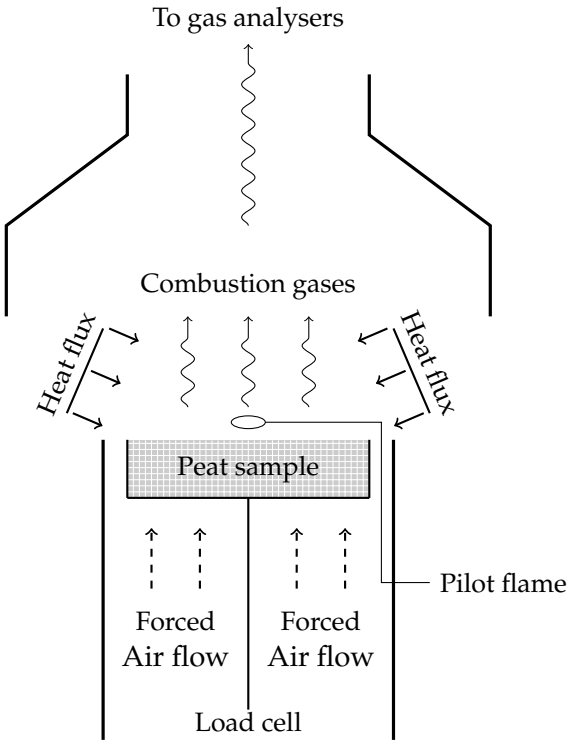

Figure 6.1. Schematic of the FPA.

Sphagnum moss peat is used in these experiments as a proxy for naturally occurring peat. This peat is commercially available in the UK (Shamrock Irish Moss Peat). Using this peat results in a more repeatable sample compared to naturally occurring peat as it has a homogeneous structure and can be sourced consistently. This is the same peat as studied previously by Belcher et al. [13]. The peat is oven-dried at 80°C for at least 48 h

and allowed to cool to ambient temperature in sealed polyethelene bags for at least 3 h prior to testing to ensure all moisture has been removed. The bulk density of the peat after drying is 220 $kg \cdot m^{-3}$ and the moisture content of the samples prior to testing is $0.6 \pm 0.3\%$ (dry basis). Using dry peat provides a more repeatable sample and allows a simplified analysis to be undertaken as it removes the water evaporation mechanism [16] while producing a conservative estimate of burning rates in natural environments. Samples of peat weighing approximately 80 g are used. The peat is held in a sample holder constructed from 2 mm thick steel mesh with porosity of 26%. This allows air to flow through the sample (see Schemel et al. [23]) and allows the effect of flow on the smoulder reaction to be studied. This has not been included in previous work, e.g. Rein et al. [16].

Experiments were undertaken at heat fluxes in the range 7.5–40 $kW \cdot m^{-2}$ and air flows up to 300 $mm \cdot s^{-1}$ (see Section 6.2.1). The heat flux received by the sample is uniform with maximum deviations at the edges of the sample of less than 10%. Two types of heat flux exposure were studied: constant exposure and 10 min exposure.

The peat was ignited by exposure to a radiant heat flux on the downstream surface of the sample (with respect to the oxidizer flow). The heat flux acts as the ignition source and mimics the heat released by the combustion of surrounding peat in a real fire. Higher heat fluxes represent a more intense fire than lower heat fluxes. This will result in heating and pyrolysis of the peat generating pyrolysate gas and leaving behind a layer of solid char. If a small pilot flame is introduced above the sample, flaming combustion may be initiated if the pyrolysate is of sufficient concentration. Smouldering was initiated on the upstream side of the sample and was followed by a quasi-one dimensional downward propagation. This is a simplification of the real, three dimensional propagation of natural fires. Experiments were terminated when the sample mass became constant and the concentrations of CO and CO_2 had returned to ambient levels.

6.2.1 Flow characterization

The flow through the porous fuel is known to affect the smoulder dynamics [24]. Therefore, it is necessary to define the flow field around and through the sample. Flow

speeds corresponding to volumetric flow rates of 50, 100 and 200 l·min^{-1} around the sample are measured. The upstream flow (i.e. before impingement on the sample), was characterized by measuring the flow speed in five upstream locations using a hot wire anemometer. Measurements were taken at the centre of the flow duct, and at points 70 and 140 mm along the radius at 90° intervals in the absence of the sample and applied heat flux. With a sample in place (and no heat flux), the flow was measured at four points between the edge of the sample holder and edge of the flow duct. The flow speed through the sample could then be calculated. The upstream flow speeds and calculated flow speeds through the sample are given in Table 6.1.

Before impingement, average upstream speeds range from 40 to 400 mm·s^{-1}. The velocity at 50 l·min^{-1} was lower than the sensitivity of the device, but a calculation suggests a value of the order 40 mm·s^{-1}. The flow around the sample was considerably higher than the upstream flow and ranged from 120±30 to 830±200 mm·s^{-1}. This is because the pressure drop through the peat results in most flow going around the sample and only a small fraction through the sample. The flow through the sample was calculated by a mass balance of the flow around and upstream of the sample. These flows are also shown in Table 6.1. Flow above the sample of 130 mm·s^{-1} was measured at a flow rate of 200 l·min^{-1}. This is within the calculated range, showing that the calculation yields reliable results. The exact flow field will be altered by the buoyant flow induced by the heating of the sample; therefore reference is made to the upstream velocity when discussing the experimental conditions.

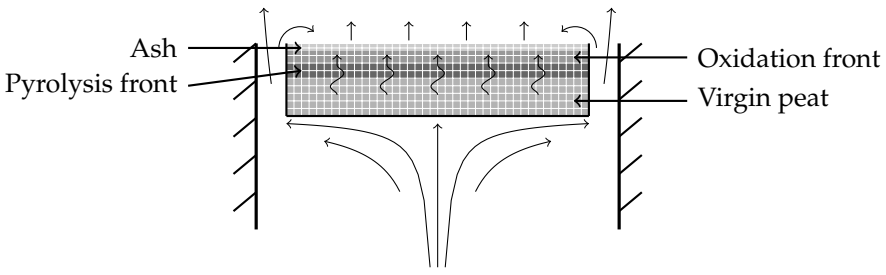

Figure 6.2. Schematic of the flow field around and through a sample of peat in the FPA.

Table 6.1. Range of upstream flow speed and calculated flow speed through the sample for the volumetric flow rates studied. Flow of 130 mm·s^{-1} was measured above the sample in the case of the 200 l·min^{-1} flow, suggesting that the calculations are reliable.

Flow rate, l·min^{-1}	Upstream speed, mm·s^{-1} Measured range	Flow through sample, mm·s^{-1} Calculated range
50	40	0–15
100	20–150	50–90
200	130–400	120–300

6.2.2 Test matrix

Figure 6.2 shows the test matrix for the experiments carried out in this work. Thirty-eight experiments were carried out with constant exposure to the heat flux, twenty-six experiments with 10 min exposure and thirty-three with constant exposure and the pilot flame present. Experiments were repeated to ensure consistency of results and provide estimates of the error. In total, results from 96 experiments are reported.

Table 6.2. Test matrix showing the heat flux/flow conditions under which the experiments were conducted. The experiments are grouped into three sets: continuous exposure to the heat flux, 10 min exposure to the heat flux and constant exposure to the heat flux with a pilot flame present.

Flow speed mm·s^{-1}	Continuous heat flux					10 min exposure					Pilot flame				
300	1	2	2	1	2	-	-	-	-	-	1	1	1	1	1
70	3	6	2	1	1	3	2	6	1	-	1	3	5	1	1
40	1	4	1	1	1	-	2	-	-	-	1	1	2	1	1
Natural flow	2	3	2	1	1	1	4	4	2	1	1	4	4	1	1
Heat flux, kW·m^{-2}	7.5	10	20	30	40	7.5	10	20	30	40	7.5	10	20	30	40

6.3 Smouldering results and discussion

6.3.1 Overview

Figure 6.3 shows the data from three experiments where samples were exposed to continuous heat fluxes of 7.5, 10 and 20 kW·m^{-2} with a constant air flow of 70 mm·s^{-1}. Figure 6.3a shows the normalized sample mass as a function of time for the three experiments. This shows that as the heat flux is increased, time to the onset of significant mass loss decreases. It also shows a consistent transition from a period of high mass

loss rate at the beginning of the experiment to lower mass loss rate at the end of the experiment. The transition is indicated by the shaded regions.

The transition in mass loss rates is shown more clearly in Fig. 6.3b. The transition is from a period of high mass loss rate during the initial phase of the reaction to the period of lower mass loss rate and is shown by the shaded region. The transition is found by locating the maximum of the second derivative of the mass loss rate curve. For a heat flux of 7.5 $kW \cdot m^{-2}$, the mass loss rate increases rapidly to approximately 5 $g \cdot s^{-1} \cdot m^{-2}$ at 5 min. After this there is a period of roughly 10 min where the mass loss rate remains constant before it starts to decline. After a sharp decline to approximately 2 $g \cdot s^{-1} \cdot m^{-2}$ over 7 min, the transition in the mass loss rate is observed and it gradually decreases to zero during the following 38 min. Similar trends are seen for exposure to 10 and 20 $kW \cdot m^{-2}$; however, the peak mass loss rate at these heat fluxes are 6 and 7.5 $g \cdot s^{-1} \cdot m^{-2}$, reached in 2 and 4 min respectively.

Surface temperatures (Fig. 6.3c) show that the peak temperature is independent of applied heat flux at around 530°C, however the time to reach this peak decreases from 14 to 9 min for heat fluxes of 10 and 20 $kW \cdot m^{-2}$. The transitions seen in the mass loss rate occur just after the peak in surface temperature.

The mass flux of CO and CO_2 for the experiments is shown in Fig. 6.3d. As the heat flux is increased, these peak earlier with CO reaching a flux of 0.7 $g \cdot s^{-1} \cdot m^{-2}$ and CO_2 2.5 $g \cdot s^{-1} \cdot m^{-2}$. The transition corresponds to a time when the emissions begin to decay. The peak CO_2 flux is approximately 3.5 times higher than the peak CO flux and there is a slight increase in the peak fluxes with increasing applied heat flux.

From these data, two burning regimes are consistently observed across a wide range of conditions. The first is the period of high mass loss rate and increasing emissions flux and temperature at the beginning of the experiment corresponding to peat smouldering. The second is the period of lower mass loss rate and decaying emissions and temperatures during the latter part of the experiment, when char oxidation dominates the combustion dynamics. A detailed study of these regimes is given in Chapter 5. The first regime corresponds to a period of peat smouldering. During this period, the pyrolysis front is driven through the sample by the heat liberated from the oxidation reactions (assisted by the applied heat flux). This converts the peat to carbon-rich char

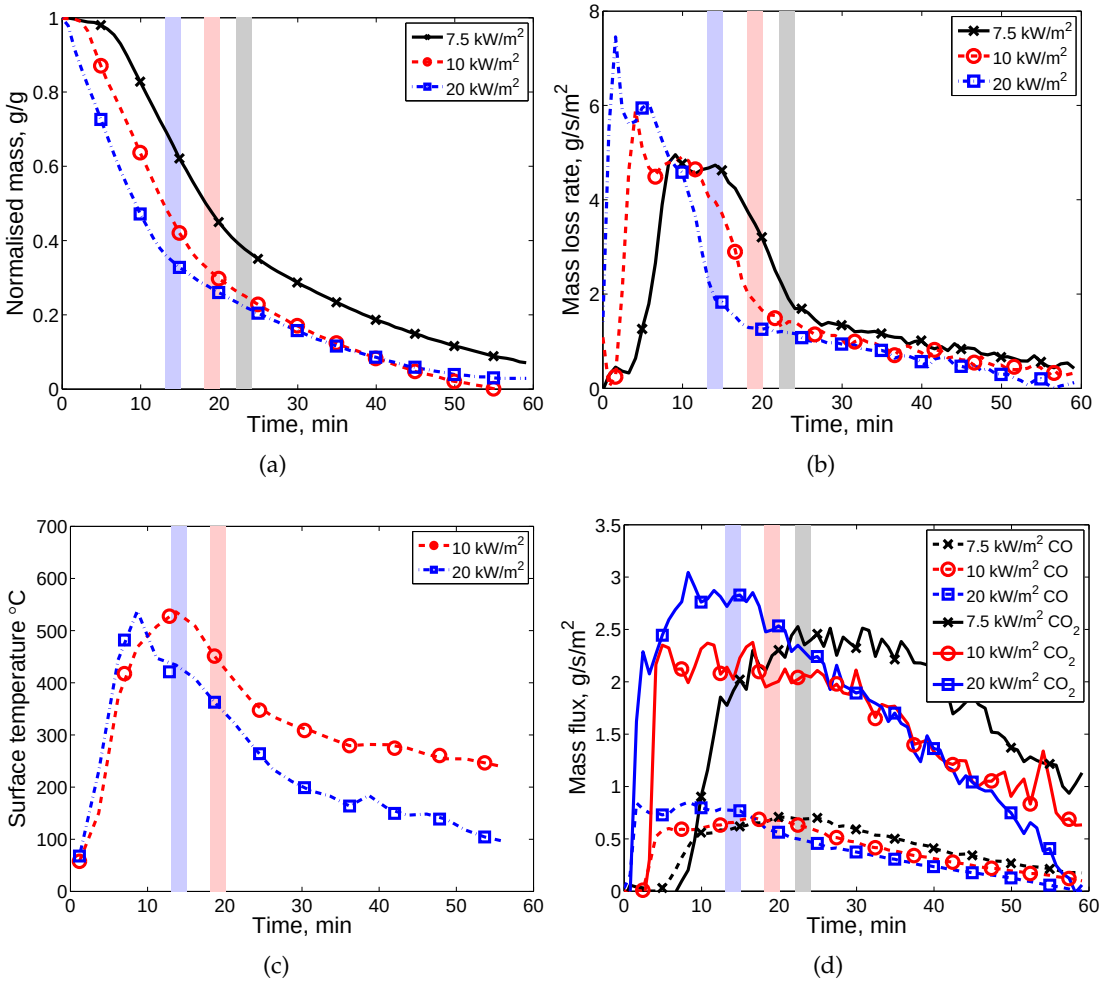

Figure 6.3. (a) Normalized mass, (b) mass loss rates, (c) surface temperatures and (d) CO and CO_2 flux as a function of time for experiments at 7.5, 10 and 20 kW·m^{-2} showing two distinct burning regimes, the transition between which is highlighted by the shaded regions.

and pyrolysate. After all the peat has been converted to char, the pyrolysis reaction stops. This is the end of the first regime. In the second regime the char undergoes oxidative reactions to form gaseous products and ash.

6.3.2 Duration of the applied heat flux

Figure 6.4a shows the mass loss rate for exposure of a sample to a heat flux of 10 kW·m^{-2} for 10 min compared to an experiment where the sample is exposed to the heat flux for the duration of the experiment. The 10 min exposure means that, once established, the reaction propagates unassisted. This results in slower propagation and therefore longer experimental duration. Initially, the mass loss rates follow the same profile, however

when the external heat flux is switched off after 10 min, the mass loss rate drops rapidly from 5 $g \cdot s^{-1} \cdot m^{-2}$ to 2.5 $g \cdot s^{-1} \cdot m^{-2}$ over 4 min. The mass loss rate increases again to that of the constant exposure experiment. Both mass loss rates then decrease as the reaction transitions to the second regime of char oxidation. The mass loss rates remain the same during this regime. There is no significant difference between the times to transition from peat smouldering to char oxidation between the 10 min and continuous exposure experiments

The mass flux of CO and CO_2 are shown in Fig. 6.4b. During exposure to the heat flux, the CO and CO_2 fluxes are the same. After the heat flux has been switched off, the fluxes of CO and CO_2 decease rapidly. After the transition to the period of char oxidation, the emissions from the 10 min exposure experiment are similar to those of the constant exposure experiment.

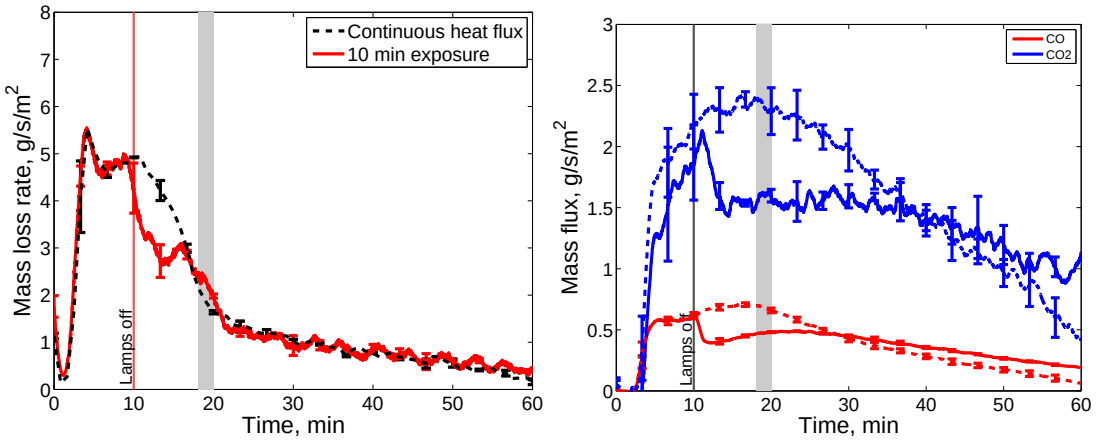

Figure 6.4. (a) Mass loss rates for heat flux of 10 $kW \cdot m^{-2}$ for 10 min showing the independence of the regimes on the applied heat flux and (b) Mass flux of CO and CO_2 for the same experiment. The shaded region corresponds to the transition from peat smouldering to char oxidation. The time when the lamps are switched off and the transition from peat smouldering to char oxidation are indicated.

6.3.3 Mass fluxes of CO and CO_2

The mass flux of CO and CO_2 are found by multiplying the volumetric flow rate of each species in the exhaust by its density at the temperature measured in the exhaust. The volumetric flows were calculated by multiplying the volume fraction of CO or

CO_2 measured in the exhaust gas by the measured volumetric flow in the exhaust duct. The mass flow is divided by the area of the sample to obtain a mass flux with units $g{\cdot}s^{-1}{\cdot}m^{-2}$.

The mass fluxes of CO and CO_2 as a function of time for experiments at 7.5 and 20 $kW{\cdot}m^{-2}$ are shown in Fig. 6.5. The general trend for both species is that the flux of both CO and CO_2 increase during the period of peat smouldering when the reaction front is growing and decrease during the period of char oxidation. As the applied heat flux is increased, the peak mass flux increases and the time to reach the peak reduces.

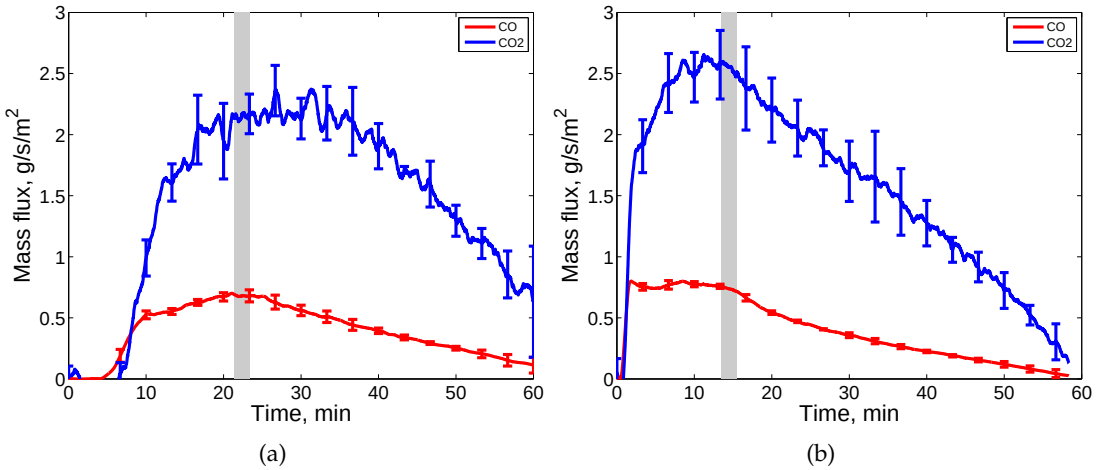

Figure 6.5. The mass flux of CO and CO_2 for experiments carried out at heat fluxes (a) 7.5 $kW{\cdot}m^{-2}$ and (b) 20 $kW{\cdot}m^{-2}$ with air flow of 70 $mm{\cdot}s^{-1}$. The shaded areas show the change from initial to in-depth burning.

These effects can be seen more clearly in Figs 6.6a and 6.6b which show the peak mass flux and time to the peak mass flux as a function of applied heat flux. As the heat flux is increased, the peak mass flux of CO and CO_2 increase from 0.8 to 1.3 and 2.5 to 3.6 $g{\cdot}s^{-1}{\cdot}m^{-2}$ respectively. The time to the peak flux of these decreases from 28 to 5 min for CO_2 and 32 to 2 min for CO as the heat flux is increased from 7.5 to 40 $kW{\cdot}m^{-2}$. The peak mass flux of CO is always reached before the peak mass flux of CO_2, indicating that CO is produced in higher quantities earlier in the smoulder process.

6.3.4 Yields

The yield of gaseous combustion product is defined as the mass flux of the species divided by the mass loss rate of sample. This gives a yield in units kg of species

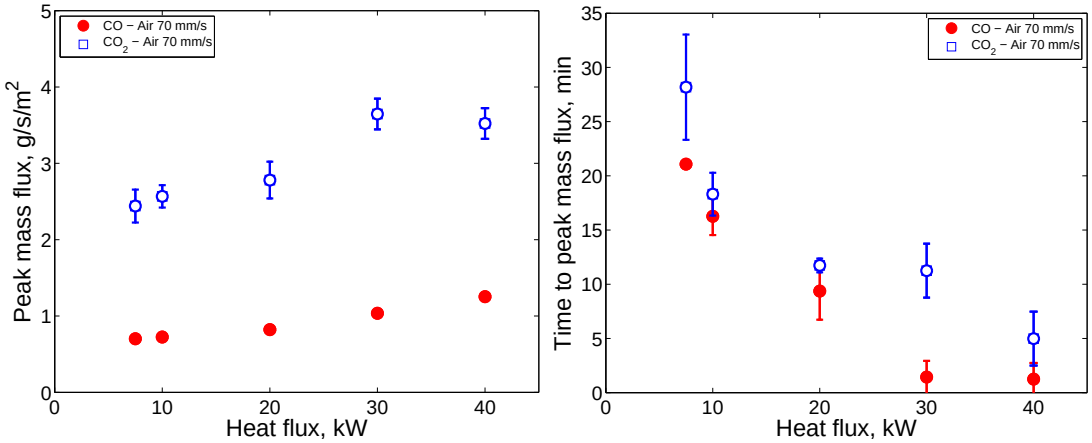

Figure 6.6. (a) The peak mass flux of CO and CO_2 and (b) the time to the peak mass flux as a function of the applied heat flux. If no error bar is shown, then the error is contained within the symbol.

produced per kg of peat consumed. This is sometimes referred to as the emission factor.

Yields of CO and CO_2 from experiments at 7.5 and 20 $kW \cdot m^{-2}$ are shown in Fig. 6.7. The shaded region represents the transition from peat smouldering to char oxidation. During the period of peat smouldering, the yields of CO and CO_2 are on the order of 0.2 and 0.5 $kg \cdot kg^{-1}$ respectively. After the transition to the char oxidation regime, the yields increase to around 0.5 $kg \cdot kg^{-1}$ for CO and 2 $kg \cdot kg^{-1}$ for CO_2 – an increase of 2 and 4 times respectively. During the peat smouldering regime the peat is undergoing pyrolysis as well as oxidation. This results in a significant mass of carbon being lost as products of pyrolysis. After the transition, when the char cannot further pyrolyse, the mass loss is almost entirely a result of the reaction between char and oxygen to produce CO and CO_2, resulting in significantly higher yields. Yields during the initial 2 min and final 5 min of the experiments where the mass loss rates are low are not shown as the mass loss rate is too low.

The effect of heat flux on the average yield of CO and CO_2 during the peat smouldering and char oxidation regimes are shown in Fig. 6.8. During the peat smouldering regime, the yields of CO_2 increase from 0.25 to 0.6 $kg \cdot kg^{-1}$ over the heat flux range studied, while the CO yield remains relatively constant at around 0.18 $kg \cdot kg^{-1}$. The average yields during the char oxidation regime are approximately 0.4 and 2 $kg \cdot kg^{-1}$ for CO and CO_2 respectively and do not show significant dependence on the heat flux.

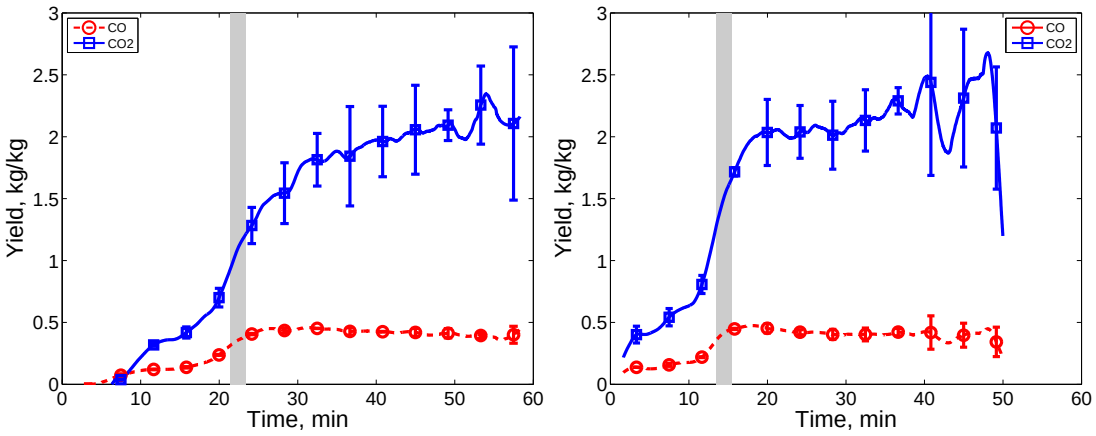

Figure 6.7. The yields of CO and CO_2 for experiments carried out at heat fluxes (a) 7.5 $kW \cdot m^{-2}$ and (b) 20 $kW \cdot m^{-2}$ with air flow of 70 $mm \cdot s^{-1}$. The shaded areas show the change from peat smouldering to char oxidation.

6.3.5 CO/CO_2 ratio

The CO/CO_2 ratio was found by dividing the mass flux of CO by that of CO_2. For heat fluxes 7.5 and 20 $kW \cdot m^{-2}$ this is plotted in Fig. 6.9. Relatively more CO is found to be produced per unit CO_2 during the peat smouldering than during the char oxidation regime. This is in agreement with the observation that during the peat smouldering regime relatively more pyrolysis reactions occur than during the char oxidation regime when the formation of CO_2 over CO is favoured. Fig. 6.10 shows that there is no significant effect of heat flux on the ratio during the peat smouldering and char oxidation regimes, as these are constant at 0.29 and 0.19 $kg \cdot kg^{-1}$ respectively. The ratios for the beginning and end of the experiments are not shown as the fluxes are low.

The ratio can also be expressed by plotting the average mass flux of CO against the average mass flux of CO_2 during an experiment, as seen in Fig. 6.11. This plot shows, the average flux for all combinations of heat flux and air flow. The gradient of the best-fit line is approximately 0.2. This shows that the ratio is relatively constant over a wide range of smouldering conditions.

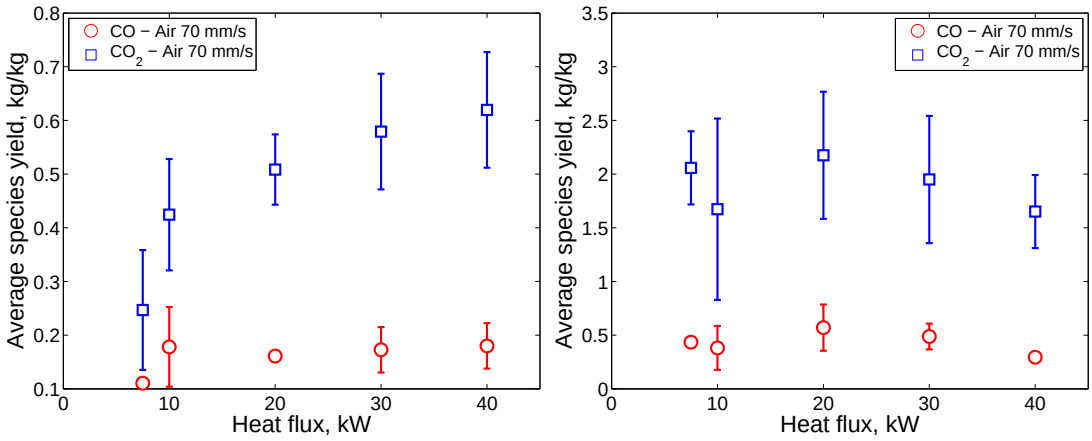

Figure 6.8. The yield of CO and CO_2 during (a) peat smouldering and (b) char oxidation.

Table 6.3. Summary of mass flux, yields and ratio reported in the literature and comparison to the peat smouldering and char oxidation observed in the present work. Average mass fluxes are presented in previous work and peak mass fluxes are reported in this study.

	Mass flux $g \cdot s^{-1} \cdot m^{-2}$		Yield $kg \cdot kg^{-1}$		CO/CO_2 ratio –
	CO	CO_2	CO	CO_2	
Rein et al. [16]	0.2–0.5	0.3–1.2	0.16–0.21	0.25–0.80	0.3–0.7
Christian et al. [14]	–	–	0.21	1.70	0.12
Yokelson et al. [25]	–	–	0.16	1.30	0.19
Yokelson et al. [25]	–	–	0.22	1.25	0.28
Akagi et al. [26]	–	–	0.18	1.56	0.12
Peat smouldering	0.8–1.3	2.5–3.6	0.12–0.18	0.25–0.6	0.3
Char oxidation	–	–	0.4	2	0.2

6.3.6 Comparison to literature

Results from the present study and those found in the literature are presented in Table 6.3 for comparison. Rein et al. [16] reported a series of small-scale calorimeter tests similar in set-up to this work using Scottish boreal peat under natural flow conditions in a non-porous sample holder. They investigated the effects of moisture content (from 80 to 600% in dry base) and heat flux (from 30 to 70 $kW \cdot m^{-2}$) on the emissions. These ranges are higher than the 0.6±0.3% moisture content and heat fluxes of 7.5–40 $kW \cdot m^{-2}$ studied here and the set-up does not allow for air flow through the sample. They report lower mass fluxes of CO and CO_2 than in this work, however these are given as an average during a period of 'steady-state' burning, not the peak as reported here. The

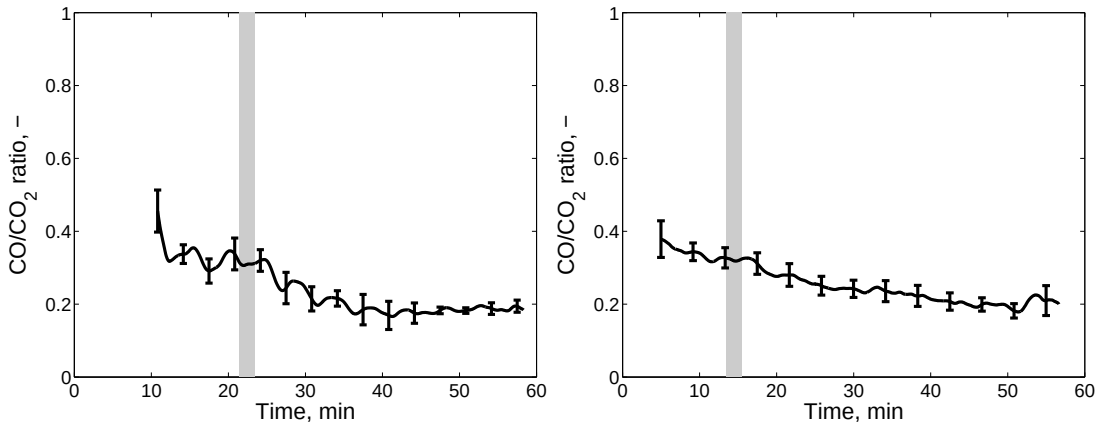

Figure 6.9. The ratio of CO and CO_2 for experiments carried out at heat fluxes (a) 7.5 $kW \cdot m^{-2}$ and (b) 20 $kW \cdot m^{-2}$ with air flow of 70 $mm \cdot s^{-1}$. The shaded areas show the change from peat smouldering to char oxidation.

range of yields reported are in agreement with this work, however the CO/CO_2 ratio is higher. This might be due to a limited oxygen flux to the smoulder front due to the closed sample holder, increased heat losses due to the moisture content and the high heat fluxes which favour the pyrolysis reaction and therefore the formation of CO over CO_2.

Christian [14], Yokelson [25] and Akagi [26] report emission factors in g of species emitted per kg of peat consumed for Indonesian [14] and North American peat [25, 26]. These are converted to yields for comparison. The values reported fall within the ranges given here, however as no details as to the smoulder environment are given, it is not possible to quantify the emissions as a function of the burning dynamics.

6.3.7 Effect of flow

The effect of the flow on the mass flux of CO and CO_2 is shown in Fig. 6.12. The effect is relatively small with the flux of CO_2 increasing from 1 to 1.4 $g \cdot s^{-1} \cdot m^{-2}$ as the flow is increased from no forced flow to 300 $mm \cdot s^{-1}$. At higher flow velocities, oxidation of the sample is more complete resulting in increased formation of CO_2. The mass flux of CO is relatively unchanged with flow, remaining at 0.3 $g \cdot s^{-1} \cdot m^{-2}$.

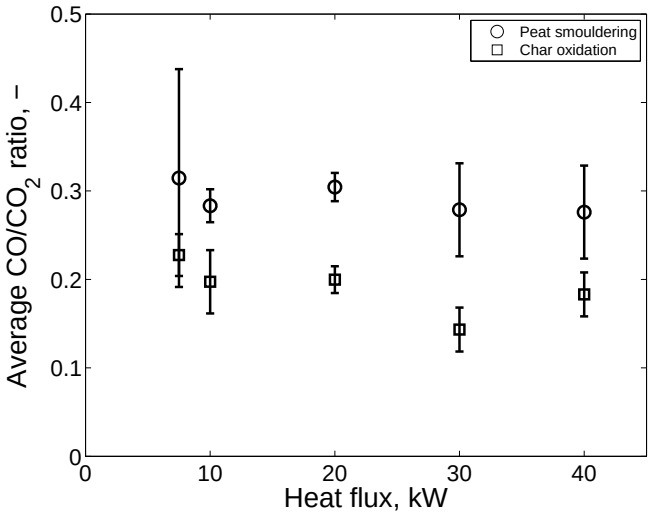

Figure 6.10. The yield of CO and CO_2 during peat smouldering (circles) and char oxidation (squares).

6.4 Comparison of emissions from flaming and smouldering peat

Using knowledge of the combustion dynamics, detailed measurements of the emissions as a function of the smouldering conditions have been made. This can be extended to determine the differences in CO and CO_2 emissions from smouldering and flaming combustion. As discussed previously, under the appropriate conditions it is possible for peat to undergo flaming combustion. This requires that the peat is heated such that the pyrolysate is emitted in sufficient quantity to allow a flammable pyrolysate/air mixture to be formed above the sample. If a pilot flame (or other ignition source) is present to ignite these vapours, flaming ignition can occur. In natural conditions, this would require that the peat is very dry and the smouldering is very intense. Flaming was observed at all the heat fluxes tested when a pilot flame was present and was found to occur during the first regime only. The duration of flaming was short ($<$10 min) and always followed by a period of in-depth smoulder.

The mass loss rate for experiments at 10 kW$\cdot$m^{-2} and 70 mm$\cdot$s^{-1} in which flaming was ignited by the pilot is shown in Fig. 6.13 and compared to an experiment under the same conditions but without the pilot. The period during which flaming was observed visually is indicated by the shaded region and detailed in the inset. It is seen that the mass loss behaviour is similar in both cases. There is an initial peak at around 6 g$\cdot$s$^{-1}\cdot$m^{-2} after 5 min. Fig. 6.14 shows that a slightly higher peak mass loss rate is

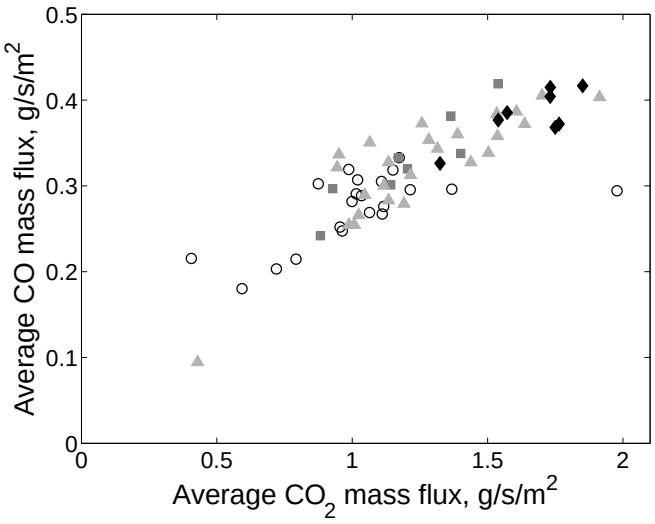

Figure 6.11. The mass flux of CO vs the mass flux of CO_2. There is a linear relationship between the production of CO for a value of CO_2. The circles represent natural flow, squares 40 mm·s^{-1}, triangles 70 mm·s^{-1} and diamonds 300 mm·s^{-1}.

consistently observed in the experiments which underwent flaming. The mass lost during flaming corresponds to 10–20% of the total mass.

The mass fluxes of CO and CO_2 for the experiment described above are shown in Fig. 6.15. During the time when flaming is observed (see inset), the mass flux of CO is less than 0.1 g·s^{-1}·m^{-2} and the peak mass flux of CO_2 is approximately 7.7 g·s^{-1}·m^{-2} (attained after 5 min) compared to 0.7 and 1.9 g·s^{-1}·m^{-2} during smouldering. This corresponds to an increase of more than 3.8 times for CO_2 and a CO flux 0.75 times lower than during smouldering. After flaming, the mass fluxes of CO and CO_2 for the piloted and non-piloted experiments is similar although there is a slight decrease in CO_2 flux immediately following flaming compared to experiments in which only smouldering was observed. This highlights the differences in chemical processes between the two modes of combustion and shows that flaming promotes the formation of CO_2 over CO.

Figure 6.16 shows a comparison of the mass fluxes of CO_2 (Fig. 6.16b) and CO (Fig. 6.16a) during flaming and smouldering as a function of the heat flux. It is seen that during flaming, the peak mass flux of CO_2 is significantly higher than the average mass flux during smouldering. At low heat fluxes, the increase is around 3 times but this increases at higher heat fluxes to 4 times the flux of smouldering. The mass flux of CO_2

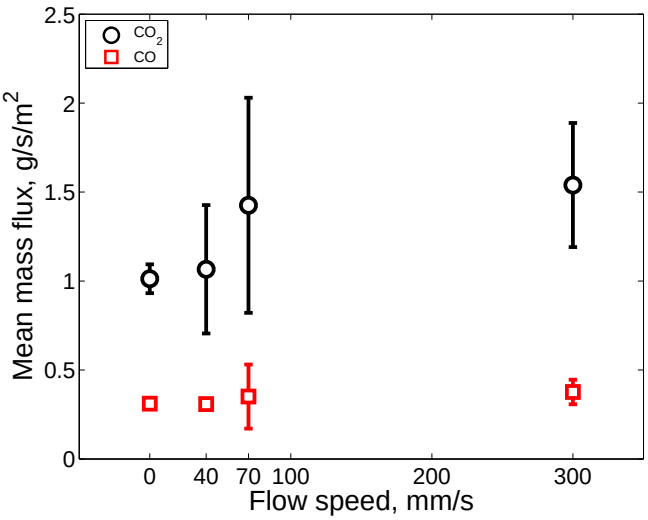

Figure 6.12. The mean mass flux of CO and CO_2 for experiments carried out 10 $kW \cdot m^{-2}$ and flow speeds of 0, 40, 70 and 300 $mm \cdot s^{-1}$.

is observed to depend more strongly on heat flux during flaming than smouldering. The opposite trend is observed in the CO emissions. During flaming, these remain relatively constant across the heat fluxes studied at around 0.25 $g \cdot s^{-1} \cdot m^{-2}$, but during smouldering this increases from 0.6–1.3 $g \cdot s^{-1} \cdot m^{-2}$ over the heat flux range studied.

The yields of CO and CO_2 are shown in Fig. 6.17a. During the period of flaming, there is a significantly higher yield of CO_2 (1.25 $kg \cdot kg^{-1}$) than at the corresponding time during smouldering (0.5 $kg \cdot kg^{-1}$). However, this yield is not as large as that observed during the char oxidation regime (i.e. at times greater than 20 min) which is around 2 $kg \cdot kg^{-1}$. During flaming, the yield of CO is very low (< 0.05 $kg \cdot kg^{-1}$).

The CO/CO_2 ratio is shown in Fig. 6.17b. The production of CO_2 is favoured during the flaming period with ratios close to zero compared to peak ratios of 0.45 at 5 min for smouldering peat. This again shows that there are different chemical processes occurring during flaming and smouldering combustion. After the period of flaming, the experiments show similar trends in both the yields and ratio.

The CO and CO_2 yields as a function of heat flux are shown in Figs 6.18b and 6.18a respectively. The yields of both species are relatively constant with heat flux for smouldering and flaming. The CO yield during flaming is below 0.05 $kg \cdot kg^{-1}$ compared to approximately 0.3 $kg \cdot kg^{-1}$ during smouldering. The CO_2 yield during flaming combustion is 0.75 $kg \cdot kg^{-1}$ compared to 1.25 $kg \cdot kg^{-1}$ during smouldering.

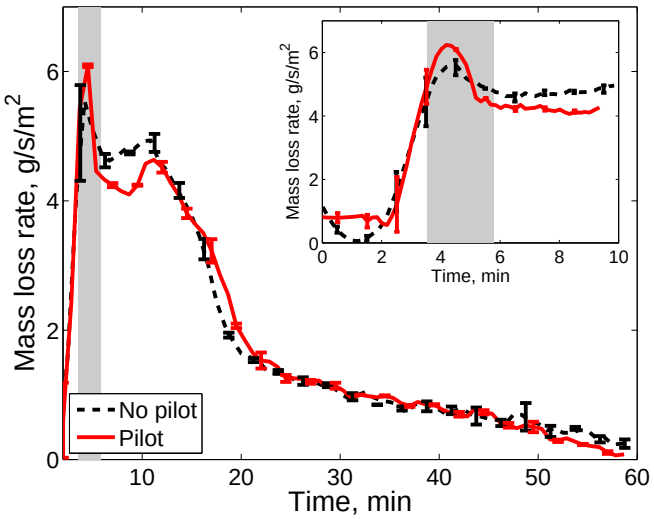

Figure 6.13. The mass loss rate for experiments in which flaming was ignited using a pilot flame (solid) and where only smoulder was observed (dashed). The shaded are represents the duration of the flaming. The inset details differences in mass loss rate during the period of flaming.

This highlights the differences in emissions from these combustion regimes.

A comparison of the CO/CO_2 ratio during flaming and smouldering combustion is given in Fig. 6.19. The ratio is seen to be consistently less than 0.1 for flaming compared to 0.2–0.3 during smouldering.

Figure 6.20 shows the percentage of the emissions from a sample during the period of flaming as a percentage of the total released during the burning process. It is observed that flaming contributes less than 15% of the CO_2 and 3% of the CO emissions across a wide range of experimental conditions. In a real peat fire, this fraction will depend on the depth of the peat layer. For thicker peat layers, the in-depth smoulder reaction will be sustained for longer, and release more CO and CO_2, while the duration of the surface flaming (a function of the surface area) will not change significantly.

6.4.1 Characteristics of flaming

Time to ignition and duration of flaming

The time to flaming ignition is defined as the time taken from exposure to the heat flux to the onset of piloted ignition. This is shown in Fig. 6.21a to decrease as the applied heat flux is increased. This is because at higher heat fluxes, flammable vapours are released from the peat in sufficient concentration earlier than at lower heat fluxes,

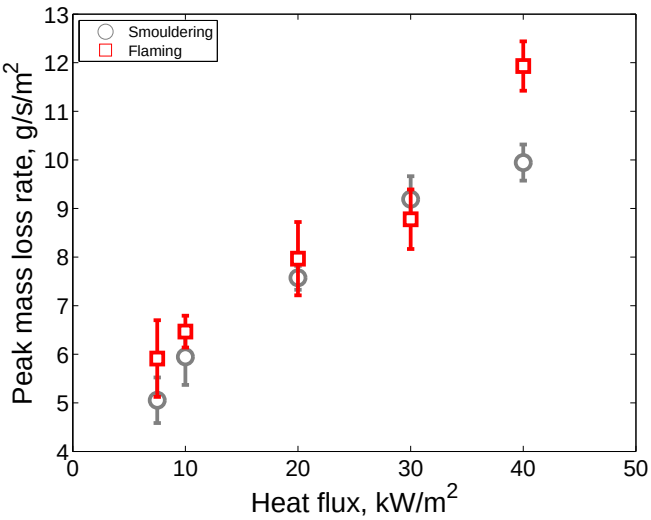

Figure 6.14. The peak mass loss rate for experiments in which flaming was ignited using a pilot flame and where only smoulder was observed. Flaming combustion is generally seen to result in slightly higher mass loss rate compared to smouldering.

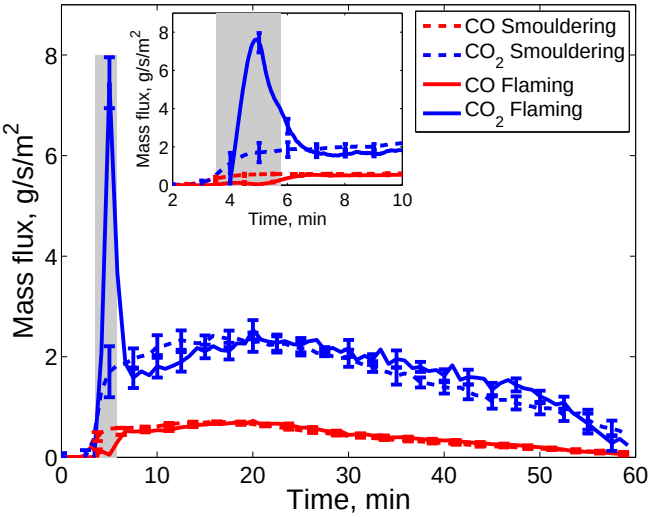

Figure 6.15. The mass flux of CO (red) and CO_2 (blue) for experiments in which flaming was ignited using a pilot flame (solid) and where only smoulder was observed (dashed). The shaded region represents the duration of the flaming. The inset details differences in emissions during the period of flaming.

thereby allowing flaming to be initiated sooner after exposure to the heat flux.

The duration of flaming was also found to be a function of applied heat flux (Fig. 6.21b). This was calculated by recording the time to ignition and the time of flame out (the time that the last flame is observed). As the heat flux is increased, the period during which flaming occurs increases from less than 2 min at 7.5 kW·m^{-2} to

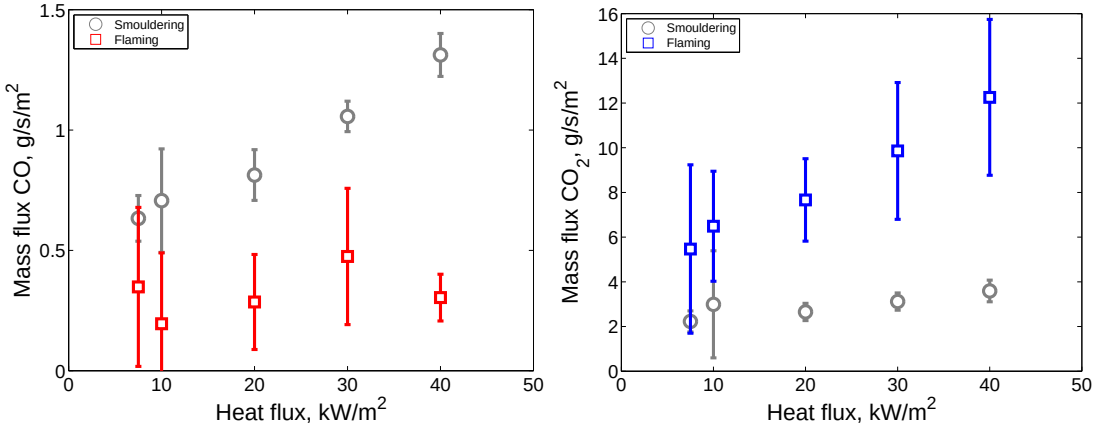

(a) (b)

Figure 6.16. Comparison of the the mass fluxes of (a) CO and (b) CO_2 during smouldering and flaming combustion.

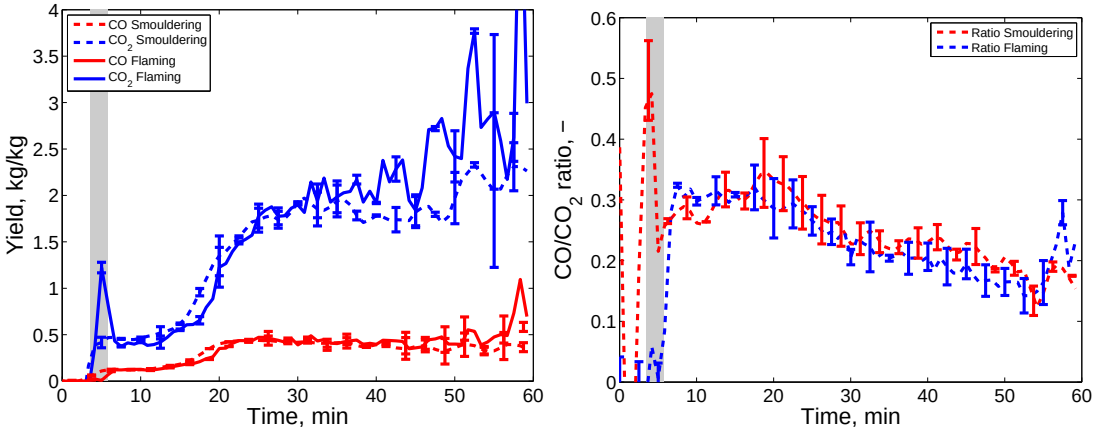

(a) (b)

Figure 6.17. (a) The yield of CO and CO_2 and (b) the CO/CO_2 ratio for experiments with piloted flaming ignition (solid) and smouldering ignition (dashed) with exposure to 10 kW·m^{-2} and flow of 70 mm·s^{-1}.

around 7 min at 40 kW·m^{-2}. This is because at high heat fluxes, volatiles are given off in sufficient concentration sooner than at low heat fluxes and because the heat is transferred further into the sample, which allows more vapours to be evolved at depth which sustain the flame for longer. The combination of these effects results in a longer period of flaming as the heat flux is increased.

Compared to the total duration of the experiment (>60 min), the flaming phase lasts only for a short period (typically <10% of the total time). For the majority of the time the peat is undergoing smouldering combustion. This highlights that smouldering is the dominant form of peat combustion.

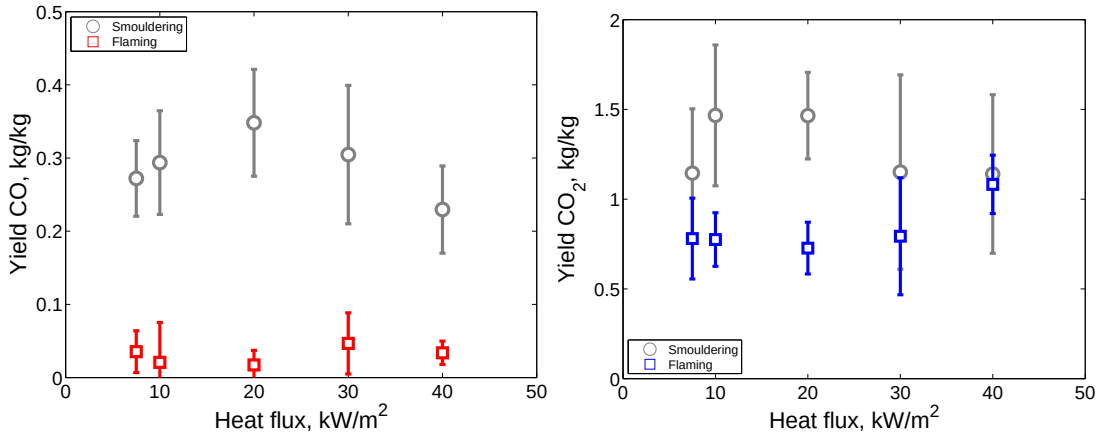

Figure 6.18. Comparison of the the yields of (a) CO and (b) CO_2 during smouldering and flaming combustion.

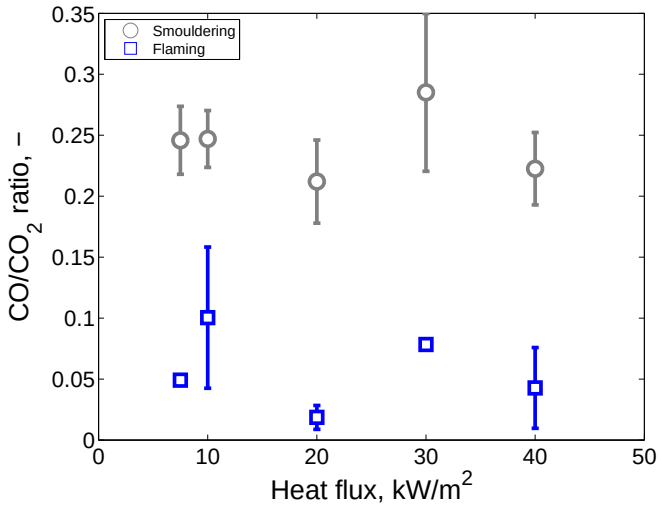

Figure 6.19. The CO/CO_2 ratio during smouldering and flaming combustion.

Effect of flow

The effect of flow on flaming peat at 10 $kW \cdot m^{-2}$ is observed in Fig. 6.22. As the flow is increased the mean mass flux of CO_2 increases from 1.1 $g \cdot s^{-1} \cdot m^{-2}$ under natural conditions to 2 $g \cdot s^{-1} \cdot m^{-2}$ at 300 $mm \cdot s^{-1}$ but, no significant effect can be seen on the CO production. The yield shows a similar trend, but the effect of forced flow is small and yield of CO_2 is around 0.8 $kg \cdot kg^{-1}$. There is a strong effect on the duration of flaming (Fig. 6.22c) increasing from 1 to 16 min as the flow speed is increased. This suggests that at high velocities, the increased flow through the peat permits transport of the pyrolysis vapours to the surface where they can undergo flaming combustion.

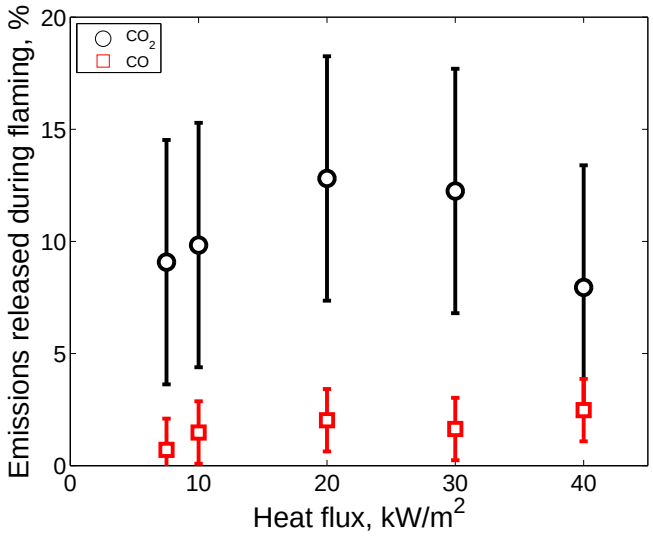

Figure 6.20. The percentage of total CO and CO_2 emissions from flaming combustion.

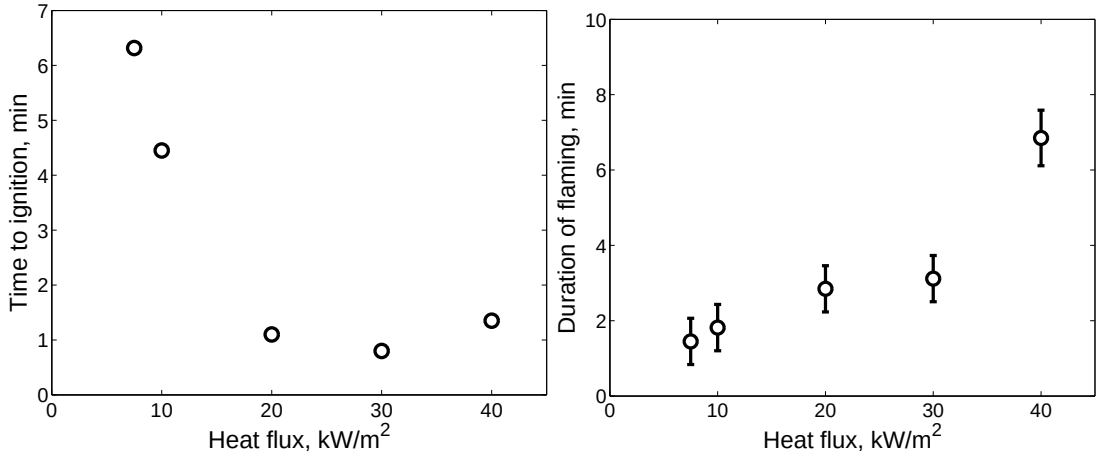

Figure 6.21. (a) The time to ignition as a function of applied heat flux and (b) the duration of the period of flaming combustion. The error in the time to ignition is included in the symbol size.

6.5 Conclusions

A detailed study of the carbon emissions from smouldering peat fires has been undertaken in controlled laboratory conditions. It has been shown that peat can undergo both flaming and smouldering combustion but that smouldering is the dominant mode of combustion. The smoulder process can be divided into an initial period of peat smouldering in which the fluxes and yields of CO and CO_2 are low and the CO/CO_2 ratio is around 0.3. After this period, there is a transition to a period of char oxidation.

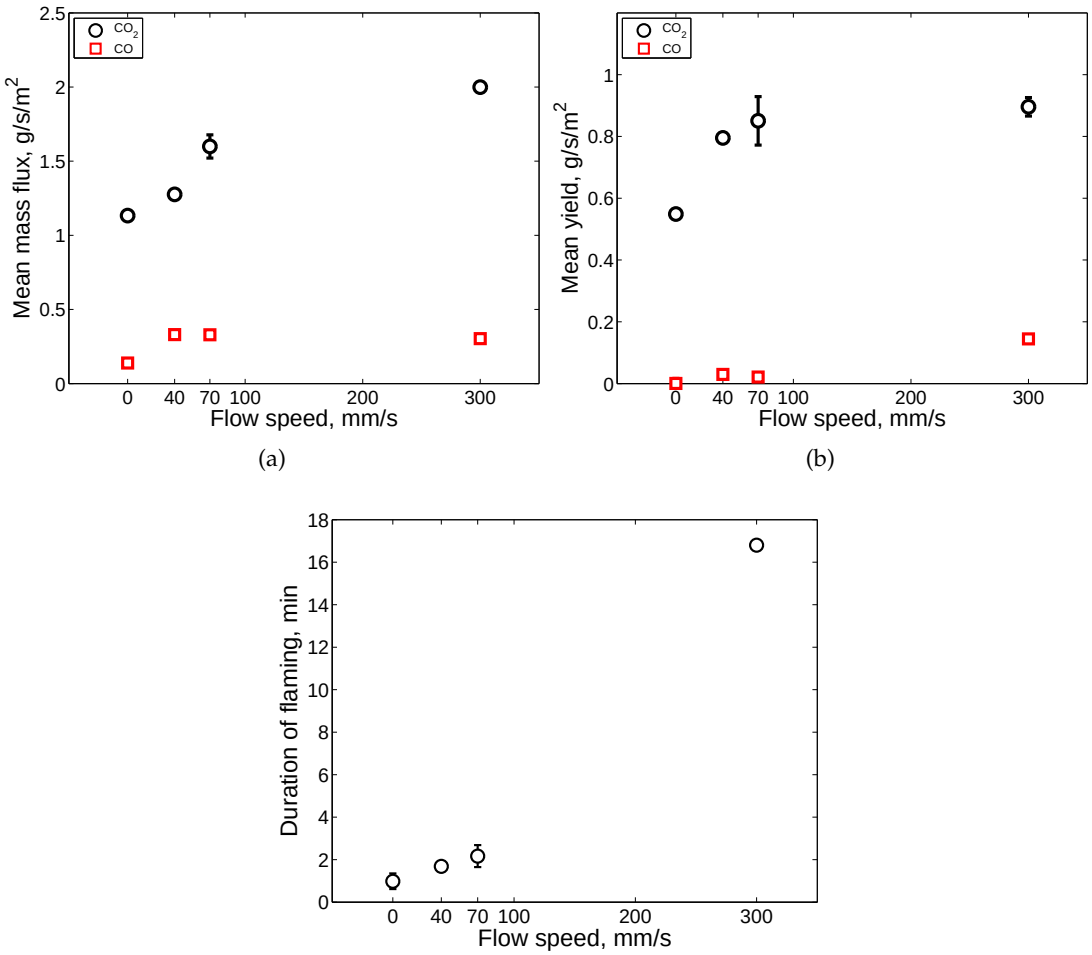

Figure 6.22. Effect of flow on (a) the mass flux and (b) the yield of CO and CO_2 and (c) the duration of flaming combustion.

This is characterized by high CO and CO_2 yields and a lower CO/CO_2 ratio. The emissions from flaming combustion differ significantly from smouldering emissions. Flaming was found to occur only during the regime of peat smouldering and in all cases lasted for less than 10 min.

The mass flux and yields of emissions are shown to be markedly different with typical CO and CO_2 fluxes of 0.5 and 2 $g{\cdot}s^{-1}{\cdot}m^{-2}$ for smouldering and 0.1 and 7 $g{\cdot}s^{-1}{\cdot}m^{-2}$ for flaming. This shows that these modes of combustion are controlled by different chemical processes. The yields of CO and CO_2 from smouldering are 0.4 and 2 $kg{\cdot}kg^{-1}$ and less than 0.1 and 1.25 $kg{\cdot}kg^{-1}$ respectively for flaming combustion. The CO/CO_2 ratio during smouldering is of the order 0.3–0.4, while for flaming this drops to below 0.1 as the production of CO is low.

Flaming is shown to account for less than 20% of the CO_2 and 5% of the CO emissions from these small-scale experiments on a mass basis. This fraction will decrease as the depth of the peat layer is increased and in-depth smoulder is enhanced.

Emissions from smouldering peat have been quantified under controlled laboratory conditions and shown to be significant compared to flaming fires. This work has provided a significant step forward in understanding emissions from smouldering peat fires as emissions have been quantified as a function of the combustion dynamics. The findings from this work can be applied to estimate CO and CO_2 from fires in shallow layers of peat. Behaviour under other conditions and configurations typical of smouldering (e.g. deep fronts, high moisture content) requires additional work, especially in cases where smouldering can propagate beneath the surface.

References

[1] G. Rein. Smouldering combustion phenomena in science and technology. *International Review of Chemical Engineering*, 1:3–18, 2009. URL hdl.handle.net/1842/2678.

[2] S. E. Page, F. Siegert, J. O. Rieley, H.-D. V. Boehm, A. Jaya, and S. Limin. The amount of carbon released from peat and forest fires in Indonesia during 1997. *Nature*, 420:61–65, 2002. doi: 10.1038/nature01131.

[3] B. Poulter, N. L. Christensen Jr, and P. N. Halpin. Carbon emissions from a temperate peat fire and its relevance to interannual variability of trace atmospheric greenhouse gases. *Journal of Geophysical Research*, 111:D06301, 2006. doi: 10.1029/2005JD006455.

[4] Evans Road Fire – Pocosin Lakes National Wildlife Refuge. Published Online, 2009. URL www.fws.gov/pocosinlakes/erf.html. Accessed September 2011.

[5] A. E. Kramer. Past errors to blame for Russias peat fires. Published Online, 2010. URL www.nytimes.com/2010/08/13/world/europe/13russia.html. Accessed September 2011.

[6] M. R. Turetsky, E. S. Kane, J. W. Harden, R. D. Ottmar, K. L. Manies, E. Hoy, and E. S. Kasischke. Recent acceleration of biomass burning and carbon losses in Alaskan forests and peatlands. *Nature Geoscience*, 4(1):27–31, 2011. doi: 10.1038/ngeo1027.

[7] M. C. Mack, M. S. Bret-Harte, T. N. Hollingsworth, R. R. Jandt, E. A. G. Schuur, G. R. Shaver, and D. L. Verbyla. Carbon loss from an unprecedented Arctic tundra wildfire. *Nature*, 475(7357):489–492, 2011. doi: 10.1038/nature10283.

[8] W. H. Frandsen. The influence of moisture and mineral soil on the combustion limits of smouldering forest duff. *Canadian Journal of Forest Research*, 17:1540–1544, 1987.

[9] W. H. Frandsen. Heat evolved from smoldering peat. *International Journal of Wildland Fire*, 1(3):197–204, 1991. doi: 10.1071/WF9910197.

[10] W. H. Frandsen. Ignition probability of organic soils. *Canadian Journal of Forest Research*, 27:1471–1477, 1997.

[11] M. Janssens. *SFPE Fire Protection Handbook*, chapter 3-2: Calorimetry, pages 3–60–3–89. National Fire Protection Association, Quincy, MA 02269, 3rd edition, 2008.

[12] G. Rein, N. Cleaver, C. Ashton, P. Pironi, and J. L. Torero. The severity of smouldering peat fires and damage to the forest soil. *Catena*, 74(3):304–309, 2008. doi: 10.1016/j.catena.2008.05.008.

[13] C. M. Belcher, J. M. Yearsley, R. M. Hadden, J. C. McElwain, and G. Rein. Baseline intrinsic flammability of Earth's ecosystems estimated from paleoatmospheric oxygen over the past 350 million years. *Proceedings of the National Academy of Sciences*, 107(52):22448–22453, 2010. doi: 10.1073/pnas.1011974107.

[14] T. J. Christian, B. Kleiss, R. J. Yokelson, R. Holzinger, P. J. Crutzen, W. M. Hao, B. H. Saharjo, and D. E. Ward. Comprehensive laboratory measurements of biomass-burning emissions: 1. emissions from Indonesian, African, and other

fuels. *Journal of Geophysical Research*, 108(D23):4719, 2003. doi: 10.1029/2003JD003704.

[15] T. R. Muraleedharan, M. Radojevic, A. Waugh, and A. Caruana. Emissions from the combustion of peat: an experimental study. *Atmospheric Environment*, 34(18): 3033–3035, 2000. doi: 10.1016/S1352-2310(99)00512-9.

[16] G. Rein, S. Cohen, and A. Simeoni. Carbon emissions from smouldering peat in shallow and strong fronts. *Proceedings of the Combustion Institute*, 32(2):2489–2496, 2009. doi: 10.1016/j.proci.2008.07.008.

[17] V. Babrauskas. *SFPE Fire Protection Handbook*, chapter 3-3 The Cone Calorimeter, pages 3–90–3–108. National Fire Protection Association, Quincy, MA 02269, 3rd edition, 2008.

[18] ASTM International. ASTM E2058 -09, Standard test methods for measurement of synthetic polymer material flammability using a Fire Propagation Apparatus (FPA), 2009.

[19] D. Drysdale. *An Introduction to Fire Dynamics*. John Wiley and Sons Ltd, Chichester, UK, 2nd edition, 1998.

[20] K. N. Palmer. Smouldering combustion in dusts and firbous materials. *Combustion and Flame*, 1:129–154, 1957.

[21] T. J. Ohlemiller. *SFPE Fire Protection Handbook*, chapter 2-10: Smouldering Combustion, pages 2–201–2–210. National Fire Protection Association, Quincy, MA 02269, 3rd edition, 2002.

[22] G. B. Stracher and T. P. Taylor. Coal fires burning out of control around the world: thermodynamic recipe for environmental catastrophe. *International Journal of Coal Geology*, 59(1-2):7–17, 2004. doi: 10.1016/j.coal.2003.03.002.

[23] C. F. Schemel, A. Simeoni, H. Biteau, J. D. Rivera, and J. L. Torero. A calorimetric study of wildland fuels. *Experimental Thermal and Fluid Science*, 32(7):1381–1389, 2008. doi: 10.1016/j.expthermflusci.2007.11.011.

[24] J. L. Torero. *Buoyancy Effects on Smoldering of Polyurethane Foam*. PhD thesis, University of California, Berkeley, 1992. URL www.era.lib.ed.ac.uk/handle/1842/2134.

[25] R. J. Yokelson, R. Susott, D. E. Ward, J. Reardon, and D. W. T. Griffith. Emissions from smoldering combustion of biomass measured by open-path Fourier transform infrared spectroscopy. *Journal of Geophysical Research*, 102(D15): 18865–18877, 1997. doi: 10.1029/97JD00852.

[26] S. K. Akagi, R. J. Yokelson, C. Wiedinmyer, M. J. Alvarado, J. S. Reid, T. Karl, J. D. Crounse, and P. O. Wennberg. Emission factors for open and domestic biomass burning for use in atmospheric models. *Atmospheric Chemistry and Physics*, 11: 4039–4072, 2011. doi: 10.5194/acp-11-4039-2011.

7

Conclusions

In this thesis, smouldering combustion and self-sustaining reactions in solids have been studied in small-scale laboratory experiments. Smouldering is a significant threat to the natural and man-made environments and this work has sought to understand the processes involved and to assess this hazard. The ignition, propagation, suppression and emissions from smouldering fires in fuels common in the built and natural environments have been investigated.

The ignition of smouldering has been studied in Chapters 1, 2, 3, 4 and 5. Understanding the factors which can lead to ignition is essential in order to reduce risk due to smouldering fires. Ignition has been studied using radiant heat (Chapters 2 and 5) and conductive heat sources (Chapters 3 and 4). The latter can be divided further into constant energy (Chapter 4) and varying energy sources (Chapter 3). Ignition of smouldering fires due to radiative heating is rare outside the laboratory. However, this kind of heating is useful in the laboratory as the energy absorbed by the solid can be easily quantified with little dependence on the properties of the solid. Conductive heating is more realistic; it simulates ignition by hot surfaces or parts (commonly found in process plants) as well as providing a good analogy for ignition by another smouldering source, e.g. ignition of material by a cigarette.

The study of ignition by these means has shown it to be a complex phenomenon dependent on the heat source and the properties of the fuel. The mode of heat transfer to the solid and the rate at which the heat is transferred (Chapter 1) is important, as well as the chemical and physical properties of the fuel. For example, results from Chapter 4

show that there was an optimum particle size for ignition, comparing the ignition of similar fuels with different densities (cf. Chapters 4 and 5) indicated that fuels with lower density are easier to ignite and in Chapter 2 it was shown that larger samples can be ignited at lower heat fluxes than smaller samples. In general, the properties which effect ignition are those which govern the heating of the solid fuel.

Convective heating of the solid has not been studied. This mode of ignition involves heating the air stream coming in contact with the solid fuel. As this has not previously been studied, it offers scope for novel contributions. This method may allow simplified study of the ignition processes by eliminating uncertainties introduced by the external heaters traditionally used. An experiment like this would be similar to traditional self-heating experiments. These involve the heating of a material in a hot oven for extended periods of time. Smouldering ignition can, and should, be studied alongside this phenomenon.

Once ignited, smouldering will propagate through the mass of a fuel. By adjusting key variables such as applied heat flux and the atmosphere in which the smoulder takes place, simplified reaction frameworks can be developed, as in Chapters 1 and 5 for reactions involving oxygen and non-oxygen-based chemistry. These are useful to assess the rate at which the smoulder reaction will propagate and to understand controlling mechanisms such as sample size (Chapter 2), heat losses from the smouldering front and the effects of oxidizer flow (Chapter 5). Understanding the dynamics relating to the spread of smouldering is essential to understand real smouldering events. In order to do this effectively, more detailed further work should focus on the scale-up of laboratory tests which are undertaken at the centimetre scale to real-scale scenarios, which can be on the order of tens of metres. This will allow results obtained in the laboratory to be applied with greater confidence to real smouldering fires.

The emissions from peat fires were studied in Chapter 6. This is an important aspect when assessing the impact smouldering has on the environment. This is the first time that the emissions have been studied as a function of the smouldering dynamics. The differences in the chemical processes involved in flaming and smouldering combustion were emphasized by the differences in CO and CO_2 production; CO/CO_2 ratios for smouldering were much higher compared to flaming combustion. It was also shown

that compared to flaming, smouldering releases significantly more CO_2 during the burning of a sample as it propagates in depth and consumes more material, while flaming is a surface phenomenon. Other emissions were not studied in this work and would provide significant contributions to further the understanding of the effect of large-scale smouldering fires on the environment.

The suppression of smouldering fires has been studied for the first time in this thesis (Chapter 4). This is a significant contribution to the state-of-the-art of smouldering combustion. Though it is a much less energetic mode of combustion than flaming, smouldering has been shown to be extremely difficult to extinguish. This difficulty arises from effectively delivering the extinguishing agent through a porous medium to the hot smouldering front. Using small-scale experiments with a much simpler configuration to real smouldering fires, this was shown to require large volumes of water thereby making it costly and inefficient. Other methods of extinguishing, such as preventing oxygen ingress to the reaction zone, are shown to be less effective due to the time frames involved and the detailed knowledge of the subsurface required.

Smouldering fires can lead to the ignition of large, flaming fires through the mechanism of transition to flaming. This was observed in Chapter 2, however a definitive conclusion as to the mechanism could not be drawn. Better understanding of this phenomenon could be gained by further detailed experimental study of the reaction dynamics, temperatures and gas-phase reaction products. This would allow the key mechanisms resulting in the transition to be identified.

7.1 Future work

Research on smouldering still represents a small fraction of all the work done in the field of Fire Science. Compared to flaming combustion, there are significantly fewer studies and the available data are relatively sparse. There are few (if any) standard test methodologies to reliably determine the smouldering behaviour of materials which leads to difficulty in applying results generally. Most of the work to date has been undertaken using polyurethane foams, however these are not representative of many fuels which smoulder, e.g. they do not contain moisture like natural fuels and they

have a very homogeneous structure. This makes them ideal for laboratory study but not necessarily representative of smoulder in the wider world. This lack of knowledge means that smouldering remains an interesting area in which to work with much still to be learned, most excitingly the potential beneficial applications of smouldering such as remediation of contaminated soil and biochar production.

In the built environment, the most important topic in smouldering combustion is understanding the transition from smouldering to flaming. Many fires begin as smouldering fires and it is when these transition to flaming that they become a significant threat to the structure of a building and human life. The current literature does not allow a definitive conclusion to be drawn regarding the mechanisms which control this phenomenon and more research is necessary. Future work studying the emissions from the smoulder reaction may prove useful in elucidating the controlling mechanisms. Understanding these mechanisms would allow the development of materials to eliminate this behaviour.

Work on the detection and suppression of smouldering fires would have relevance in industries which deal with reactive bulk solids where fires are most likely and costly. The difficulty with detecting smouldering fires arises due to the cool smoke which is typically produced. This means that smoke is not carried to high levels where detection equipment is located. Further work to establish a smouldering signature based on the emissions could be developed and implemented. This would allow detection to be undertaken in high-risk areas using gas analysis techniques. Once a smouldering fire has been detected, extinguishing the fire becomes the next difficulty. In reality, this is achieved either through flooding of the affected area or excavation of the fuel, which are not practicable in many situations. Further investigation into the suppression of these fires requires working across disciplines to fully understand the challenges involved in extinguishing and monitoring large-scale smouldering fires.

There are many methods to ignite smouldering (e.g. radiant heat, contact ignition and self-heating) with no 'standard' method yet adopted. These methods cannot be easily related, partly due to the mathematics and partly due to the lack of data using similar materials and conditions. Such studies could allow the ignition to be quantified so that the behaviour of materials could be more accurately assessed under a range of

conditions.

The emissions from smouldering are also important in terms of life safety. The problem is two-fold: the low temperatures of smouldering result in a less buoyant smoke than flaming and the composition is unknown. The major hazard arises due to the toxicity associated with the chemical species produced by the incomplete smoulder reaction, which results in the production of large quantities of aerosol which are responsible for the smog produced from smouldering wildfires. This haze was evident in the 1997 fires in Borneo and the 2010 fires around Moscow. Further study of the products of smouldering combustion (e.g. using FTIR or GC-MS) would allow the potential impacts of the emissions to be quantified and better assessment of the toxicity to be undertaken.

Almost all experimental studies of smouldering are undertaken in small-scale laboratory experiments. However, in the natural environment, smouldering usually occurs on a much larger scale. The effect this will have on the smouldering dynamics could be estimated by an understanding of the controlling mechanisms of smouldering combustion and how these change across different scales, but this has not been studied experimentally. Further study of the scale effects is key if laboratory results are to be applied with confidence to real-scale scenarios.

Understanding of the many mechanisms involved in smouldering could be furthered through the development and application of appropriate computer models. Using these in conjunction with thorough experimental studies can allow rapid progression in the understanding of governing mechanisms of smouldering.

There is much still to do in the field of smouldering which will have impact and application across a broad range of disciplines in the built and natural environments. It is this breadth of application that continues to make smouldering an important and fascinating area of research.